In Between Matters
Interfaces in Complex Oxides

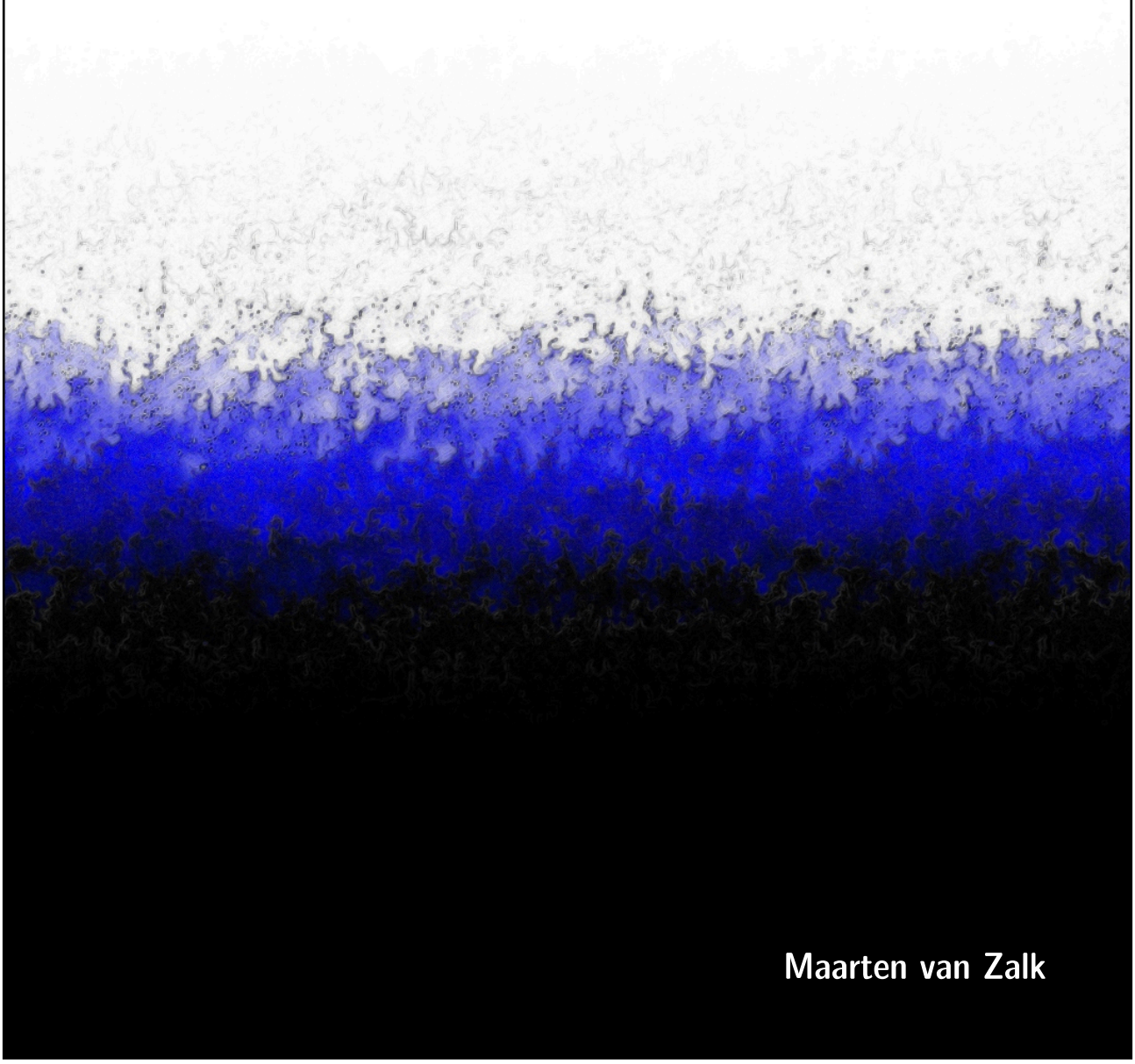

Maarten van Zalk

In Between Matters

Interfaces in Complex Oxides

Maarten van Zalk

Ph.D. committee

Chairman	
prof. dr. G. van der Steenhoven	University of Twente
Secretary	
prof. dr. G. van der Steenhoven	University of Twente
Supervisor	
prof. dr. ir. H. Hilgenkamp	University of Twente
Assistant-supervisor	
dr. ir. A. Brinkman	University of Twente
Members	
prof. dr. ir. B. Poelsema	University of Twente
prof. dr. P.J. Kelly	University of Twente
prof. dr. M.G. Blamire	University of Cambridge
prof. dr. J. Aarts	Leiden University
dr. ing. A.J.H.M. Rijnders	University of Twente

Cover

Atomic force microscopy image (digitally manipulated) of the surface of a 50 nm $La_{2-x}Sr_xCuO_4$ ($x = 0.125$) film, showing a meandering terrace-like structure. The field of view is approximately 10 μm, and the color scale (black to white) corresponds to about 6 nm.

The research described in this thesis was performed in the Faculty of Science and Technology and the MESA$^+$ Institute for Nanotechnology at the University of Twente, in collaboration with the High Field Magnet Laboratory in Nijmegen and Leiden University. The work was financially supported by the Netherlands Organization for Scientific Research (NWO) and the Dutch Foundation for Fundamental Research on Matter (FOM).

In Between Matters, Interfaces in Complex Oxides
Ph.D. Thesis, University of Twente
Printed by Gildeprint Drukkerijen
ISBN 978-90-365-2910-5

IN BETWEEN MATTERS, INTERFACES IN COMPLEX OXIDES

PROEFSCHRIFT

ter verkrijging van
de graad van doctor aan de Universiteit Twente,
op gezag van de rector magnificus,
prof. dr. H. Brinksma
volgens besluit van het College voor Promoties
in het openbaar te verdedigen
op vrijdag 13 november 2009 om 13:15 uur

door

Maarten van Zalk

geboren op 31 december 1980
te Harderwijk

Dit proefschrift is goedgekeurd door de promotor:

prof. dr. ir. H. Hilgenkamp

en de assistent-promotor:

dr. ir. A. Brinkman

Contents

Chapter 1 In between matters

Abstract

In this introductory chapter the research described in this thesis is motivated and a bird's-eye view over the work is given. The concepts of complex oxides and strongly correlated electron systems are introduced. Furthermore thin-film growth and sample fabrication are briefly discussed.

1.1 Materials and interfaces

Useful properties of materials have always been exploited. Stone was already used 2.5 million years ago for the creation of tools, such as hammers and axes, because of its hardness and density.[1] When copper (4000 BC), bronze (3000 BC), and iron (1500 BC) were discovered, it was realized that these metals and metal alloys not only provide such properties as well, but also large flexibility in the fabrication process.

Many centuries later, metals turned out to have another useful property: electrical conductivity. It was Henry Cavendish (1731–1810), who first classified materials according to their ability to conduct electricity.[2] It is worth mentioning his research method. In his laboratory in London, Cavendish created an electrical circuit, in which he included the material of interest, as well as himself. He then compared the intensity of the electric shock he received upon discharging a *Leyden jar* through the circuit, which gave him a measure for the conductivity of the material under test.

Leyden jars were the batteries of those times, although they were rather capacitors. The Leyden jar had been invented in Leiden, by the Dutch physicist Pieter van Musschenbroek (1692–1761) in 1746.[3] Cavendish used an improved version of Musschenbroek's design, consisting of a glass tube coated on the inside and outside with metal foil. By varying the radius of the glass tube, Cavendish not only proved that the force between electric charges varies inversely as the square of the distance between the charges (a result he never published and is therefore known as Coulomb's law, who established it in 1785 in a direct manner[4]), but also discovered that the glass was acting as if it were eight times thinner than it actually was.[2] Cavendish explained this result by supposing that the glass contained infinitesimal thin layers of alternately conducting and non-conducting material. By

experimenting with different kinds of glass and other non-conducting substances, Cavendish discovered a material property nowadays known as the dielectric constant.

Two centuries after the invention of the Leyden jar, Leiden was the place where yet another property of materials was discovered. Heike Kamerlingh Onnes[5] (1853–1926) had built there a state-of-the-art cooling machine and in 1908, he was the first who liquefied helium and reached temperatures as low as 1.5 K. When the electrical resistivity of solid mercury was measured in Onnes's machine, a sudden transition to a state of zero resistance was observed at 4.2 K: *superconductivity*. After 1911, various other metallic substances were found to be superconductors at low temperatures. Over the years, the highest transition temperature (also called critical temperature, from now on referred to as T_c) steadily grew up to 23 K reported for Nb_3Ge in 1974.[6] In 1986, J. Georg Bednorz and K. Alex Müller unexpectedly found superconductivity in the copper-oxide (or cuprate) $La_{2-x}Ba_xCuO_4$ at 35 K (Ref. 7) and initiated a sequence of discoveries of superconducting cuprate compounds with rapidly increasing T_c's, culminating in 1994 at 164 K for $HgBa_2Ca_2Cu_3O_{8+\delta}$ (under pressure).[8]

To use all the material properties mentioned above in a functional way, one often has to make combinations of different materials. The Leyden jar is a good example, as it is based on the separation of metal conductors by glass insulators. Combining materials inherently creates interfaces. In many cases, the functionality of the device as a whole is influenced by what happens at the interfaces. For the Leyden jar, the accumulation of charge at the metal/glass interface, greatly enhances its charge storage capacity.

Electronic components in particular, often depend crucially on interfaces. An example is the transistor, invented in 1947 by John Bardeen, Walter H. Brattain and William B. Shockley.[9,10] The transistor forms the basis for virtually all present electronic devices. The active part of the transistor is a boundary layer between two materials, which is normally depleted of charge carriers. By introducing charge carriers in the depletion region, the current through the transistor can be regulated.

Another example is the so-called giant-magnetoresistance (GMR) sensor, developed by Peter Grünberg, Albert Fert and coworkers,[11–13] which is a sensitive magnetic field sensor. Such sensors are used in computer harddisks to read the bits that are magnetically stored on the disk. The GMR sensor consists of a stacking of thin magnetic and non-magnetic metals. The stacking is composed in such a way that the resistance of the total device sensitively responds to magnetic field.

The examples above illustrate the significance of the understanding of interfaces for the functionalization of materials. With the field of complex oxides rapidly developing, it is important to study the interface behavior of these fascinating materials.

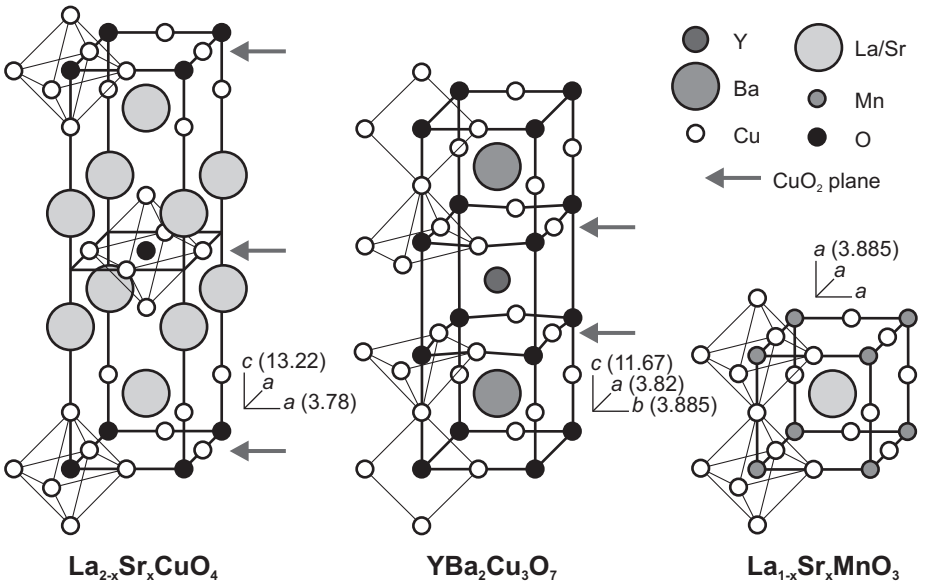

Figure 1.1: Crystal structure of three different complex oxides. Lattice parameters are indicated in Å.

1.2 Complex oxides

The discovery of high-T_c superconductivity in $La_{2-x}Ba_xCuO_4$ has generated a general interest in complex oxide materials over the past two decades. But what exactly is a complex oxide? The term itself is not an entry in the main encyclopedias. It is however commonly used to denote oxides with considerable complexity. In the Encyclopædia Britannica the term is used as a synonym for a multiple oxide, which together with the simple oxides form the group of oxide materials.[14] Whereas simple oxides consist by definition of a combination of one metal and oxygen, multiple oxides contain at least two metal ions (or two ions of the same metal with different oxidation states) and oxygen.

Fig. 1.1 shows the crystal structures of three different complex oxides, namely $La_{2-x}Sr_xCuO_4$ (from now on, abbreviated by LSCO), $YBa_2Cu_3O_7$ (YBCO) and $La_{1-x}Sr_xMnO_3$ (LSMO). The x appearing in the structure of LSCO and LSMO indicates that the material is obtained by replacing x La atoms by Sr atoms in La_2CuO_4 and $LaMnO_3$, respectively. The structure of $La_{2-x}Ba_xCuO_4$, the compound in which high-T_c superconductivity was discovered, is similar to that of LSCO, but with Ba substituted for La, instead of Sr. In the crystal structures in Fig. 1.1, we have indicated the geometrical shapes formed by oxygen atoms surrounding the smaller (Cu or Mn) elements. In LSCO and LSMO the oxygen atoms are arranged in octahedra. The crystal structures of these complex oxides

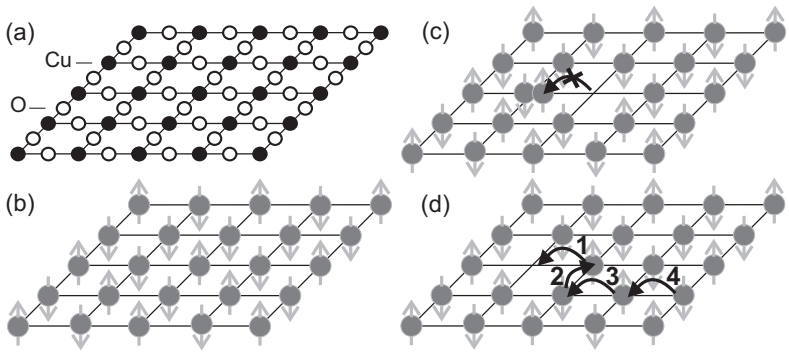

Figure 1.2: (a) Schematic representation of the CuO_2 plane characteristic for high-T_c superconductors. (b) In La_2CuO_4, the undoped parent compound of $La_{2-x}Sr_xCuO_4$, all Cu sites are occupied by one electron. (c) Hopping of electrons to neighboring sites is prevented by strong on-site Coulomb repulsion. (d) By Sr substitution for La, holes are introduced on the CuO_2 planes. These holes can freely move across the plane.

can be seen as a periodic arrangement of octahedra, intercalated by the larger elements (La/Sr). Characteristic for the high-T_c superconductors is the presence of CuO_2 planes, as indicated in the figure.

Although not by definition, the complex oxides often show also electronically rich and complicated behavior. This is the result of electron-electron *correlations*. Compounds in which these play an important role are therefore referred to as strongly correlated electron systems. We can illustrate the notion of electron correlations with the help of the CuO_2 planes mentioned in the previous paragraph. Many physicists believe that the essential physics of the high-T_c compounds is captured by what happens on these CuO_2 planes.[15,16] In Fig. 1.2(a,b) we have sketched the electronic arrangement for La_2CuO_4, the insulating parent compound of LSCO. At all copper sites resides one electron. According to electronic band theory, the CuO_2 plane should be conducting, but as we just mentioned, it is insulating. How can this be understood? In Fig. 1.2(c) we have sketched the possibility that an electron moves to a neighboring site, which then becomes doubly occupied. It turns out that strong on-site Coulomb repulsion prevents such a hopping process. The arising insulating phase is called a Mott insulator.[17] As a result of a second kind of interaction between neighboring electrons (virtual hopping[16]), their spins order in an antiferromagnetic lattice.

When Sr is substituted for La, electron holes are introduced on the CuO_2 plane, as indicated in Fig. 1.2(d). Electrons can hop to this hole without the Coulomb energy cost, and the hole is free to move across the plane. As a result, insulating behavior is rapidly destroyed for small doping $x \approx 0.03$–0.05. It is in the arising conducting state that high-T_c superconductivity appears for $x \approx 0.05$–0.25.

In Fig. 1.3(a) we have shown the schematic phase diagram for LSCO. Apart from the antiferromagnetic and superconducting regions just discussed, there is

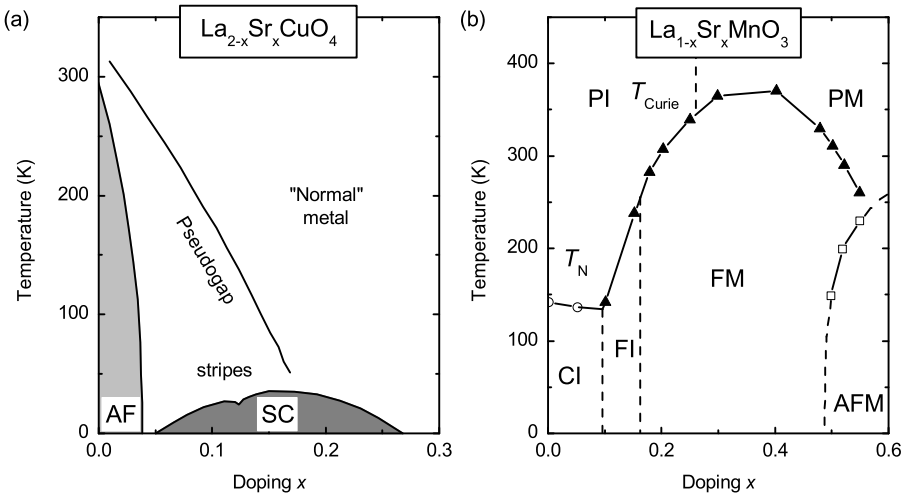

Figure 1.3: (a) Schematic phase diagram for the high-T_c superconductor $La_{2-x}Sr_xCuO_4$. AF and SC denote the antiferromagnetic and the superconducting state, respectively. The figure is reproduced in a modified form from Ref. 18. We have added the slight suppression of T_c reported around $x = 0.125$ (Ref. 19) and the fluctuating stripe phase around this doping.[20] (b) Phase diagram for $La_{1-x}Sr_xMnO_3$. PI denotes paramagnetic insulator, FI ferromagnetic insulator, FM ferromagnetic metal, PM paramagnetic metal, AFM antiferromagnetic metal, and CI spin-canted insulator state. (Figure reproduced from Ref. 21.)

also a so-called pseudogap phase.[22] The origin of this phase is unclear. There are two major schools of thought. The pseudogap might either be a precursor of the superconducting state, or it might reflect some kind of electronic ordering, perhaps remanent antiferromagnetic fluctuations of the nearby antiferromagnetic order for doping $x < 0.05$. A small dip[19] in the superconducting "dome" near $x = 0.125$ is associated with the presence of fluctuating stripes.[20,23–26] These self-assembling extended patterns of spins and charges are an exotic example of electron correlation effects. For large enough x, LSCO is metallic, but in many aspects, such as for instance transport, the metallic state deviates from that in ordinary metals.[27]

For LSMO the phase diagram is depicted in Fig. 1.3(b). The doping level x here determines the ratio Mn^{4+}/Mn^{3+} of valence states of the Mn ions.[21] Without going into all the details of the phase diagram, we note that electronic correlations (in this case double exchange) between electrons on neighboring Mn sites induce a ferromagnetic metallic state for $x \approx 0.16$–0.48, with a Curie temperature T_{Curie} above room temperature for a large part of this doping region. The ferromagnetic state is of particular interest because the electrons taking part in charge transport were reported to be 100 % spin polarized for $x = 0.3$.[28] This not only is interesting for device applications, such as magnetic field sensors,[29,30] but also creates opportunities for instance when combined with YBCO for fundamental studies on the interplay between spin-polarized ferromagnetism in the LSMO and

superconductivity and a tendency for antiferromagnetism in the YBCO.

The unprecedented richness of the phase diagrams in Fig. 1.3 indicate the versatility of complex oxides and correlated electron systems. Understanding their interfaces will certainly contribute to further development and applicability of these materials.

1.3 Outlook

The interface behavior of complex oxides will be studied in this thesis in a variety of cases. One of the main themes is the interplay between different properties of materials on both sides of the interface. Another important question is whether properties of the materials under study vary near interfaces to other materials. In the next section of this chapter, film growth and sample fabrication techniques relevant to all subsequent chapters will be introduced.

Chapter 2. In this chapter we describe how the mere presence of a STO substrate influences the electronic phase of a thin film of the high-T_c superconductor LSCO. As was described in Sec. 1.2, electrons self-organize in this material into striped patterns of charges and spins near doping $x = 0.125$. These stripes, or "rivers of charge", are expected to exist in LSCO in a fluctuating form.[20,23–26] This means the "rivers" meander in all directions and rapidly change position over time. A phase transition in the STO imposes a minute change in the crystal structure of the LSCO thin film, through the epitaxial connection between substrate and film. When this happens, the fluctuation stripes seem to come to a standstill and a static stripe phase appears, or, in simple words, the rivers turn into straight "canals", oriented along certain crystallographic orientations; a situation that for LSCO has never been observed before.

Chapter 3. Chapter 3 describes a tunnel study performed on LSCO. Tunneling is a suitable technique to examine the properties of a superconductor. Electrons tunnel from a metal electrode through an insulating barrier material into the LSCO, which is supposed to be superconducting. In Chapter 3, we find that the superconducting properties of the high-T_c superconductor are influenced by the presence of the STO barrier. The tunnel experiments indicate suppressed superconductivity near the LSCO/STO interface which can be understood from a local suppression of the charge carrier density and the LSCO locally being in the pseudogap (see Fig. 1.3) state.

Chapter 4. In Chapter 4, we further explore this phenomenon, but in a system consisting of YBCO and the half-metallic ferromagnet LSMO. Although there is no purposely fabricated tunnel barrier between the YBCO and the LSMO, we find that when a current is passed through the YBCO/LSMO contact, the resistance is large *as if* a tunnel barrier is present. We argue that such a tunnel barrier likely arises from the transfer of charge across the interface, which reduces the charge carrier density in the YBCO locally. This not only induces a high interface resistance, but also enhances antiferromagnetism in the YBCO near the interface,

since the doping level x at this position is decreased (see Fig. 1.3). The interplay with the spin polarization in the LSMO then gives rise to a strong dependence of the interfacial resistance on an externally applied magnetic field.
Chapter 5. Carrying on with YBCO/LSMO heterostructures, in Chapter 5 we consider the possibility that the sandwiching of the superconductor between spin-polarized ferromagnets enables switching of superconductivity through the reversal of the magnetization direction in one of the two ferromagnets.[31–33] The structure is reminiscent of the GMR-sensor described in Sec. 1.1. In this chapter we find clear evidence that in these oxide superconductor/ferromagnet hybrids resistance switching effects near T_c of the superconductor are dominated by effects of magnetic stray fields, stemming from the ferromagnetic layers. The structural properties of the interface (roughness) play an important role, because roughness enhances the stray fields through the superconductor.
Chapter 6. In Chapter 6, we switch to a system of stacked insulators, namely $SrTiO_3$ and $LaAlO_3$. Recently, the interface between these two insulators was found to be conducting.[34] We will investigate the properties of the conducting interface at low temperatures and in high magnetic fields. It turns out that the interface shows a large magnetoresistance, which is explained by the presence of local magnetic moments at the interface. Apparently, the conditions at the interface induce such local moments.
Appendix A. The appendix to this thesis is not directly related to interfaces, but discusses the multiband description of the cuprates. The possibility of Cooper pairing induced by the Coulomb interaction between electrons and holes is examined.

1.4 Thin-film growth and sample fabrication

In this section, general growth and sample fabrication techniques will be introduced. These techniques have been used to fabricate all samples and structures described in the following chapters of this thesis.

1.4.1 Pulsed laser deposition

The pulsed laser deposition (PLD) technique has proven to be particularly suitable for the growth of complex oxides.[35] The independent control over the substrate temperature, deposition pressure and flux rate of ablated material enables the growth of these demanding materials. Moreover, the PLD technique allows high oxygen deposition pressure, which is important for the oxygenation of thin films. The PLD set-up is schematically shown in Fig. 1.4. In our system, we make us of a pulsed KrF excimer laser (with a wavelenght of 248 nm). A mask is used to define the beamshape and selects the homogeneous part in the center of the beam. A lens projects the mask image on a target. The laser pulse energy can be adjusted. For a typical value of 100 mJ, the standard deviation of the pulse

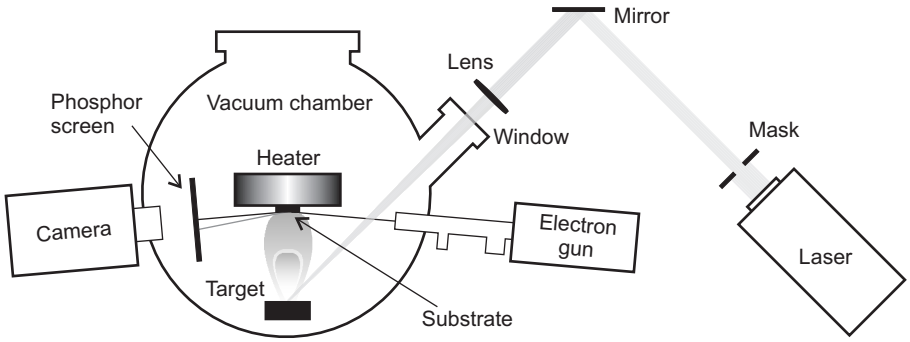

Figure 1.4: Schematic overview of the pulsed laser deposition system.

energy is about 2 mJ. During the 25 ns laser pulse, an energy-density (fluence) in the range of 1–3.5 $\mathrm{J\,cm^{-2}}$ is delivered to the target. In many occasions, the target is a sintered pellet of mixed oxide powders, with the non-oxide elements in ratios corresponding to the stoichiometry of the desired thin film. When the laser hits the target surface, excessive heating of the target surface leads to the ablation of material and the formation of a plasma plume. Details about plume formation can be found in Ref. 36. The kinetic energy of the particles in the plume is high, but interaction with the background gas leads to the thermalization of the plume and the particles reach the substrate with a strongly reduced kinetic energy.[36,37] The substrate is heated to the deposition temperature (in the range of 700–800 °C for LSCO, YBCO, and LSMO). If all deposition conditions are within the correct parameter window, an epitaxial film will grow on the substrate.

With a typical pulse repetition rate of 4 Hz, rather high film growth rates can be achieved. For instance, the growth rate for YBCO with our deposition settings is about 0.4 $\mathrm{nm\,s^{-1}}$. Deposition settings for the various materials used in this thesis, will be provided in the relevant chapters.

In order to obtain good thermal contact between substrate and heater, the substrate is glued to the heater using silver paint. The use of excessive silver paint should be avoided. It was found that when silver paint was left on the heater next to the substrate, conductive outgrowths were formed on the thin-film surface, which we assume to arise from the redeposition of evaporated silver.

1.4.2 Substrate choice and preparation

The choice of the substrate is crucial for the growth of crystalline thin films. The substrate serves as a template for the lattice of the epitaxial film and a good lattice match between lattice and film is required.[40] $SrTiO_3$ (STO) is a widely available substrate, which has a cubic structure at room temperature with lattice constant $a = 3.905$ Å. This makes it suitable for use as a substrate for LSCO, YBCO and

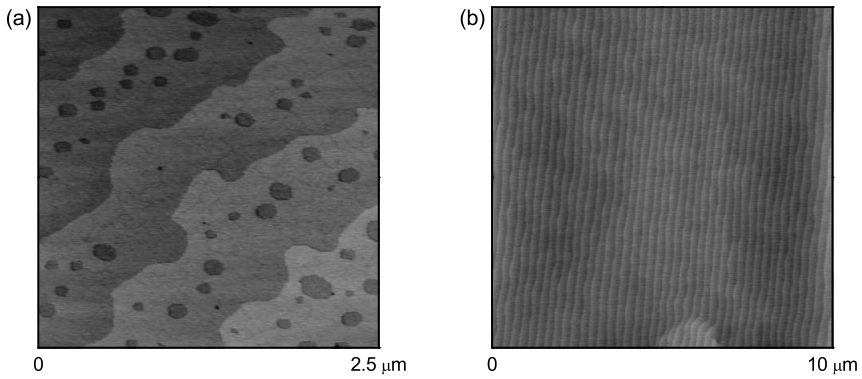

Figure 1.5: Surfaces of $SrTiO_3$ substrates prepared by a buffered HF and annealing treatment.[38,39] The surfaces show unit-cell-height steps as a result of a small miscut with respect to the (001) plane. (a) A small miscut of about 0.03° yields 750 nm wide terraces which are meandering and contain holes of one-unit-cell depth. (b) A larger miscut of about 0.09° results in almost straight 250 nm wide terraces.

LSMO. The lattice mismatches for these materials are 3.3 %, 2.2 %, and 0.5 %, respectively, resulting in tensile strain in the grown films.

Usually, the STO crystal is cut along the (001) plane, which yields *c*-axis growth for LSCO and YBCO. When cut along a different plane it is, within certain limits, possible to induce tilted epitaxial growth.[40,41] In Chapter 5 we have made use of this effect. By growing YBCO on STO (305), i.e., cut along the (305) plane, the YBCO grows with the *c* axis oriented under a 31° angle with respect to the substrate surface.

When using a STO (001) substrate, the smoothness of the substrates as received from the supplier can be enhanced to the atomic level by a buffered HF treatment and annealing.[38,39] In addition, this procedure results in a TiO_2-terminated surface, whereas the STO (001) surface can be either TiO_2 terminated or SrO terminated. Fig. 1.5 shows an atomic force microscopy image of the atomically smooth STO surface prepared by this method. A small miscut with respect to the (001) plane is inevitable in the fabrication of the substrate. This leads to the unit-cell-height substrate steps visible in Fig. 1.5.

1.4.3 Reflective high-energy electron diffraction

Thin-film growth can occur in several growth modes, depending on several parameters such as nucleation and surface diffusion. For a detailed discussion of growth modes, we refer to Refs. 40 and 42. Layer-by-layer (or Frank-Van der Merwe) growth is characterized by the growth of the thin film occurring per unit cell: A unit-cell layer of the grown material tends to be completed over the sample surface, before a new unit-cell layer starts being formed.

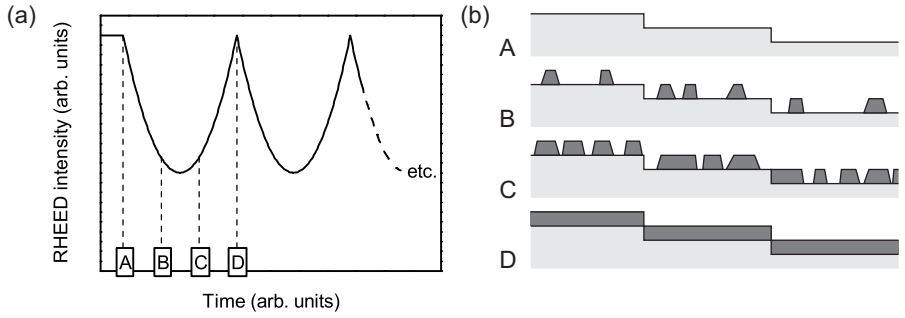

Figure 1.6: (a) Schematic diagram of RHEED during growth. The periodic variation in surface coverage of a stepped substrate surface as sketched in (b) gives rise to RHEED oscillations. Each oscillation corresponds to the growth of one unit cell layer.

Layer-by-layer growth can be monitored effectively using reflective high-energy electron diffraction (RHEED).[40] A high-energy (35 keV) electron beam, grazing over the sample surface, reflects and forms a diffraction pattern on a phosphor screen. During film growth, the intensity of the diffraction spots oscillate over time, as a result of the periodically varying surface coverage. This way, the thickness of the thin film can be controlled by counting the number of grown unit cells.

To apply RHEED to the growth of complex oxides, special precautions[43,44] have to be taken because of the relatively high deposition pressures that are typically needed. A two-stage differential pumping system ensures low pressure at the electron-beam filament and minimizes electron scattering in a high pressure environment.[44]

1.4.4 Thin-film annealing

Despite the use of high oxygen pressure ($pO_2 \approx 0.1$ mbar) during the PLD process, the annealing of as-grown complex-oxide films is important for their oxygenation.[45,46] We apply a multistep annealing process. The first step is an anneal under deposition conditions, after which the temperature is slightly reduced and the oxygen pressure is increased to atmospheric pressure. Subsequently, the temperature is decreased to room temperature over an interval of time, either by ramping the temperature down at a given rate, or by reducing the temperature in several abrupt steps. Specific annealing temperatures, times and pressures will be provided throughout this thesis.

1.4.5 Sample fabrication techniques

In many cases, structuring of the thin film is required, before useful measurements can be performed. Also, it is sometimes necessary to add wiring and insulating layers. To connect the sample electrically to external equipment, aluminum wires

are ultrasonically bonded to gold contact pads, that have to be defined on the sample.

Samples grown by PLD are typically smaller than 1×1 cm^2 to ensure sufficient homogeneity of the film, because of the finite size of the plasma plume. Structures therefore have to be made small; typical length scales are 10–100 μm. Definition of these structures is performed by photolithograpy. Standard techniques are used to define photoresist etch and lift-off masks.

Most structuring of our oxide films is performed by argon ion milling. Etching is performed in a 5×10^{-3} mbar argon environment using an acceleration voltage of 500 V and a beam current of 10–15 mA. Etching is performed in pulses of 8 s, with 12 s between each pulse, to prevent the sample from heating. It is well known that overetching into STO substrates can induce a conducting surface layer in the STO, presumably by the creation of oxygen vacancies. It was experienced that this behavior is quite unpredictable. In some cases, the STO remained insulating despite considerable overetching. In other cases, the STO was found to be conducting irrespective of the depth it was etched into. The surface conductivity after etching might be dependent on which material was etched away, but might also vary for different batches of supplied substrates. It has been reported that for slight overetched conducting surfaces recovery of insulating behavior can be obtained by a short oxygen plasma etch.[47] We have found that in some cases annealing in air at 100 °C for 15 min yields full recovery. In other cases this is completely inadequate and a high pressure (1 bar O_2) reanneal at 600 °C is necessary to restore insulating behavior.

Gold is often used for wiring layers on the sample. Titanium/gold bilayers are sputtered on the sample covered with a predefined lift-off mask. The thin (approximately 2 nm) titanium layer enhances the adhesion of the gold film to the sample. After sputtering, the photoresist lift-off mask and the titanium/gold on top are removed in acetone.

References

[1] I. McNeil, *An encyclopaedia of the history of technology* (Routledge, London, 1990).

[2] C. Jungnickel and R. McCormmach, *Cavendish: the experimental life* (Bucknell, Cranbury, 1999).

[3] Encyclopædia Britannica (2009),"Pieter van Musschenbroek" in Encyclopædia Britannica online: www.britannica.com.

[4] Encyclopædia Britannica (2009), "Charles-Augustin de Coulomb" in Encyclopædia Britannica online: www.britannica.com.

[5] D. van Delft, *Heike Kamerlingh Onnes: een biografie; de man van het absolute nulpunt* (Bakker, Amsterdam, 2005), English title: Freezing physics. Heike Kamerlingh Onnes and the quest for the cold.

[6] J. R. Gavaler, M. A. Janocko, and C. K. Jones, J. Appl. Phys. **45**, 3009 (1974).

[7] J. G. Bednorz and K. A. Müller, Z. Phys. B **64**, 189 (1986).

[8] L. Gao, Y. Y. Xue, F. Chen, Q. Xiong, R. L. Meng, D. Ramirez, C. W. Chu, J. H. Eggert, and H. K. Mao, Phys. Rev. B **50**, 4260 (1994).

[9] J. Bardeen and W. H. Brattain, Phys. Rev. **74**, 230 (1948).

[10] W. Shockley, *Electrons and holes in semiconductors; with applications to transistor electronics* (D. Van Nostrand Company, Inc., Toronto, 1950).

[11] P. Grünberg, R. Schreiber, Y. Pang, M. B. Brodsky, and H. Sowers, Phys. Rev. Lett. **57**, 2442 (1986).

[12] M. N. Baibich, J. M. Broto, A. Fert, F. N. Van Dau, F. Petroff, P. Etienne, G. Creuzet, A. Friederich, and J. Chazelas, Phys. Rev. Lett. **61**, 2472 (1988).

[13] G. Binasch, P. Grünberg, F. Saurenbach, and W. Zinn, Phys. Rev. B **39**, 4828 (1989).

[14] Encyclopædia Britannica (2009), "oxide mineral" in Encyclopædia Britannica online: www.britannica.com.

[15] See e.g. the special issue (3) on high-T_c superconductivity, Nat. Phys. **2**, 133 (2006).

[16] P. A. Lee, Rep. Progr. Phys. **71**, 12501 (2008).

[17] N. F. Mott, Proc. Phys. Soc., London, Sect. A **62**, 416 (1949).

[18] A. Damascelli, Z. Hussain, and Z.-X. Shen, Rev. Mod. Phys. **75**, 473 (2003).

[19] H. Takagi, T. Ido, S. Ishibashi, M. Uota, S. Uchida, and Y. Tokura, Phys. Rev. B **40**, 2254 (1989).

[20] A. Lucarelli, S. Lupi, M. Ortolani, P. Calvani, P. Maselli, M. Capizzi, P. Giura, H. Eisaki, N. Kikugawa, T. Fujita, et al., Phys. Rev. Lett. **90**, 037002 (2003).

[21] E. Dagotto, T. Hotta, and A. Moreo, Phys. Rep. **344**, 1 (2001).

[22] T. Timusk and B. Statt, Rep. Prog. Phys. **62**, 61 (1999).

[23] J. Zaanen and O. Gunnarsson, Phys. Rev. B **40**, 7391 (1989).

[24] J. Tranquada, B. Sternlieb, J. Axe, Y. Nakamura, and S. Uchida, Nature **375**, 561 (1995).

[25] S. A. Kivelson, I. P. Bindloss, E. Fradkin, V. Oganesyan, J. M. Tranquada, A. Kapitulnik, and C. Howald, Rev. Mod. Phys. **75**, 1201 (2003).

[26] D. Reznik, L. Pintschovius, M. Ito, S. Iikubo, M. Sato, H. Goka, M. Fujita, K. Yamada, G. D. Gu, and J. M. Tranquada, Nature **440**, 1170 (2006).

[27] P. W. Anderson and Z. Zou, Phys. Rev. Lett. **60**, 132 (1988).

[28] J. H. Park, E. Vescovo, H. J. Kim, C. Kwon, R. Ramesh, and T. Venkatesan, Nature **392**, 794 (1998).

[29] J. M. De Teresa, A. Barthélémy, A. Fert, J. P. Contour, R. Lyonnet, F. Montaigne, P. Seneor, and A. Vaurès, Phys. Rev. Lett. **82**, 4288 (1999).

[30] H. Yamada, Y. Ogawa, Y. Ishii, H. Sato, M. Kawasaki, H. Akoh, and Y. Tokura, Science **305**, 646 (2004).

[31] L. R. Tagirov, Phys. Rev. Lett. **83**, 2058 (1999).

[32] V. Peña, Z. Sefrioui, D. Arias, C. Leon, J. Santamaria, J. L. Martinez, S. G. E. te Velthuis, and A. Hoffmann, Phys. Rev. Lett. **94**, 057002 (2005).

[33] N. M. Nemes, M. García-Hernández, S. G. E. te Velthuis, A. Hoffmann, C. Visani, J. Garcia-Barriocanal, V. Peña, D. Arias, Z. Sefrioui, C. Leon, et al., Phys. Rev. B **78**, 094515 (2008).

[34] S. Okamoto and A. Millis, Nature **428**, 630 (2004).

[35] D. Dijkkamp, T. Venkatesan, X. D. Wu, S. A. Shaheen, N. Jisrawi, Y. H. Min-Lee, W. L. McLean, and M. Croft, Appl. Phys. Lett. **51**, 619 (1987).

[36] P. R. Willmott and J. R. Huber, Rev. Mod. Phys. **72**, 315 (2000).

[37] S. I. Anisimov, D. Bäuerle, and B. S. Luk'yanchuk, Phys. Rev. B **48**, 12076 (1993).

[38] G. Koster, B. L. Kropman, G. J. H. M. Rijnders, D. H. A. Blank, and H. Rogalla, Appl. Phys. Lett. **73**, 2920 (1998).

[39] M. Kawasaki, K. Takahashi, T. Maeda, R. Tsuchiya, M. Shinohara, O. Ishiyama, T. Yonezawa, M. Yoshimoto, and H. Koinuma, Science **266**, 1540 (1994).

[40] M. Ohring, *Materials Science of thin films: deposition and structure* (Academic Press, San Diego, 2002), 2nd ed.

[41] W. A. M. Aarnink, E. Reuvekamp, M. A. J. Verhoeven, M. V. Pedyash, G. J. Gerritsma, A. van Silfhout, H. Rogalla, and T. W. Ryan, Appl. Phys. Lett. **61**, 607 (1992).

[42] H. Lüth, *Solid Surfaces, interfaces and thin films* (Springer, Berlin, 2001), 4th ed.

[43] H. Karl and B. Stritzker, Phys. Rev. Lett. **69**, 2939 (1992).

[44] G. J. H. M. Rijnders, G. Koster, D. H. A. Blank, and H. Rogalla, Appl. Phys. Lett. **70**, 1888 (1997).

[45] D. K. Lathrop, S. E. Russek, and R. A. Buhrman, Appl. Phys. Lett. **51**, 1554 (1987).

[46] S. I. Shah, Appl. Phys. Lett. **53**, 612 (1988).

[47] C. Beekman, I. Komissarov, M. Hesselberth, and J. Aarts, Appl. Phys. Lett. **91**, 062101 (2007).

Chapter 2 Indications for static stripe stabilization in $La_{2-x}Sr_xCuO_4$ ($0.10 < x < 0.13$) by an epitaxial-strain-enforced lattice modification

Abstract

We have studied the magnetoresistance and conductance anisotropy of underdoped ($0.10 < x < 0.13$) and optimally doped ($x = 0.15$) $La_{2-x}Sr_xCuO_4$ (LSCO) thin films grown on $SrTiO_3$ (STO) substrates. For $0.10 < x < 0.13$, a linear term is present in the magnetoresistance, which suddenly disappears at a temperature slightly below the cubic-tetragonal phase transition of the STO substrate (105 K). In LSCO single crystals, this linear magnetoresistance term has been observed by Kimura *et al.*[1] for temperatures down to 50 K for $0.12 < x < 0.13$ and has been associated with the presence of fluctuating stripes. The conductance anisotropy of our underdoped LSCO thin films sensitively responds to the STO phase transition in a way that suggests the appearance of static stripes below 105 K. We thus infer that the phase transition of the STO substrate enforces a lattice modification in the epitaxially connected LSCO film, which induces the pinning of fluctuating stripes.

2.1 Introduction

Ever since the discovery of the high-temperature superconductors, their normal state transport properties have been studied widely. Many of these show unusual behavior,[2] and the understanding of them might be crucial to our comprehension of the high-temperature superconductors. Intriguing behavior is observed for the La-based cuprates around the "1/8 anomaly". At doping $x = 0.125$, superconductivity is suppressed[3] by the competing static stripe phase,[4,5] which develops under the condition of a phase transition to the low-temperature tetragonal (LTT) phase at low temperatures. It is due to the tight competition between the superconducting and the stripe phases that a minor influence like a small structural deformation can have such an impact. By studying a thin layer of LSCO on an STO substrate we demonstrate that the ordering of stripes can be influenced from the outside.

Below 105 K, the STO substrate undergoes a structural transition from the cubic to the tetragonal phase, which through the epitaxial connection to the LSCO film leads to a small structural modification of the LSCO. We then find in our transport measurements the disappearance of the fingerprints of fluctuating stripe order and the onset of a contribution to conductance anisotropy, the latter strongly indicating the appearance of a static stripe phase.

Diffraction measurements leave no doubt that stripe charge and spin order occurs for $La_{1.6-x}Nd_{0.4}Sr_xCuO_4$ (Ref. 5) and $La_{2-x}Ba_xCuO_4$ (LBCO) (Refs. 6,7) in the LTT phase around doping $x = 0.125$. The LTT phase provides a pinning potential for the stripes through the specific tilting pattern of the oxygen octahedra in these materials.[5] $La_{2-x}Sr_xCuO_4$ (LSCO) single crystals do not exhibit a phase transition to the LTT phase but remain in the low-temperature orthorhombic (LTO) phase at low temperatures. It is often suggested that in the absence of pinning, stripes occur in a fluctuating form.[5,8] Experimental indications for the presence of fluctuating stripes in LSCO come from optical conductivity measurements[9,10] and phonon anomalies.[11] LSCO shows a partial suppression of the superconducting transition temperature T_c around $x = 0.125$.[12] Dynamic[13–16] as well as static[13,17–19] incommensurate spin correlations were found for LSCO around $x = 0.12$. The static magnetic correlations showed the largest correlation length for $x = 0.12$,[17] at which doping they persist up to the highest temperature of about 30 K. Dynamic spin correlations were measured up to room temperature.[13,14]

In the underdoped regime, Kimura *et al.*[1] revealed for LSCO single crystals anomalous behavior of the magnetoresistance (obtained with the magnetic field applied perpendicular to LSCO's crystallographic *ab* plane and the current parallel to the *ab* plane) at two doping levels: (1) at $x = 0.11$ the magnitude of the MR shows a sudden suppression. (2) Near $x = 0.13$ a linear term adds to the magnetoresistance, which is quadratic for all other doping levels. The quadratic magnetoresistance vanishes rapidly above 100 K and is (partly) attributed to superconducting fluctuations. The linear term survives up to the highest temperature measured (175 K). Kimura *et al.* explained the suppressed magnetoresistance at $x = 0.11$ by the suppression of superconductivity associated with the 1/8 anomaly. At the same time, a relation between the 1/8 anomaly and the linear magnetoresistance around $x = 0.13$ was suggested, the linear magnetoresistance being the fingerprint of fluctuating stripes. Our data on LSCO thin films help settle this issue. We have measured linear magnetoresistance up to 300 K for the entire doping range $x = 0.10$–0.13. The linear term in the magnetoresistance disappears below 90 K. Such distinction from single-crystal data is attributed to the presence of the STO substrate, which influence on the LSCO film has been clearly established.

2.2 Experimental details

Epitaxial thin films with a thickness of 50 nm were grown by pulsed laser ablation (PLD) from a sintered LSCO target with a Sr content of $x = 0.15$. Prior to deposition, the (001) $SrTiO_3$ (STO) substrates were chemically treated[20] and annealed for at least two hours at 950 °C in an oxygen environment. Atomically flat surfaces with unit-cell-height substrate steps were confirmed by atomic force microscopy (AFM) measurements. The films were deposited in a 0.13 mbar oxygen environment at a temperature of 700 °C. The laser fluence was 1.2 $\mathrm{J\,cm^{-2}}$. The film growth was monitored by reflective high-energy electron diffraction, which showed intensity oscillations, indicative for layer-by-layer growth. The thin films were annealed for 15 minutes at the deposition pressure and temperature, after which the oxygen pressure was increased to 1 atm, in which the films were annealed 15 minutes at 600 °C, 30 minutes at 450 °C, and subsequently cooled down to room temperature. Hall bars were defined by photolithography and argon ion milling on three different samples: S1, S2, and S3. S1 contained multiple Hall bars, four of them labeled A–D. The Hall bars on S1 have varying orientations with respect to the STO [100] axis, which will be used for studying anisotropy in Sec. 2.3.3. S2 and S3 were grown simultaneously, their substrates were cut out of a single, larger substrate. Magnetoresistance and Hall measurements were performed with magnetic fields applied perpendicular to the thin film.

In order to perform doping-dependent measurements, we employed the stoichiometry variations that occur within the PLD plasma plume. The Sr/La ratio decreases when moving away from the center of the plume [see Fig. 2.1(a)], as a result of the atomic weight dependence of the plume confinement by the oxygen background gas. The Hall bar on S3 was positioned in the center of the spot, the distance S2–S3 and the distance between Hall bars A and C on S1 were about 7 mm. In Fig. 2.1(b) we show temperature-dependent resistance (RT) measurements for the different samples. The superconducting transition temperature T_c, as determined by a zero-resistance criterion, varied between 13 and 23 K. A midpoint temperature, determined in the middle of the superconducting transition, of 26 K for S3 compares well to the value of 27 K that was reported for optimally doped ($x = 0.15$) LSCO on STO.[22]

We have used the Hall effect to estimate the local doping level x for the various Hall bars. It is well known that for LSCO the Hall coefficient R_H cannot simply be used to determine the carrier density.[21] We therefore interpolated the 50 K single-crystal Hall-coefficient data from Ando *et al.*,[21] to estimate x. The result as shown in grey in Fig. 2.1(c) correlates well with T_c, as we resolve a part of the superconducting dome, characteristic for high-T_c superconductors. It must be emphasized that there is some uncertainty in the value of x, since we compare single-crystal data with thin-film data. We argue that the whole curve should be shifted to larger x by a value of 0.02 because we expect $x = 0.15$ for S3. Furthermore, when comparing the datapoints to the domeshape that is drawn in

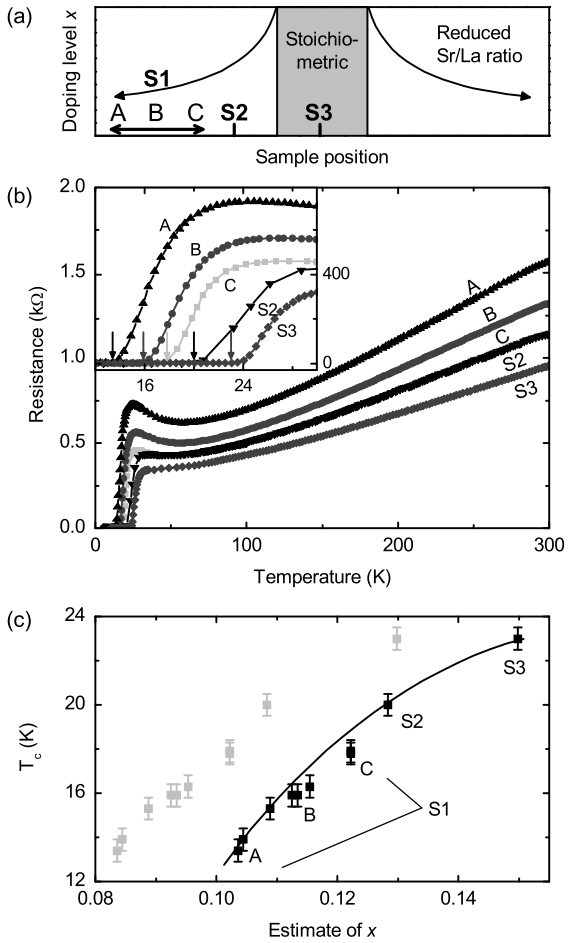

Figure 2.1: (a) Schematical drawing of the stoichiometry variation as a function of sample position with respect to the center of the plasma plume. Away from the center, the Sr/La ratio is reduced. (b) RT-curves for three Hall bars on S1 and Hall bars on S2 and S3. The inset shows the behavior around T_c; arrows denote T_c. (c) An estimate of the doping level x for the various Hall bars was obtained by interpolating single-crystal Hall data from Ando *et al.*[21] (grey datapoints). The estimate correlates well with the local value of T_c. The fixed point $x = 0.15$ for S3 suggests a shift by 0.02. A small suppression of T_c is then observed for $x = 0.115$–0.125. The curve through the datapoints is a guide to the eye.

the figure, we observe a small suppression of T_c which falls in the range $x = 0.115$–0.125 for the shifted datapoints. Such a suppression is likely related to the 1/8 anomaly, which further substantiates the shift by 0.02. The suppression is not an artifact of the interpolation procedure; when we plot T_c directly against R_H^{-1}, we find the suppression as well.

2.3 Results

2.3.1 Magnetoresistance

We have measured the magnetoresistance, $[R(H) - R(0)]/R(0)$, H being the magnetic field, for our Hall bars. For optimal doping ($x = 0.15$), the magnetoresistance decreases monotonically as a function of temperature and vanishes almost completely between 140 and 200 K; see Fig. 2.2(a). In the doping range $x = 0.10$–0.13 the magnetoresistance is doping independent and shows a non-monotonic temperature dependence [Fig. 2.2(b,c)]. The temperature evolution is peculiar: the largest magnetoresistance is observed at 50 K. Between 50 and 80 K, the magnetoresistance decreases. Between 80 and 110 K, the magnetoresistance increases and then decreases again up to room temperature. In addition, the functional form changes between 80 and 110 K. At 50, 70, and 80 K, the magnetoresistance is purely quadratic as demonstrated by the parabolic fits in Fig. 2.2(c). However, at 110 K, the data cannot be fit by a parabola, because of a pronounced linear contribution to the magnetoresistance. The onset temperature of the linear term was pin-pointed at 90 K for S1B, the magnetoresistance at 85 K still being purely parabolic and at 95 K–140 K linear-like and temperature independent.

We associate the linear magnetoresistance for $x = 0.10$–0.13 in the temparature range 90–300 K with that observed by Kimura *et al.*[1] in single crystals with doping levels $x = 0.12$ and $x = 0.13$. The quadratic behavior for $x = 0.15$ is identical to the behavior observed for $x = 0.15$ crystals. This further confirms the estimated doping levels as presented in Fig. 2.1(c). The magnitude of our magnetoresistance compares well to the single crystal data. Also, the temperature dependence of the data shows similarities. The parabolic magnetoresistance vanishes rapidly above 100–140 K, while the linear term shows a much weaker temperature dependence. A marked difference between the single-crystal and the thin-film data is the vanishing of the linear term below 90 K in the latter.

A second difference is the doping independence of the linear magnetoresistance for thin films in the range $x = 0.10$–0.13, whereas Kimura *et al.*[1] found for single crystals, apart from linear magnetoresistance near $x = 0.13$, a suppressed quadratic magnetoresistance at $x = 0.11$. Notice that even if we take the unshifted estimate for the doping levels in Fig. 2.1, which follow directly from interpolation of single-crystal data, $x = 0.11$ is covered. Kimura *et al.* suggested that either the suppressed magnetoresistance at $x = 0.11$ or the linear magnetoresistance near $x = 0.13$ is related to the 1/8 anomaly and the presence of fluctuating stripes.

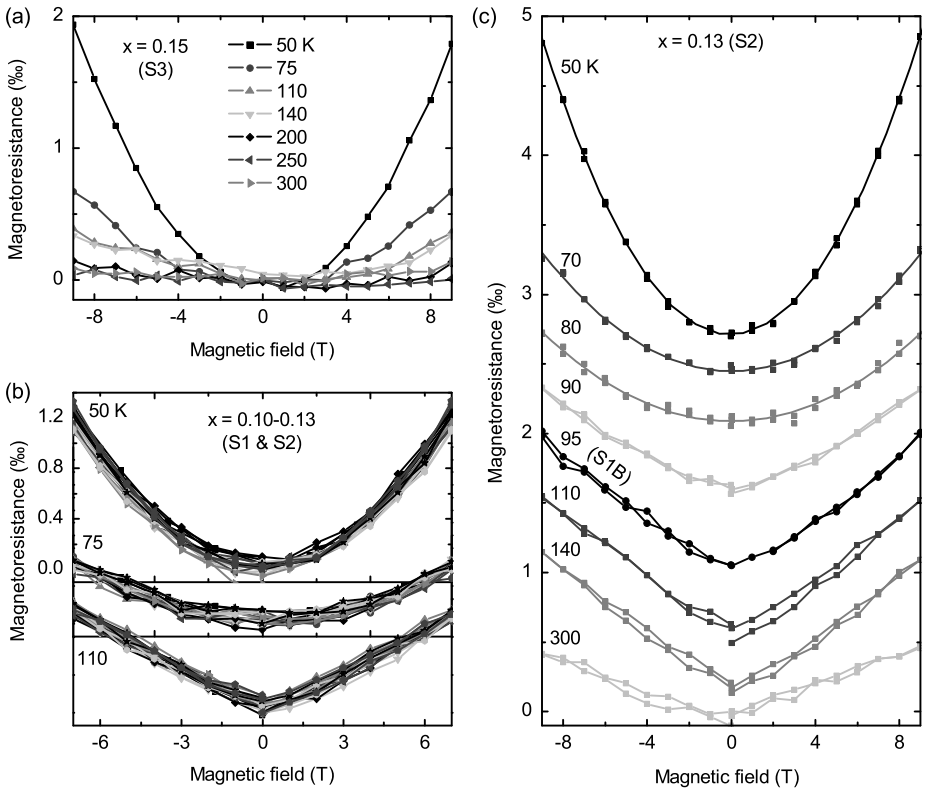

Figure 2.2: (a) The magnetoresistance for $x = 0.15$ (S3) decreases monotonically with temperature. (b) The magnetoresistance is independent of x in the doping range $x = 0.10$–0.13. Curves for 50 K, 75 K and 110 K are all plotted on the same scale. A non-monotonic temperature dependence is observed. (c) Magnetoresistance for $x = 0.10$–0.13 (measured on S2 and S1B for the 95 K curve) for various temperatures. The curves are offset for clarity. A linear term adds to the magnetoresistance for temperatures of 90 K and higher.

With only the linear magnetoresistance to explain, we propose that the linear magnetoresistance in the doping range $x = 0.10$–0.13 is caused by fluctuating stripes.

Because of the magnetic nature of stripes, it is reasonable to assume that stripes would have an impact on an observable as the magnetoresistance. The magnetic field is known to enhance static magnetic order in LSCO,[19,23] and might influence fluctuating stripes as well. Experiments[10,11,13,14] and theory[24] indicate the existence of fluctuating stripes over the entire temperature range where we observe linear magnetoresistance. The loss of linear magnetoresistance below 95 K would within this viewpoint be induced either by the pinning, or by the suppression of fluctuating stripes.

2.3.2 Visualizing the STO phase transition

We will proceed with investigating whether the disappearance of linear magnetoresistance below 90 K could be related to the STO phase transition from cubic to tetragonal below 105 K.[25] The deviation from the cubic unit cell in the tetragonal phase is small [$c/a = 1.00056$ at 56 K (Ref. 26)]. However, since the LSCO film is epitaxially connected to the substrate, the sudden change of the substrate's lattice is fully passed on to the LSCO film. Moreover, since the STO c axis in the tetragonal phase can align with the LSCO a and b axes, the phase transition can break a–b symmetry in the LSCO. The mentioned ratio $c/a = 1.00056$ might seem small, but is only 3–7 times smaller than the lattice-parameter changes associated with the LTO-LTT phase transition for LBCO: $a_{\mathrm{LTT}}/a_{\mathrm{LTO}} = 1.0017$ and $b_{\mathrm{LTO}}/a_{\mathrm{LTO}} = 1.0036$.[27] Yet, for LBCO this small modification represents a significant change in the tilting direction of the oxygen octahedra, providing the necessary pinning potential to stabilize the static stripe phase.[5]

A direct indication for the influence of the phase transition on the properties of the LSCO comes from the Hall offset $R_{\mathrm{xy},0}$. It is common that Hall measurements show a small offset, i.e., a Hall signal is measured *without* applying a magnetic field. The cause of this offset in our specific case will be discussed in Sec. 2.3.3. The temperature dependence of the Hall offset is shown in Fig. 2.3(a). For some of the Hall bars, we observe a small anomaly near 105 K; two of them are marked by arrows in the figure. To visualize the anomalies more clearly, we have plotted the numerical derivatives of the Hall offsets $\mathrm{d}R_{\mathrm{xy},0}/\mathrm{d}T$ for all Hall bars in Fig. 2.3(b). All derivatives show a clear and sharp transition, exactly at 105 K. Above this temperature, the derivatives are smooth, whereas below 105 K, they show large variations with temperature. We interpret these variations as resulting from domains in the STO, which are likely in continuous motion as function of temperature. We accept Fig. 2.3(b) as evidence of the influence of the STO structural phase transition on the LSCO film. We do not observe anomalies when differentiating the RT-curves in Fig. 2.1(b). The subtle changes induced by the phase transition are probably hidden in the large signal that is due to the longitudinal resistance itself. Interestingly, we also do not observe anomalies when differentiating the Hall offset for $x = 0.15$. This indicates a connection between the linear magnetoresistance and the Hall offset anomalies. If linear magnetoresistance is related to stripe ordering, the Hall offset anomaly likely arises from these stripes as well. It is therefore useful to investigate the relation between the Hall offset anomaly and the orientation of the Hall bar.

2.3.3 Anisotropy

If the Hall offset anomaly arises from stripes, we anticipate that it reflects some of the directional nature of these stripes.[28,29] The small magnitude of the anomalies in Fig. 2.3(a) indicate that a possible modification of the conduction due to stripes is small. However, as we expect a sudden onset at 105 K, we might recognize a

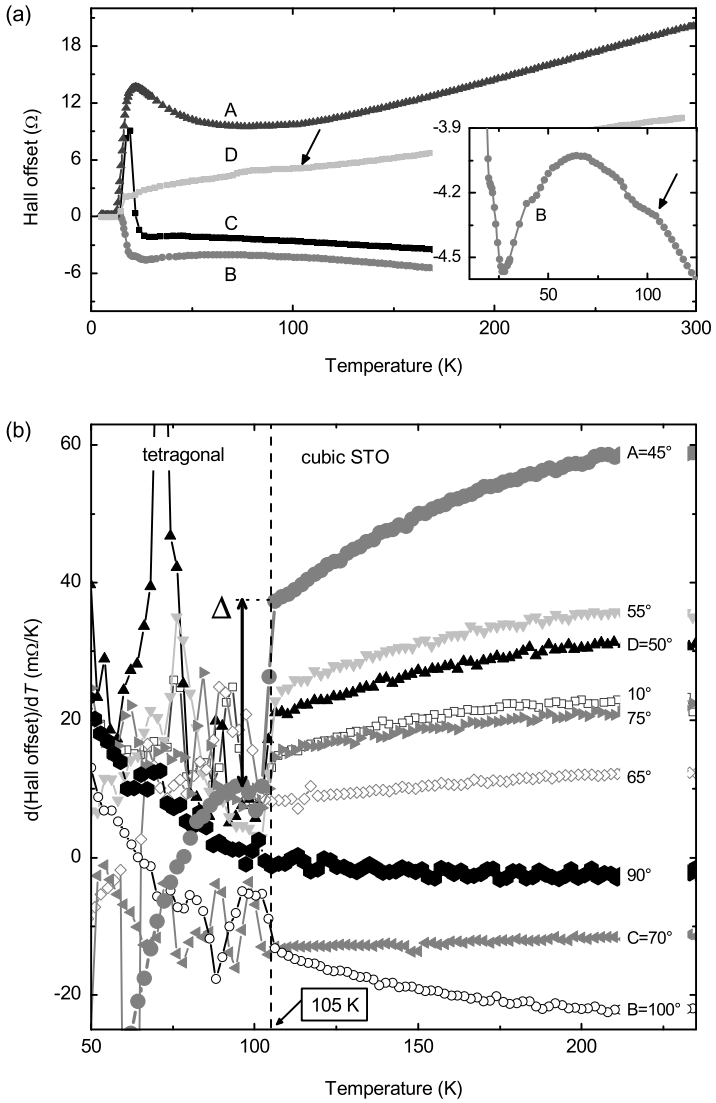

Figure 2.3: (a) Hall offset as function of temperature. The inset shows an enlarged view of curve B. Arrows indicate anomalies in the Hall offset. (b) Derivatives of the Hall offsets for various Hall bars. A clear transition in the behavior is visible at 105 K, corresponding to the cubic-tetragonal phase transition of the STO substrate. The angles denote the orientation of the Hall bars with respect to the STO [100] axis.

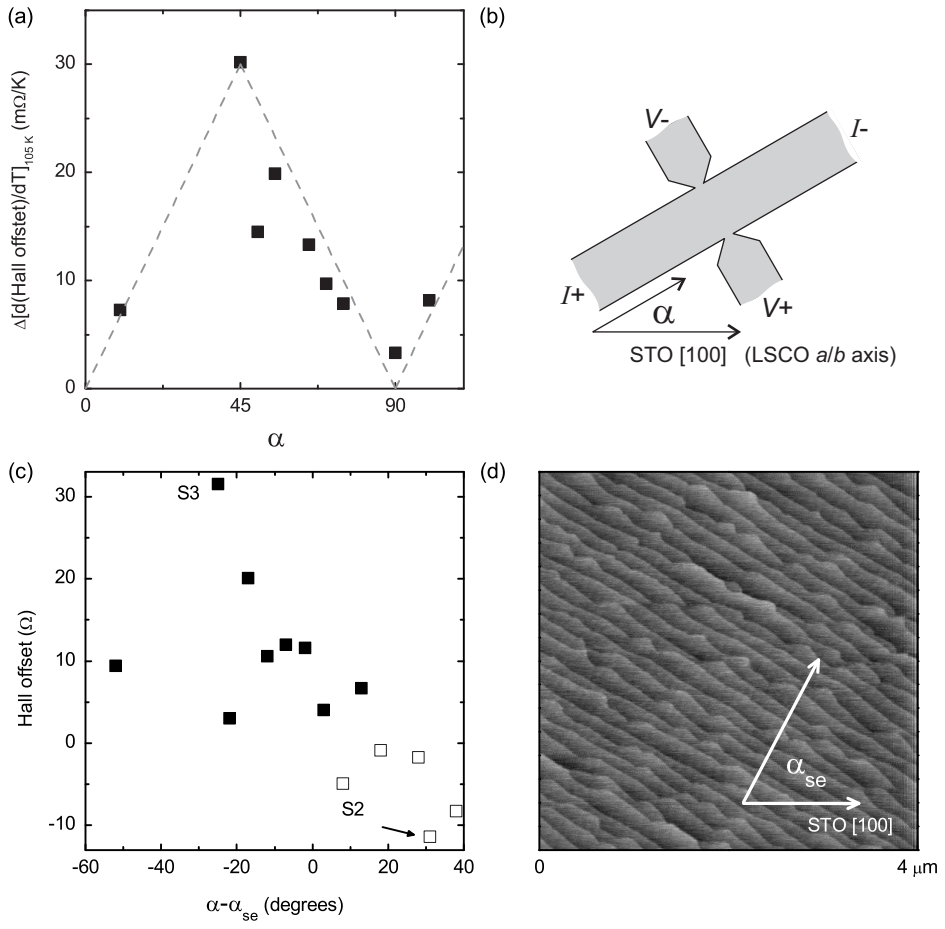

Figure 2.4: (a) The jump Δ in the Hall offset derivative observed in Fig. 2.3(b) as function of the Hall-bar orientation as defined in (b). The dashed line in (a) sketches the expected orientation dependence for Δ, if it reflects the onset of stripes along the LSCO a or b axes. (c) Hall offset at room temperature as function of Hall-bar orientation, relative to the step-edge orientation. Positive (negative) offsets are indicated by filled (open) squares. A sign change is observed between 8 and 13°. On the right, a 4×4 μm^2 AFM image of the substrate of S1 is shown. The step-edge orientation α_{se} with respect to the STO [100] axis is 62° for S1, 39° for S2, and 115° for S3.

possible stripe contribution to anisotropic conductivity most easily in $dR_{xy,0}/dT$ at 105 K. We therefore plotted in Fig. 2.4(a) the observed jumps $\Delta(dR_{xy,0}/dT)$ at 105 K as a function of Hall bar orientation, defined by α as shown in Fig. 2.4(b). It is clear that $\Delta(dR_{xy,0}/dT)$ is largest for the 45° orientation, smallest for the 90° orientation and systematically changes with orientation in between. Note also the large variations with temperature in $dR_{xy,0}/dT$ in Fig. 2.3(b) for orientations close to 45°, which are nearly absent for 90°. This observed anisotropy can readily be expected for conducting (or insulating) unidirectional stripes along the LSCO a or b axes. These are the expected stripe ordering orientations for static stripes.[5]

Thus, the presence of linear magnetoresistance for $x = 0.10$–0.13 is concomitant with a changing conductance anisotropy at the temperature of the STO cubic-tetragonal phase transition, which has the symmetry of the crystal structure. Furthermore, at a slightly lower temperature the linear magnetoresistance disappears. Before we further discuss these findings, we will now first consider the origin of the Hall offset itself. Since the Hall offset is too large to arise from misalignment of the contacts, given the resolution of the applied photolithography technique, there must be some source of anisotropy in the sample (to which the suggested contribution from stripes is a small addition). Possibilities are sample inhomogeneity and the stepped character of the STO substrate, which could nucleate antiphase boundaries. The step-edge orientation α_{se} (their normal direction with respect to the STO [100] axis) and average terrace width for the three substrates were determined by AFM measurements. They are 62° and 216 nm, 39° and 162 nm, and 115° and 85 nm for S1, S2, and S3, respectively. A 14° variance in step-edge orientation was observed over a distance of 1 cm. In Fig. 2.4(c), we plotted the Hall offset at room temperature as function of $\alpha - \alpha_{SE}$: the Hall-bar orientation relative to the step-edge direction. For S1, the Hall offset crosses zero for $\alpha - \alpha_{se}$ of 8–13°, which is within the range of the variance from the expected value of 0° for the step-edge scenario. The crossing angle is inconsistent with a resistance-gradient induced offset, arising from the carrier-density variance over the sample, because the gradient points along the STO [100] axis. The signs of the Hall offsets for both S2 and S3 are consistent with the step-edge scenario. Moreover, the largest offset is observed for S3, which features the smallest terrace width. We therefore attribute the anisotropy underlying the Hall offset to step-edge induced antiphase boundaries. We like to note that the linear magnetoresistance is unrelated to the antiphase boundaries, since we do not observe any scaling of the linear magnetoresistance with the Hall offset, or the Hall bar orientation. There is also no correlation between the magnitude of the Hall offset itself and the magnitude of $\Delta(dR_{xy,0}/dT)$ at 105 K.

2.4 Discussion

While we firmly established the influence of the cubic-tetragonal phase transition in the STO on the conductance anisotropy of the LSCO, there is still some

uncertainty whether the phase transition also induces the loss of linear magnetoresistance, because of the 15 K temperature difference between the two phenomena. This point might be clarified by measurements by Alefeld[30] who found an increasing tetragonality as a function of temperature below the STO structural phase transition. At 90 K, the ratio c/a is about 1.0003, which apparently needs to be exceeded before the linear term in the magnetoresistance vanishes. In the temperature range 90–105 K, fluctuating and static stripes might coexist, the former ultimately disappearing below 90 K due to the increasing tetragonality of the STO substrate.

An alternative scenario in which the STO phase transition induces stripe suppression, rather than pinning, is unlikely. First of all, this scenario cannot explain the observed anisotropy, since fluctuating stripes do not exhibit a preferential orientation. It is also difficult to explain the temperature-dependent variations in $\mathrm{d}R_{\mathrm{xy},0}/\mathrm{d}T$ below 105 K in the absence of stripes. Furthermore, it can be argued that the small lattice parameter change induced by the STO phase transition unlikely suppresses the electron-electron interactions responsible for fluctuating stripe order, but rather modifies the appearance of the arising electronic phase through the alteration of the crystal symmetry.

Interestingly, the occurrence of a static stripe phase below 105 K would imply the coexistence of static stripes and superconductivity in our thin films. This perhaps indicates that static stripes in LSCO on STO are weak compared to static stripes in LBCO, where superconductivity is strongly suppressed near $x = 0.125$.[3] However, the interplay between superconductivity, stripes and lattice effects is a longstanding issue and has never been completely resolved.[31] In LBCO and $La_{1.6-x}Nd_{0.4}Sr_xCuO_4$, the doping level x not only influences stripe ordering but also the LTO/LTT phase transition.[32] The epitaxial-strain-enforced lattice modification resulting from a substrate phase transition provides a means of disentangling structural and stripe effects on superconductivity, since the lattice symmetry is imposed from the outside and can be applied independently of x.

2.5 Conclusion

It has been shown that linear magnetoresistance in LSCO $x = 0.10$–0.13 thin films disappears at a temperature slightly below the cubic-tetragonal phase transition of the STO substrate at 105 K. This phase transition also induces a change in conductance anisotropy for this doping. We have argued that both effects can be explained by the pinning of fluctuating stripes, induced by the epitaxial-strain-enforced structural modification. Direct measurements of spin or charge correlations on LSCO thin films, would be an interesting challenge. Our results open up the possibility of exploiting epitaxial-strain-enforced structural changes by choosing appropriate substrates in which phase transitions can be tuned at will. Candidates are the (Ca/Sr)TiO_3 and (Ca/Ba)TiO_3 systems.[33,34]

References

[1] T. Kimura, S. Miyasaka, H. Takagi, K. Tamasaku, H. Eisaki, S. Uchida, K. Kitazawa, M. Hiroi, M. Sera, and N. Kobayashi, Phys. Rev. B **53**, 8733 (1996).

[2] J. R. Schrieffer and J. S. Brooks, eds., *Handbook of high-temperature superconductivity: theory and experiment* (Springer, 2007).

[3] A. R. Moodenbaugh, Y. Xu, M. Suenaga, T. J. Folkerts, and R. N. Shelton, Phys. Rev. B **38**, 4596 (1988).

[4] J. Zaanen and O. Gunnarsson, Phys. Rev. B **40**, 7391 (1989).

[5] J. Tranquada, B. Sternlieb, J. Axe, Y. Nakamura, and S. Uchida, Nature **375**, 561 (1995).

[6] M. Fujita, H. Goka, K. Yamada, and M. Matsuda, Phys. Rev. Lett. **88**, 167008 (2002).

[7] P. Abbamonte, A. Rusydi, S. Smadici, G. D. Gu, G. A. Sawatzky, and D. L. Feng, Nat. Phys. **1**, 155 (2005).

[8] S. A. Kivelson, I. P. Bindloss, E. Fradkin, V. Oganesyan, J. M. Tranquada, A. Kapitulnik, and C. Howald, Rev. Mod. Phys. **75**, 1201 (2003).

[9] M. Dumm, D. N. Basov, S. Komiya, Y. Abe, and Y. Ando, Phys. Rev. Lett. **88**, 147003 (2002).

[10] A. Lucarelli, S. Lupi, M. Ortolani, P. Calvani, P. Maselli, M. Capizzi, P. Giura, H. Eisaki, N. Kikugawa, T. Fujita, et al., Phys. Rev. Lett. **90**, 037002 (2003).

[11] D. Reznik, L. Pintschovius, M. Ito, S. Iikubo, M. Sato, H. Goka, M. Fujita, K. Yamada, G. D. Gu, and J. M. Tranquada, Nature **440**, 1170 (2006).

[12] H. Takagi, T. Ido, S. Ishibashi, M. Uota, S. Uchida, and Y. Tokura, Phys. Rev. B **40**, 2254 (1989).

[13] R. J. Birgeneau, Y. Endoh, K. Kakurai, Y. Hidaka, T. Murakami, M. A. Kastner, T. R. Thurston, G. Shirane, and K. Yamada, Phys. Rev. B **39**, 2868 (1989).

[14] G. Aeppli, T. E. Mason, S. M. Hayden, H. A. Mook, and J. Kulda, Science **278**, 1432 (1997).

[15] T. Suzuki, T. Goto, K. Chiba, T. Shinoda, T. Fukase, H. Kimura, K. Yamada, M. Ohashi, and Y. Yamaguchi, Phys. Rev. B **57**, R3229 (1998).

[16] K. Yamada, C. H. Lee, K. Kurahashi, J. Wada, S. Wakimoto, S. Ueki, H. Kimura, Y. Endoh, S. Hosoya, G. Shirane, et al., Phys. Rev. B **57**, 6165 (1998).

[17] H. Kimura, K. Hirota, H. Matsushita, K. Yamada, Y. Endoh, S.-H. Lee, C. F. Majkrzak, R. Erwin, G. Shirane, M. Greven, et al., Phys. Rev. B **59**, 6517 (1999).

[18] Y. S. Lee, R. J. Birgeneau, M. A. Kastner, Y. Endoh, S. Wakimoto, K. Yamada, R. W. Erwin, S.-H. Lee, and G. Shirane, Phys. Rev. B **60**, 3643 (1999).

[19] S. Katano, M. Sato, K. Yamada, T. Suzuki, and T. Fukase, Phys. Rev. B **62**, R14677 (2000).

[20] G. Koster, B. L. Kropman, G. J. H. M. Rijnders, D. H. A. Blank, and H. Rogalla, Appl. Phys. Lett. **73**, 2920 (1998).

[21] Y. Ando, Y. Kurita, S. Komiya, S. Ono, and K. Segawa, Phys. Rev. Lett. **92**, 197001 (2004).

[22] H. Sato and M. Naito, Physica C **274**, 221 (1997).

[23] B. Lake, H. M. Rønnow, N. B. Christensen, G. Aeppli, K. Lefmann, D. F. McMorrow, P. Vorderwisch, P. Smeibidl, N. Mangkorntong, T. Sasagawa, et al., Nature **415**, 299 (2002).

[24] V. J. Emery, S. A. Kivelson, and O. Zachar, Phys. Rev. B **56**, 6120 (1997).

[25] E. Courtens, Phys. Rev. Lett. **29**, 1380 (1972).

[26] F. W. Lytle, J. Appl. Phys. **35**, 2212 (1964).

[27] S. Katano, J. A. Fernandez-Baca, S. Funahashi, N. Môri, Y. Ueda, and K. Koga, Physica C **214**, 64 (1993).

[28] Y. Ando, A. N. Lavrov, and K. Segawa, Phys. Rev. Lett. **83**, 2813 (1999).

[29] Y. Ando, K. Segawa, S. Komiya, and A. N. Lavrov, Phys. Rev. Lett. **88**, 137005 (2002).

[30] B. Alefeld, Z. Physik **222**, 156 (1969).

[31] Q. Li, M. Hücker, G. D. Gu, A. M. Tsvelik, and J. M. Tranquada, Phys. Rev. Lett. **99**, 067001 (2007).

[32] M. K. Crawford, R. L. Harlow, E. M. McCarron, W. E. Farneth, J. D. Axe, H. Chou, and Q. Huang, Phys. Rev. B **44**, 7749 (1991).

[33] C. J. Ball, B. D. Begg, D. J. Cookson, G. Thorogood, and E. R. Vance, J. Solid State Chem. **139**, 238 (1998).

[34] T. Mitsui and W. B. Westphal, Phys. Rev. **124**, 1354 (1961).

Chapter 3 Tunnel spectroscopy on a high-T_c superconductor

Abstract

$La_{2-x}Sr_xCuO_4$ (LSCO) based tunnel junctions have been fabricated. The emphasis has been on planar junctions with *in situ* grown epitaxial $SrTiO_3$ barriers. Junctions are characterized by a linear conductance as a function of bias voltage. In many occasions the spectra are asymmetric and sometimes contain a gap-like feature. The results can be explained reasonably well by assuming that inelastic tunneling takes place in these junctions. The gap-like feature might be related to the pseudogap. The results indicate that charge carriers tunnel into a non-superconducting LSCO surface layer, adjacent to the barrier.

3.1 Introduction

3.1.1 Tunneling with conventional superconductors

Tunnel experiments have played a decisive role in the understanding of conventional (low-T_c) superconductors. Already since 1940, strong indications for the presence of an energy gap Δ in superconductors had been collected from several *indirect* experiments.[1] The importance of such a gap was proven by the microscopic theory for superconductivity, developed by Bardeen, Cooper and Schrieffer (BCS) in 1957.[2] Shortly after the formulation of the BCS theory, Giaever revealed the energy gap *directly*, by electron tunneling.[3] Developments followed quickly then. The energy dependence of the density of states, as well as the temperature and magnetic field dependence of the energy gap, all appeared to be well-described by the BCS-theory.[4] However, in 1962, measurements were conducted for the first time below 1 K and some small divergences from the theory were found in the electron density of states: instead of being smooth for energies larger than the gap, it showed "some bumps".[5] In the meantime, the BCS-theory had been generalized to the regime of strong coupling between electrons and phonons, for which the energy-dependent phonon density of states $F(\omega)$ and effective electron-phonon coupling function $\alpha^2(\omega)$ had to be taken into account explicitly.[6] It was soon realized that the structure observed for energies $E > \Delta$ in the electron density of

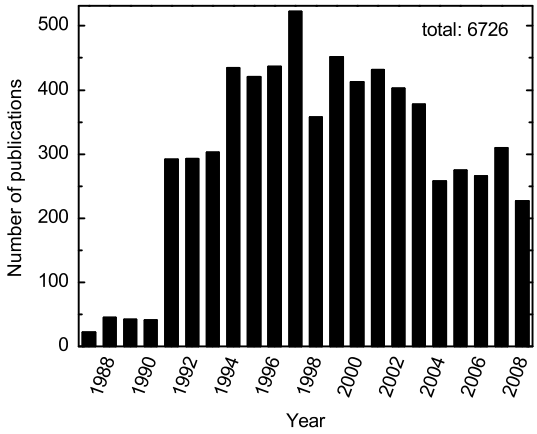

Figure 3.1: Number of publications on tunnel experiments and junction technology based on high-T_c superconductors in the period 1987-2008.[30]

states presented a signature of the phonons involved in superconductivity.[7,8] In 1965, McMillan and Rowell[9] published a procedure for inverting the gap equation to obtain $\alpha^2(\omega)F(\omega)$ from the experimentally determined electronic density of states and applied this procedure to the tunnel spectrum of lead. The good fit with the independently determined phonon spectrum of lead provided convincing confirmation of the theory of phonon mediated superconductivity.

3.1.2 Tunneling with high-T_c superconductors

The immediate and overwhelming success of tunnel experiments with low-T_c superconductors has inspired many to attempt similar experiments with high-T_c superconductors, starting soon after their discovery in 1986.[10–12] In Fig. 3.1, the number of publications per year concerning junctions and tunnel experiments with high-T_c materials is depicted. Various techniques were applied for the junction preparation, not only based on thin-film techniques,[13–17] but also on scanning tunneling microscopy (STM) (for a review, see Ref. 18), point contacts,[19,20] grain boundaries[21,22] or break junctions. Among the successes were the detection of surface bound states,[13–17,19,21] related to the d-wave symmetry of high-T_c superconductors.[23,24] Furthermore, tunneling experiments have contributed to the study of the pseudogap appearing in the high-T_c superconductors;[25] the origin of it is however still unclear.[26,27] Since STM is a local probe, it has been particularly successful in exposing spatial modulations of physical properties. Mapping of the superconducting gap has revealed spatial gap inhomogeneities on the nanometer scale.[28] In addition, periodic spatial modulations of the low-energy density of states have been observed as well.[29]

Regarding the versatility of the applied techniques it is surprising that no

conclusive evidence has been found concerning the pairing interaction in high-T_c superconductors. Some reports can be found. STM tunnel spectra measured on $Bi_2Sr_2CaCu_2O_{8+\delta}$ (BSCCO) were analyzed by Zasadzinski *et al.*[31] within the Eliashberg framework and a rather featureless spectrum for $\alpha^2(\omega)F(\omega)$ was obtained, consisting of a single peak at 36.5 meV. Although the energy of the peak matches that of a resonant spin excitation in this material, it was argued that it could equally well be a phonon.[32] Lee *et al.*[33] performed a similar analysis on BSCCO as well and found a mode around 50 meV, which showed a $^{16}O/^{18}O$ isotope substitution effect indicating that it corresponds to a lattice vibrational mode. In contrast to these results, Shim *et al.*[34] obtained a very rich spectrum from $La_{1.84}Sr_{0.16}CuO_4$ grain boundary junctions, which resembles Raman spectra obtained in this material, thus linking the relevant bosonic mode to phonons. For the copper-free superconducting oxide $Ba_{1-x}K_xBiO_3$ and the electron-doped compound $Nd_{2-x}Ce_xCuO_{4-y}$ similar observations were made,[35] although for the former the resemblance of $\alpha^2(\omega)F(\omega)$ to the phonon density of states is better than for the latter.[36] For a recent review of tunnel spectroscopy on high-T_c superconductors, see Ref. 37.

Despite these efforts, the results described above are far from conclusive and none of them has been accepted as evidence for either phonon or spin-fluctuation mediation by the scientific community. One of the larger problems with the data is reproducibility. It turns out that it is very difficult to fabricate tunnel junctions based on high-T_c materials that satisfy a few basic diagnostics[38] for a good tunnel junction: (1) scaling of the junction resistance with the junction area, (2) weak temperature-dependence of the normal state resistance from room temperature to cryogenic temperatures, (3) resolving the well-known conventional superconductor density of states, when using a conventional superconductor as one of the electrodes, and (4) reproducibility from junction to junction and from sample to sample.

Several reasons can be pointed out for the difficulty to meet these requirements. To resolve a good tunnel spectrum, the superconducting order parameter should be homogeneous over the junction area. High-T_c materials have short superconducting coherence lengths of the order of nanometers. Furthermore, the properties of doped Mott insulators depend strongly on local doping [Fig. 1.3(a)]. Due to the relatively low carrier density of high-T_c compounds, electronic screening lengths are large compared to normal metals. Disorder is intrinsic to high-T_c materials due to the distribution of dopants and the superconducting gap is found to vary on the nanometer scale.[28] Furthermore, the local doping level might vary in the direction *perpendicular* to the junction, near the interface with the tunnel barrier. Band bending effects[22,39,40] due to work function differences can induce carrier depletion regions of the order of a nanometer and one might envisage a non-superconducting surface layer in the superconductor. Band bending effects will be further discussed in Chapter 4. Another issue that plays a role is that of redox reactions occurring at the interface, as was shown by Naito *et al.*[41] using x-ray photoemission spectroscopy. The weakness of the Cu-O bond leads to oxygen deficiencies when the

high-T_c material is brought into contact with a barrier material. The resultant tunnel junction shows no signature of superconductivity. Interestingly enough, in an *ex situ* fabricated junction, for which the high-T_c superconductor had been exposed to air before deposition of the barrier, the superconducting gap was resolved. As Naito *et al.* explain, the uptake of oxygen during the exposure to air, balances the loss of oxygen due to redox reactions. Note that the top electrodes in Naito's work are grown at room temperature.

The question rises if redox reactions can be as detrimental as well in epitaxial heterostructures, which are grown at high temperatures and *in situ*. In single high-T_c thin films, the annealing procedure is of extreme importance for obtaining a proper oxygen stoichiometry in the film. Through diffusion of oxygen during the annealing process, an oxygen deficiency near the barrier can perhaps be prevented. Little is known about the spectroscopic properties of epitaxially grown tunnel structures.[42,43] Therefore, we will study in this chapter the properties of all *in situ* epitaxially grown tunnel junctions based on high-T_c superconductors using oxide barriers and either oxide or noble metal top electrodes.

3.2 Tunnel junction fabrication

3.2.1 Trilayer growth

Chemically treated, single-terminated[44] $SrTiO_3$ (001) (STO) substrates were used for sample fabrication. We used pulsed laser deposition (PLD) in combination with reflective high-energy electron diffraction (RHEED) for controlled growth of heterostructures. An overview of the different structures that have been fabricated can be found in Table 3.1. All structures are based on $La_{2-x}Sr_xCuO_4$ (LSCO), which is in most cases optimally doped ($x = 0.15$), but we also used overdoped LSCO ($x = 0.25$). For the growth of LSCO we used the settings as described in Chapter 2. The thickness of the LSCO electrodes was 30–38 unit cells (u.c.), i.e., 40–50 nm. Figure 3.2 shows the RHEED oscillations during the growth, which in this particular case were visible until the end of the deposition. The deposition was ended on an intensity maximum in order to achieve a minimal roughness. The diffraction pattern of the bare substrate and of the LSCO film are shown as well. Although the latter contains streaks, it indicates an essentially two-dimensional surface.

We have used various barrier materials, which can be divided into three kinds: (1) *in situ* grown epitaxial STO, $LaAlO_3$ (LAO) and the undoped parent compound of LSCO, La_2CuO_4 (LCO), (2) *in situ* low-temperature grown non-epitaxial STO and (3) *ex situ* grown TiO_2. For the epitaxial barriers, the deposition pressure and temperature were unchanged between the LSCO and barrier growth. The epitaxial growth was confirmed by RHEED. Figure 3.3 shows the RHEED oscillations and diffraction patterns before and after growth of STO and LAO. It was found that when the RHEED intensity was measured in the center of the

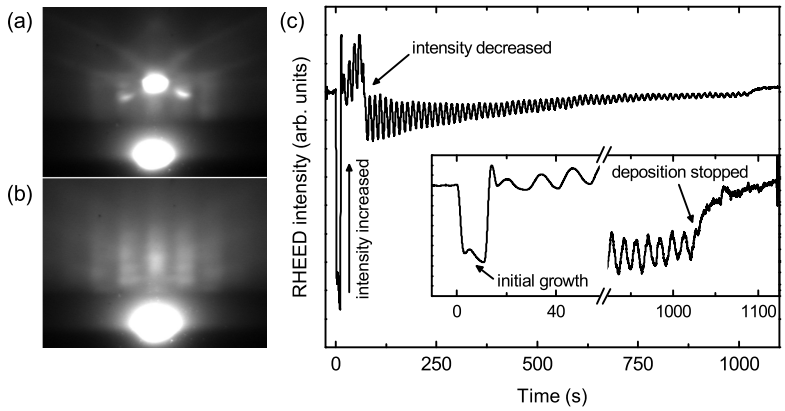

Figure 3.2: (a) RHEED pattern before and after (b) LSCO deposition. (c) RHEED oscillations during the growth. The initial behavior is typical for LSCO growth. Shortly after the start of the deposition, the RHEED intensity is increased manually and somewhat later slightly decreased. Oscillations are visible until the end of the deposition. The number of oscillations corresponds to 38 unit cells of LSCO. The deposition is stopped at a maximum.

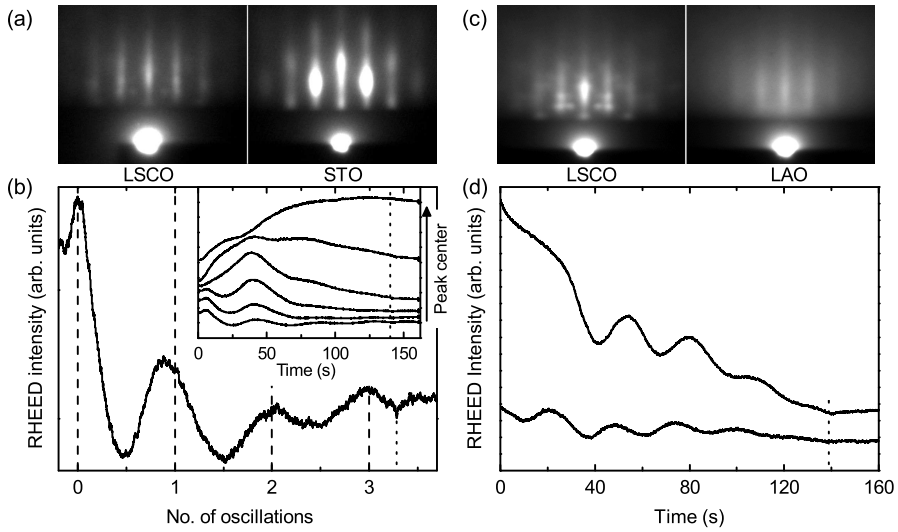

Figure 3.3: (a) RHEED pattern before and after STO deposition on top of LSCO. (b) RHEED oscillations are clearly visible when the intensity is measured out of the center of the main diffraction spot. The inset shows the intensity variation when measured closer to the center of the main diffraction spot. The dotted line denotes the end of the deposition. (c) RHEED pattern before and after LAO deposition on top of LSCO. (b) RHEED oscillations are clearly visible. The intensity is measured at two points in the main spot.

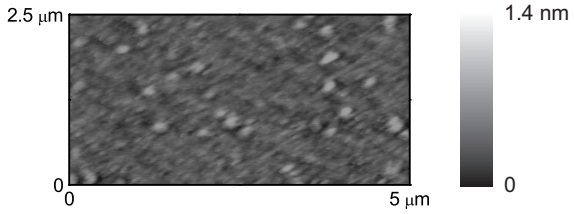

Figure 3.4: AFM image of a 40 nm LSCO film, exposed to ozone during the annealing. The rms surface roughness is 0.2 nm over the full area of the image. Scattered over the surface 1 nm peaks can be found.

main diffraction peak [the upper curve in the inset of Fig. 3.3(b)], the oscillations are disguised by the background intensity variation, which shows nonmonotonic behavior as well. When the intensity is measured out of the center of the main peak, the influence of the background is strongly diminished and the oscillations are clearly resolved. The non-epitaxial barriers are deposited at room temperature, the STO barrier *in situ* by PLD, the TiO_2 barrier by sputtering in an Ar/O_2 gas mixture.

The top electrode in almost all cases was Au, either applied by PLD or by sputtering. The PLD Au was deposited using a laser fluence of 3.5 $J\,cm^{-2}$ at 100 °C in an 0.22 mbar Ar environment. The sputtering was always performed at room temperature. In a few occasions, we used non-superconducting LSCO with doping $x = 0.05$ as the top electrode.

Some of the structures have been annealed in ozone. For that purpose, an Azcozon VMUS-4 ozone generator was used at 8 % of its maximum output using an oxygen flow of 100 $ml\,min^{-1}$ for 15 minutes after the LSCO film growth. After the barrier deposition, ozone was provided during the annealing using the same setting. The ozone was found not to roughen the LSCO film too much. We have exposed a 40 nm LSCO film to the ozone treatment and measured its roughness by atomic force microscopy (AFM). The AFM image is shown in Fig. 3.4. The root mean square (rms) roughness over the $2.5 \times 5\ \mu m^2$ area was 0.2 nm. However, scattered over the surface we found peaks of 1 nm high.

3.2.2 Structuring and contacting

The stucture used for the definition of the tunnel junction was kept as simple as possible in order to have a minimal influence of the structuring process. The junction design was initially developed for use with a cryogenic probe station, containing four probes, which can independently be placed on contact pads as small as $50 \times 50\ \mu m^2$. The geometry of the structure is shown in Fig. 3.5(a). First, a square is defined by etching through the full trilayer. Then, two concentric square slits are etched, which extent into the LSCO bottom electrode. The slits are only 5 μm wide, since etching into LSCO sometimes makes it non-superconducting

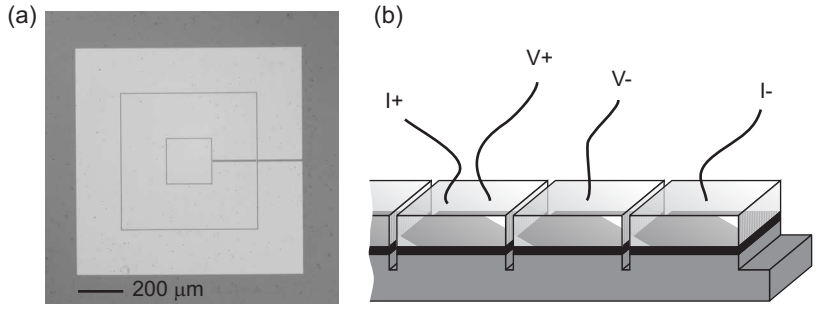

Figure 3.5: (a) Photograph of the junction viewed from the top. (b) Schematical drawing of the junction cross-section. On the left, a current and voltage contact are put on the top electrode. The voltage contact on the right (V−) probes the potential of the bottom electrode.

and we want to prevent voltage buildup over the electrodes as much as possible. Figure 3.5(b) shows a cross-section of the resulting structure. The outer shapes are interrupted at one spot by a trench, which was already defined in the first step, to prevent the formation of superconducting closed loops, which could possibly trap flux. The structure comes in two sizes on the sample, the inner square being either 200×200 or 100×100 μm^2. This inner square is the junction area. We can pass a current through the junction by placing one current contact on top of the inner square and one on top of the outer electrode. The current thus passes the barrier twice. A voltage probe on top of the inner square measures the voltage of the top electrode and another voltage on the electrode that is around it measures the voltage of the bottom electrode (provided that the area underneath the slid remains superconducting). Some junctions were fabricated using a ramp-type geometry (see Chapter 4). These will be further discussed in Sec. 3.3.6.

We initially chose to use flexible probes in the probe station in order not to damage the barrier, lying directly underneath the soft Au top electrode. However, the disadvantage was that the contacts were instable over time and contact resistances were high. Moreover, when cooling down the cold finger (which is mounted in a vacuum chamber) in the probe station, a thin layer of presumably ice formed on the sample, through which the probe tips were unable to reach the electrode.

To circumvent this problem, contacts were wire bonded directly on the Au. The risk of damaging the barrier is evident, and the junction that is ultimately formed by this method is uncontrollable. Therefore, we also have made contacts that were glued to the Au, presumably without damaging the junction, using conducting silver paint.

3.3 Results

In this section, the results of the tunnel experiments will be discussed. Because of the large amount of different structures that were fabricated, we will limit ourselves

Table 3.1: Overview of different fabricated structures, specifying the doping level x for the LSCO bottom electrode, the barrier material and thickness [in nm or unit cells (u.c.)], the annealing procedure ("oxygen" denotes the normal annealing procedure in oxygen, "ozone" means ozone was provided during the annealing) and the contacting method [by probe station (p.s.), wire bonding (w.b.), gluing (gl.) or photolithography (lith.)].

Sample	Doping	Barrier	Annealing	Contacts	Comment
J01-J03[a]	0.15	7 u.c. STO	oxygen	p.s.	Nonlinear IV at room temperature
J04	0.15	3 u.c. STO	oxygen	w.b.	Nonlinear IV, linear conductance, asymmetry
J05	0.15	3 u.c. STO	oxygen	w.b.	Linear conductance, gap-like feature, asymmetry
J06	0.15	3 u.c. STO	oxygen	lith.	Attempt to fabricate small lithographic junction
J07	0.15	3 u.c. STO	ozone	w.b.	Spectrum resemble tunnel spectrum
J08	0.15	3 u.c. STO	ozone	w.b.	Zero bias conductance peak caused by critical current
J09	0.15		ozone		LSCO film for AFM measurement
J10	0.15	6 u.c. STO	ozone	w.b.	Linear conductance
J11-J12	0.25	5 u.c. STO	oxygen	w.b.	Linear conductance, gap-like feature, asymmetry
J13	0.25	3 u.c. STO	oxygen	w.b./gl.	Zero bias conductance peak caused by critical current
J14	0.15	2 u.c. STO	oxygen	gl.	Zero bias conductance peak caused by critical current
J15	0.15	1 u.c. STO	oxygen	gl.	Linear conductance
J16	0.15	1 u.c. LCO	oxygen	gl.	Linear IV, no measurable junction resistance
J17	0.15	1 nm TiO_2	oxygen	lith.	*ab* Junction without interlayer
J18	0.15	1 nm TiO_2	oxygen	lith.	Linear conductance, gap-like feature, asymmetry
J19	0.15	1.7 nm STO[b]	oxygen	lith.	Linear conductance, asymmetry
J20	0.15		oxygen	lith.	*ab* Junction with interlayer, highly resistive
J21	0.15	5 u.c. LAO	oxygen	lith.	Highly resistive, nonlinear IV

[a] The top electrode in this case is LSCO ($x = 0.05$)
[b] Amorphous

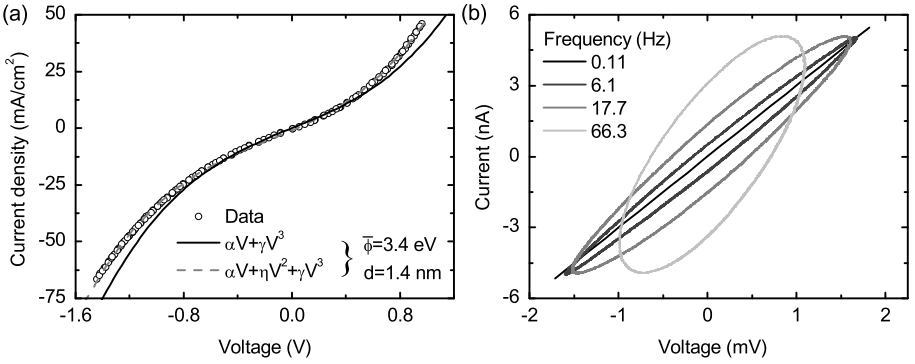

Figure 3.6: (a) Non-linear current density as a function of voltage for a LSCO(x = 0.15)/STO(7 u.c.)/LSCO(x = 0.05) junction (J03) at room temperature. The fit for α and γ from the Simmons model (see discussion in the text) corresponds to a barrier height of 3.4 eV and thickness of 1.4 nm. The best fit was obtained when a quadratic term was added, without changing α and γ. (b) Frequency dependence of a LSCO(x = 0.15)/STO(3 u.c.)/Au junction (J04) at 4.2 K.

to the key findings.

3.3.1 Barrier characterization

LSCO(x = 0.15)/STO(7 u.c.)/LSCO(x = 0.05) junctions (J01–J03) were characterized in the probe station at room temperature. These junctions show nonlinear current-voltage (IV) characteristics. The curves can be fitted reasonably well by a polynomial of the form

$$J(V) = \alpha V + \gamma V^3 \,, \tag{3.1}$$

although there is some asymmetry leading to an additional quadratic component. It has been shown by Simmons that for a metal/insulator/metal junction for low voltages the current density J takes the form of Eq. 3.1 and the parameters α and γ can be expressed as [45,46]

$$\begin{aligned} \alpha &= \left(\frac{e}{h}\right)^2 \frac{\sqrt{2m_e\bar{\phi}}}{d} \exp\left(-\beta\sqrt{\bar{\phi}}\right), \\ \frac{\gamma}{\alpha} &= \frac{(\beta e)^2}{96\bar{\phi}} - \frac{\beta e^2}{32\sqrt{\bar{\phi}}}, \end{aligned} \tag{3.2}$$

in which h, e and m_e are the Planck constant, the charge and the mass of the electron and $\bar{\phi}$ the barrier height, averaged over the barrier thickness, d. The parameter β is given by $\beta = 4\pi\sqrt{2m_e}d/h$.

Fitting to the IV-curve yields a barrier height $\bar{\phi}$ = 3.4 eV and thickness of d = 1.4 nm; see Fig. 3.6(a). The best fit was obtained when a quadratic component was added, without changing α and γ. The barrier height is slightly larger than the

STO bandgap of 3.2 eV and the derived thickness corresponds to roughly half of the actual 7 unit cell thick barrier. We characterized a LSCO($x = 0.15$)/STO/Au junction (J04) with a 3 u.c. cell barrier, which was contacted by wire bonding, at room temperature as well. For one junction we find values for the barrier height and thickness of 3.2 eV and 1.2 nm but for another junction we find 6.2 eV and 0.9 nm. Since such a barrier height is unrealistic, we assume that an ohmic shunt resistance is present, parallel to the barrier resistance. This only affects the linear part in Eq. 3.1. By adjusting the value of the shunt resistance, we fit the barrier thickness (1.2 nm) and we find a shunt of 1.9 kΩ and a barrier height of 3.4 eV. From this room temperature analysis we conclude the following: the STO barrier in between LSCO electrodes shows insulating behavior with a barrier height that is close to the value of the bandgap. However, for thicker barriers, the effective barrier thickness can be reduced compared to the thickness of the deposited STO layer. Furthermore, shunt resistances can be present especially when the contacts are prepared by wire bonding on top of the structure.

At low temperatures (4.2 K), the IV-curve of J04 shows a pronounced dependence on the frequency that was used to sweep the voltage [Fig. 3.6(b)]. When the voltage was swept very slowly, the curve was linear in the low-voltage range (between −2 and 2 mV), but when the frequency exceeded 1 Hz, the curve became ellipse-shaped. This behavior is of course likely related to the capacitance that is provided by the structure. The simplest way to describe the structure is by a parallel resistance (R) and capacitor (C). It can then be shown that the relative amplitude of and the phase shift φ_{RC} between the sinusoidal voltage and current (of frequency $\omega/2\pi$) are given by $V_{\max}/I_{\max} = R/\sqrt{1+(\omega RC)^2}$ and $\tan\varphi_{\mathrm{RC}} = \omega RC$. We determined $V_{\max}/I_{\max}$ and φ_{RC} at a frequency $\omega/2\pi = 66.2$ Hz and solved the equations, finding a resistance of 300 kΩ and a capacitance of 7.5 nF. These parameters correspond to a time constant $\tau_{\mathrm{RC}} \approx 2$ ms and a cut-off frequency of 71 Hz. The resistance matched the value that was measured directly in the low-frequency limit. By using the well-known expression for a parallel plate capacitor of area A, $C = A\epsilon_{\mathrm{r}}\epsilon_0/d$, we can estimate the relative dielectric constant of the STO layer. For the barrier thickness we take 1.2 nm, corresponding to the thickness of the deposited layer and consistent with Eq. 3.1. We then find a relative dielectric constant $\epsilon_{\mathrm{r}} = 35$ at 4.2 K. Although this is quite a large value, it is not unrealistic, since the low-temperature dielectric constant can exceed even the value of 10,000 in single crystals[47] but is known to be suppressed in thin films.[48] Because of the large time constant for our system, lock-in techniques were only applied at sufficiently low frequencies. When applying DC-techniques, we programmed a waiting time of at least a few time constants between the application of the voltage and the measurement of the current.

3.3.2 Critical current effects

For one of the ozone annealed LSCO/STO/AU junctions with a 3 u.c. STO barrier (J07), we have observed a conductance spectrum at 2 K [Fig. 3.7(a)], which

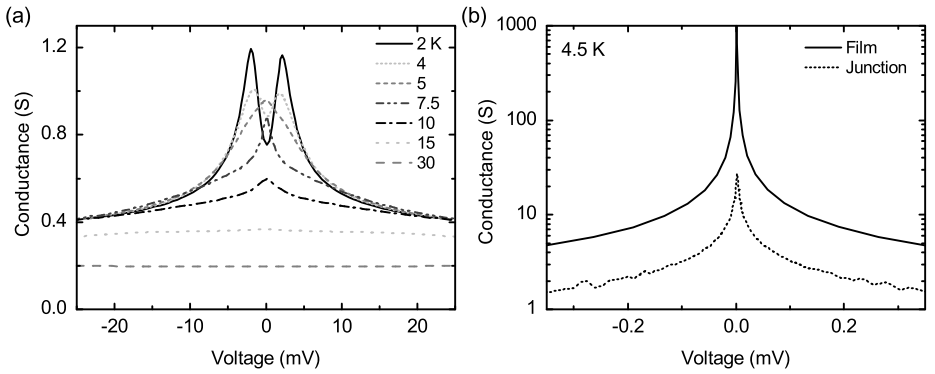

Figure 3.7: (a) Conductance spectrum for an ozone annealed LSCO/STO/Au junction with a 3 u.c. barrier contacted by wire bonding. As discussed in the text, the drop in conductance above 2 mV observed at 2 K is caused by the reaching of J_c. (b) Effects of J_c observed in an oxygen annealed LSCO/STO/Au junction with a 2 u.c. barrier and contacted by gluing. The solid line represents a measurement taken in four-point configuration.

strongly resembles the expected spectrum for a d-wave superconductor metal junction with a barrier of a small but non-zero transparency, a gap of 2 meV and tunneling along the c direction.[24,49] However, the temperature evolution of the spectrum is far from expected: a strong thermal smearing would be necessary to reduce the two peaks observed at 2 K to a single peak observed at 7.5 K. Yet, the sharpness of the peak at 7.5 K is incompatible with strong thermal smearing. Moreover, the total density of states seems not conserved: the area under the conductance curves decreases with temperature. Attempts to fit the temperature dependence of the data were therefore unsuccessful. On top of all that, a 2 meV gap is rather small compared to the expected value of about 10 meV for LSCO.[18]

If we assume for the moment that the 2 K curve is a tunnel spectrum of a superconductor, we find from our fitting attempts and from comparison to available data in the literature[20] that the dimensionless barrier parameter Z should be about 0.5.[50] It can be shown[20] that the normal state conductance $G_N = (e^2/h)(1 + Z^2)^{-1}(k_F R_J)^2$, with k_F the Fermi wave vector and R_J the junction radius. For a normal-state conductance of 0.4 S, we calculate $k_F R_J \approx 100$, from which we estimate a junction size of 10–100 nm. This is much smaller than the actual junction size. This could be the case if the junction is formed by one or a few pinholes through the barrier. However, the local current density would then be about 10^8 A cm^{-2} and exceed the critical current density J_c of the superconductor of about 10^6 A cm^{-2} (J_c is expected to be even lower in the c direction[51]).

The peaks observed at ± 2 mV in Fig. 3.7(a) thus cannot be the coherence peaks of the superconductor and we attribute the conductance drop above 2 mV to the reaching of J_c, whereas the linearly increasing conductance below 2 mV is part of the actual tunnel spectrum (which will be discussed in further detail

in Sec. 3.3.3). If the current would be homogeneously distributed over the entire junction area, the current density at 2 mV would be 8 A cm^{-2}, which implies a rather low J_c. However, this particular junction was contacted by wire bonding and it was already anticipated that the actual junction size could be smaller than the full size of the junction.

In Fig. 3.7(b) we have plotted the conductance as a function of voltage for an oxygen annealed LSCO/STO/Au junction with a 2 u.c. barrier (J14), which was contacted by gluing instead of wire bonding. The junction shows a high and narrow conductance peak around zero bias; note the logarithmic scale of the graph. The dashed line is the measurement of the junction, whereas the solid line is measured in a standard four-point configuration. In the latter configuration, the conductance peak can only be due to the reaching of J_c in the film. The similarity between the two measurements indicates a similar origin for the junction. In this case, J_c is reached for almost zero voltage, in contrast to the ozone annealed, wire bonded junction with a 3 u.c. barrier. We attribute this dissimilarity to the difference in barrier thickness.

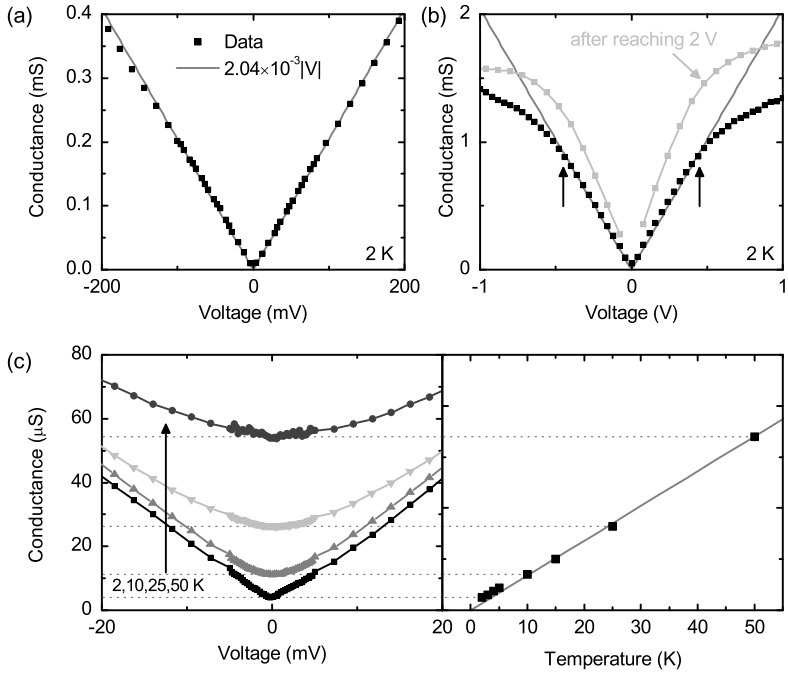

Figure 3.8: (a) Linear conductance observed for a LSCO/STO/Au junction with a 3 u.c. STO barrier observed at 2 K. The solid line is a fit. (b) The linear conductance is observed up to 0.45 V. After reaching 2 V, the conductance of the junction had permanently increased, while the behavior for low voltages remained linear. (c) Zero bias conductance as a function of temperature. The line on the right is a linear fit.

3.3.3 Linear conductance background

Some of our junctions show a pronounced linear background in the conductance spectrum. In Fig. 3.8(a), the conductance spectrum for a LSCO/STO(3 u.c)/Au junction on J05 is shown, which is one of the most striking examples. This particular junction showed a rather featureless spectrum, so the background itself is dominantly present. The solid line in the graph is a plot of the function $G = 2.04 \times 10^{-3}|V|$, which fits the data well over a wide voltage range. In Fig. 3.8(b), we show that the conductance remains linear up to $\approx \pm 0.45$ V, as indicated by arrows. It was found that after applying voltages above this level, permanent changes to the conductance spectrum were induced: The conductance became larger for low-level voltages, but remained linear in this regime. The permanent changes likely indicate that the application of high voltages damages the junction and the deviation from linear conductance above 0.45 V is probably related to this. Reasons for changing junction characteristics induced by high voltages could be electromigration[52] of oxygen in the junction or excessive heating. As can be seen in Fig. 3.8(c), the conductance does not reach zero for zero bias voltage, but displays a temperature dependence which is approximately linear.

Linear conductance spectra for tunnel junctions have repeatedly been observed, in particular for cuprate/normal metal tunnel junctions,[53–55] but also for non-cuprate junctions.[53,56,57] Various explanations for linear behavior have been suggested. It was proposed by Anderson[58] that the linear conductance is an intrinsic property of high-T_c junctions and can be expected from the resonating-valence-bond theory.[58] The spectrum should then be asymmetric,[59] which will be discussed in more detail in Sec. 3.3.4. Giaever and Zeller[60] showed experimentally and theoretically that the inclusion of metallic nanoparticles in the barrier can induce linear conductance around zero bias voltage.[46] This classical effect arises from the threshold voltage needed to transfer an electron to such a metallic particle, as a result of the Coulomb charging energy. A random distribution of these threshold voltages for a large amount of metallic particles causes linear conductance as a function of applied voltage. It was shown that for such a system the zero-bias-voltage conductance linearly depends on temperature,[60] which matches with our observation in Fig. 3.8(c). However, the linear conductance should saturate for voltages that are large compared to the Coulomb potentials involved in charging the metallic particles, which typically is about 10 mV for 8 nm particles.[60] The energy to charge a metallic sphere of radius R with a single electron is given by $E = e^2/8\pi\epsilon_0 R$. For metallic particles embedded in a dielectric medium this energy is decreased. If we use the saturation voltage of 0.45 V that was found in Fig. 3.8(b), we estimate that the particles in our barrier would have to be about 0.2 nm in size. That would be the size of a single atom, and although point defects might be present in our junction, these likely behave in a different way than the metallic particles described above. Hopping processes via a number of localized states generally do not give rise to linear conductance spectra and zero bias conductance linear with temperature,[61,62] unless a large number of localized states is

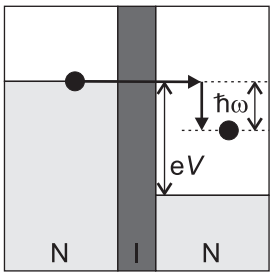

Figure 3.9: Schematical drawing of the principle of inelastic tunneling in a normal metal/ insulator/normal metal junction (N/I/N). When a bias voltage V is applied, tunneling takes place from filled electron states (grey) in the normal metal on the left to empty states (white) in the normal metal on the right, while loosing an amount $\hbar\omega$ of energy.

involved, which is not expected at low temperature.[61]

An alternative explanation for the linear background conduction is provided by Kirtley and Scalapino and is based on inelastic tunneling.[53,63,64] In this case, electrons traverse the barrier while loosing energy $\hbar\omega$. For this to happen an inelastic scattering mode must be present and the distribution of inelastic scattering modes can be described by the spectral function $F_{\mathrm{inel}}(\omega)$. If we now assume a broad and flat distribution of inelastic scattering modes $F_{\mathrm{inel}}(\omega) = \text{constant} = F_{\mathrm{inel}}$, we obtain that electrons can tunnel through the junction under applied bias voltage V to all empty electron states with equal probability; see Fig. 3.9. It is easy to

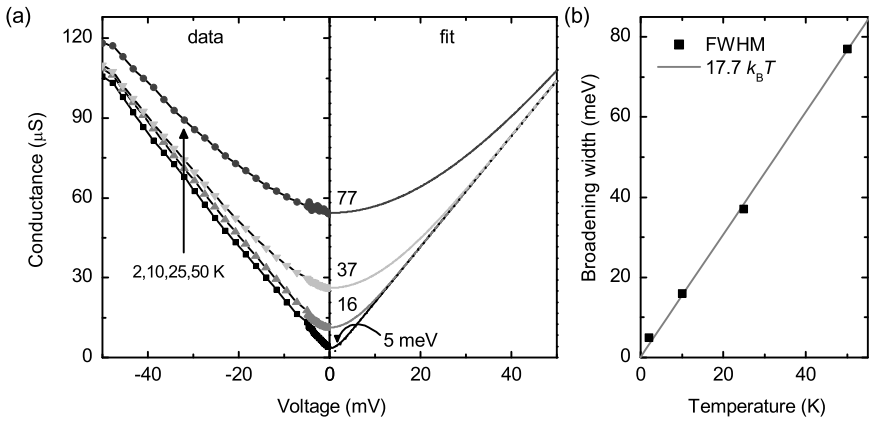

Figure 3.10: (a) The data of Fig. 3.9 can be fitted reasonably well by broadening the function $G = 2.04 \times 10^{-3}|V|$. The broadening has been performed by convolution with a gaussian with FWHM as indicated in the graph. (b) The broadening width linearly depends on temperature, following 17.7 $k_{\mathrm{B}}T$.

see that now $\mathrm{d}I \propto V\mathrm{d}V$, or more specifically[53]

$$\frac{\mathrm{d}I}{\mathrm{d}V} \propto \int_0^{eV} F_{\mathrm{inel}}\mathrm{d}\omega\,, \tag{3.3}$$

i.e., the conductance will be linear with voltage. Kirtley and Scalapino have elaborated this idea with a specific model for such a broad and flat spectral function based upon spin fluctuations. They predict a linear temperature dependence for the zero bias conductance, again in agreement with our observation. Furthermore, they predict a thermal smearing of the conductance of about 6 $k_{\mathrm{B}}T$. In Fig. 3.10(a) we have taken the function $G = 2.04 \times 10^{-3}|V|$ and convoluted it with a gaussian function with various widths [we define the width by the full width at half maximum (FWHM)], such to fit the zero bias conductance. It can be seen that the measurements at elevated temperatures indeed can be obtained from thermal smearing of the zero temperature limit. In Fig. 3.9(b) we have plotted the broadening widths, found from the fitting as a function of temperature. It follows a linear temperature dependence and we find a smearing of about 18 $k_{\mathrm{B}}T$. Although this is significantly larger than the predicted value of 6 $k_{\mathrm{B}}T$, the inelastic tunneling model is in reasonable agreement with our observations. Thermal smearing due to the temperature dependence of the Fermi distribution function, which would arise if the linear conductance would reflect a density-of-states effect, would yield a broadening width of 3.5 $k_{\mathrm{B}}T$.

3.3.4 Asymmetric conductance spectra

For many junctions, we have observed asymmetric conductance spectra, such as the one shown in Fig. 3.11 measured on J05 [LSCO ($x = 0.15$), STO (3 u.c.), Au]. The conductance for this junction varies linearly with voltage, although for reverse bias a small quadratic component is present. The presence of both linear conductance and asymmetry implies that these two phenomena arise from a single mechanism or at least two closely related mechanisms. The voltage in Fig. 3.11 is defined as the voltage of the Au electrode with respect to the LSCO. Observations of tunneling asymmetry have been reported from the early days of tunneling experiments with high-T_c superconductors.[10–12,57,65–68] As mentioned in Sec. 3.3.3, linearity and asymmetry of tunnel spectra follow from the resonating-valence-bond theory.[58,59] However, this theory predicts constant conductance for electrons moving into the superconductor, which in Fig. 3.11 is clearly not the case. A particular intuitive idea is based on the notion that the high-T_c superconductors are doped Mott insulators in which local Coulomb repulsion induces insulating behavior of a half-filled electron band. Injecting (tunneling) electrons into such a doped Mott insulator is proposed to lead to the "jamming" of electrons, whereas extracting electrons creates holes, which can freely move the material.[69] In many cases, asymmetric tunnel spectra indeed show larger conductance when extracting electrons from the superconductor.[68] In our junction however, the conductance is higher when injecting electrons into LSCO. Reports of asymmetric conductance with the

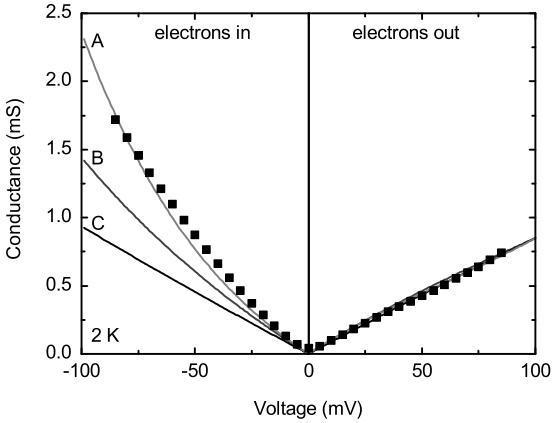

Figure 3.11: Asymmetric conductance spectra with linear conductance. The horizontal axis denotes the voltage of the Au electrode with respect to the LSCO. This implies that for positive voltage electrons will move out of the LSCO into the Au. The solid lines denote fits as described in the text (Eq. 3.4) using the following parameters: (A) $\bar{\phi} = 1.2$ eV, $d = 4.8$ nm (yielding $E_0 = 44$ meV), (B) $\bar{\phi} = 2.0$ eV, $d = 3.0$ nm ($E_0 = 92$ meV), (C) $\bar{\phi} = 3.2$ eV, $d = 1.2$ nm ($E_0 = 290$ meV). In all cases $E_\mathrm{F} = 0.5$ eV and $\eta \downarrow 0$.

highest conductance when injecting electrons can be found in the literature as well.[67,70] Thus, the mechanism leading to asymmetry should explain both types of asymmetry. One of the mechanisms that satisfies this condition is based on inelastic tunneling, just like the proposed mechanism for linear conductance spectra of Kirtley and Scalapino.[53] Grajcar *et al.*[70] have extended this model by taking into account the position in the barrier where inelastic scattering takes place. This is described by the dimensionless parameter η, where $\eta = 0$ means that inelastic scattering takes place at the normal-metal side of the barrier and $\eta = 1$ means scattering at the side of the superconductor. Grajcar *et al.* derive for the tunnel conductance

$$\begin{aligned} G \propto & \frac{\mp E_0^2(2\eta-1)}{2\eta^2}\exp\left(\frac{-eV}{2E_0}\right)\left[\exp\left(\frac{\pm\eta|eV|}{E_0}\right)-1\right] \mp \frac{E_0}{2\eta}\exp\left(\frac{-eV}{2E_0}\right)eV \\ & \mp E_0^2\exp\left(\frac{E_\mathrm{F}}{E_0}\right)\left\{\left[\frac{1}{2\eta}-\left(\frac{1}{2\eta}+\frac{1}{2(\eta-1)}\right)\exp\left(\frac{\pm\eta|eV|}{E_0}\right)\right]\exp\left(\frac{-eV}{2E_0}\right)\right. \\ & \left. + \frac{1}{2(\eta-1)}\exp\left(\frac{eV}{2E_0}\right)\right\}. \end{aligned} \tag{3.4}$$

The parameter E_0 is given by $E_0 = \bar{\phi}/\kappa_0 d$ with $\bar{\phi}$ the barrier height, d the thickness and $\kappa_0 = \sqrt{2m_\mathrm{e}\bar{\phi}/\hbar^2}$. In Fig. 3.11 we have plotted this function for various sets of parameters. Plot A fits the data reasonably well. For this curve we used $\bar{\phi} = 1.2$ eV, $d = 4.8$ nm (yielding $E_0 = 44$ meV), $E_\mathrm{F} = 0.5$ eV and $\eta \downarrow 0$. The

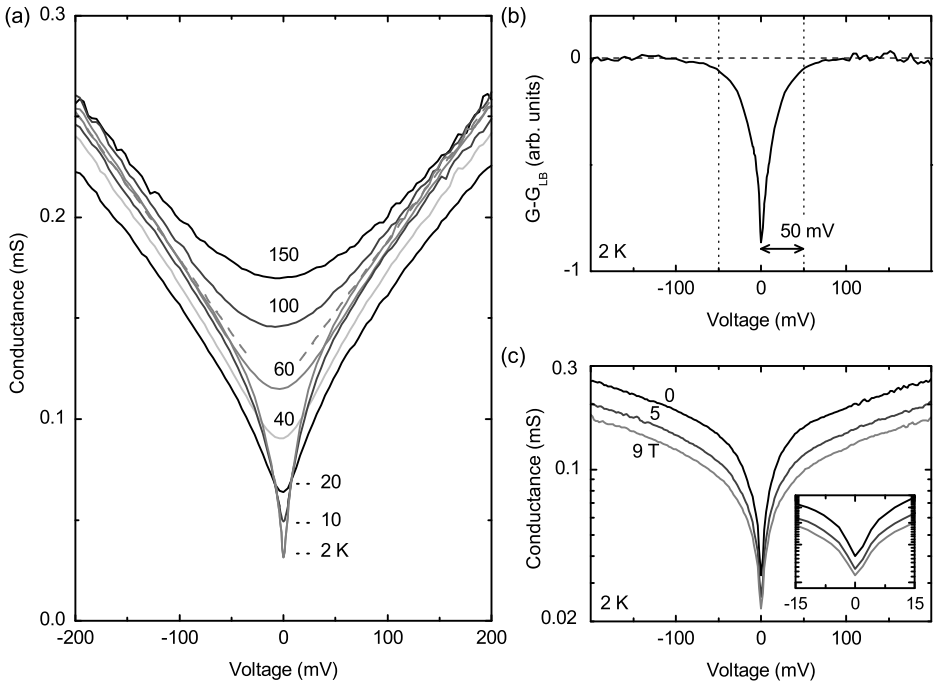

Figure 3.12: (a) The conductance spectrum for a LSCO/STO/Au junction with a 3 u.c. STO barrier shows a gap-like feature for temperatures below 60 K. (b) When the linear background is subtracted from the 2 K curve in (a), we obtain a dip. The area of the dip lies for 95 % between ±50 mV. (c) Magnetic field dependence of the conductance spectrum at 2 K. Note the logarithmic scale.

results are only weakly dependent on E_F in the range 0.1–0.5 eV, which covers the Fermi energy of LSCO (Ref. 71). For negative bias the curve reproduces the slight nonlinearity of the conductance, but also overestimates it. An attractive feature of the model is that the asymmetry depends on the specific values of the parameters. Curve C, produced for $\bar{\phi} = 3.2$ eV and $d = 1.2$ nm (the other parameters unchanged), which would be the nomimal values for this junction, hardly shows asymmetry and strongly resembles the symmetric curve observed in Fig. 3.8(a). For an appropriate set of parameters and specifically when choosing $\eta = 1$, the asymmetry will be reversed, i.e., the highest conductance is expected for positive bias voltage.

3.3.5 Gap-like feature

For a few junctions, we have observed the appearance of a gap-like feature in the conductance spectrum at low temperatures. In Fig. 3.12(a) we show an example measured on a LSCO/STO(3 u.c.)/Au sample (J05). The gap-like feature is visible

for temperatures of 60 K and below. It is possible that at higher temperatures, the gap is hidden by thermal smearing. To estimate the width of the gap-like feature, we have subtracted the linear background for the 2 K conductance spectrum in Fig. 3.12(b). The gap is visible as a sharp dip in the spectrum, but without coherence peaks that would be characteristic of a superconducting gap. The FWHM of the dip is 20 mV and the base of the dip spans about 100 mV (95 % of the integrated area of the dip can be found between −50 and 50 mV). Fig. 3.12(c) shows that when a magnetic field is applied, the conductance is reduced for all bias voltages in the range of −200–200 mV, with a voltage independent scaling factor (note the logarithmic scale of the figure). This implies that the observed gap feature is essentially independent of magnetic field.

It is appealing to ascribe the observed gap-like feature to the pseudogap. The pseudogap opens up in the electronic excitation spectrum below a temperature generally denoted by T^*.[18,25] As mentioned in Sec. 1.2, consensus about the nature of the pseudogap is lacking. One possibility is that it originates from pair fluctuations in the absence of a coherent condensate, with the latter being formed at T_c. Alternatively, the pseudogap might reflect some kind of ordering, such as (fluctuating) magnetic ordering, which could be unrelated or even in competition with superconductivity.

Angle-resolved photoemission[72] and NMR (Ref. 73) indicate a *d*-wave symmetry of the pseudogap. In *c*-axis STM experiments the pseudogap is routinely observed.[18] Considering the finite tunneling cone for planar tunnel junctions,[19,46] it is reasonable to expect the pseudogap to show up for our planar geometry as well.

Values reported for the pseudogap energy for LSCO vary from 30–100 meV as determined by angle-resolved photoemission spectroscopy,[74–77] while a value of 43 meV was reported in an optical conductivity study.[25] The pseudogap was reported to exist up to 200 K,[76] but gradually fills with temperature, so that it is understandable that we do not observe a clear gap in the spectra in Fig. 3.12(a) measured above 60 K. Little is known about the field dependence of the pseudogap in the normal state. However, scanning tunneling spectroscopy at 6 T on vortex cores in $Bi_2Sr_2CaCu_2O_{8+\delta}$ reveals a pseudogap inside the vortex core, which by thermal smearing evolves into the pseudogap measured above T_c. The field independence of the the pseudogap in moderate fields up to 6 T seems therefore not unlikely. (We note that the magnitude of the pseudogap in the normal state is largely temperature independent.[18,26]) The gap-like feature observed in Fig. 3.12 might thus well be a signature of the pseudogap.

The possible observation of the pseudogap, but absence of a superconducting gap can be explained by assuming that the charge carrier density in an interfacial layer adjacent to the tunnel barrier would be reduced from the nominal value for $x = 0.15$. If the hole density is sufficiently reduced, we might locally have $x < 0.05$, for which according to the phase diagram in Fig. 1.3 we can expect a pseudogap state, but not a superconducting state. The envisaged hole suppression might be brought about by band bending or oxygen deficiency near the barrier.

In Chapter 4, we will discuss these kind of effects in more detail.

We would like to make a final remark in this section about the observed bias voltage independence of conductance suppression by magnetic field in Fig. 3.12(c). Since the entire linear background is suppressed by a constant factor, the suppression by magnetic field might well originate from the magnetic field dependence of the inelastic tunneling as described in Sec. 3.3.3. If the inelastic scattering indeed stems from spin fluctuations, a field dependence of the spectral weight F_{inel} might be readily expected due to the magnetic nature of spin fluctuations. More specifically, if $F_{\mathrm{inel}}(H) = \alpha(H)F_{\mathrm{inel}}(0)$ with $\alpha(H)$ a field-dependent scaling factor we obtain by using Eq. 3.3 that $G(H,V) = \alpha(H)G(0,V)$, which is what we experimentally observe.

3.3.6 Behavior of other junction types

In this section we will briefly comment on the results obtained for other junction types that were fabricated. In pursuit of the "ideal" LSCO tunnel junction[42] we fabricated a LSCO($x = 0.15$)/LCO/Au junction (J16), with a barrier of a monolayer (1.3 nm) of undoped La_2CuO_4, which is the insulating parent compound of LSCO. The junction resistance was unmeasurably small and it can be questioned whether a sufficiently sharp carrier density profile can be achieved to render the LCO insulating. In one occasion (J21) we tried $LaAlO_3$ for the tunnel barrier. The 5 u.c. barrier had a large resistance of several MΩ, as can be expected for a barrier of this thickness. Due to this large resistance, we could not accurately measure the conductance spectrum.

Several *c*-axis and *ab*-axis junctions have been prepared using the ramp-type geometry (see Chapter 4). For such a *c*-axis junction (J06), a SiO_2 insulating layer was deposited over the ramp that was etched into an LSCO/STO/Au trilayer. After the SiO_2 deposition, the LSCO had become non-superconducting and highly resistive. A ramp-type *ab* junction was prepared by sputter depositing a TiO_2 barrier and Au top electrode on an etched ramp in a LSCO/STO bilayer. Although the LSCO itself was unaffected, the junction was completely insulating and could withstand several V. In an attempt to reduce the resistance of LSCO *ab* junctions, we applied the interlayer[78] concept. After etching the ramp, a thin LSCO interlayer was deposited in order to improve the properties of the LSCO at the ramp. Subsequently, a Au top electrode was deposited. The resulting junction was however still highly resistive, despite the use of an interlayer.

We have taken the insulating properties of etched ramps in LSCO to our advantage by growing a TiO_2 barrier and Au top electrode on a ramp etched into a bare LSCO film (with a thin Au capping layer, later removed by sputter etching). This simple method yields a small-area lithographic *c*-axis junction (J18). The junction shows all the features described in Secs. 3.3.3, 3.3.4 and 3.3.5, including a remarkably linear conductance background, asymmetry and a gap-like feature. The same approach was also applied to a LSCO/STO/Au junction with a 1.7 nm amorphous STO barrier (J19), also yielding a junction showing a linear conduc-

tance background and asymmetry. Because of the minimal number of fabrication steps needed for this method, while still yielding well-defined small-area junctions, it is worth to continue in this direction.

3.4 Conclusion and outlook

In this chapter we have shown the results of tunnel experiments with the high-T_c superconductor LSCO. Junction were fabricated mainly all *in situ*. Planar LSCO/STO/Au junctions were characterized by a linear conductance as a function of voltage, and in many occasions an asymmetric spectrum. Sometimes a gap-like feature was observed, which might be associated with the pseudogap. Linear conductance, asymmetry and gap-like features were also seen in small-area lithographic junctions with TiO_2 and amorphous STO barriers. Since no superconducting gaps are observed, we are led to believe that the LSCO that is tunneled into, is locally in the underdoped regime.

The results are in agreement with the observation of Naito *et al.*[41] that *in situ* grown junctions show underdoped behavior. Our results show that this is even true when the barrier is fabricated at high temperature and annealed in oxygen at atmospheric pressure. One might therefore wonder whether the explanation provided by Naito *et al.*, namely the occurrence of redox reaction at the cuprate surface, is the complete picture. There might be additional origins for carrier depletion at the interface, such as for instance band bending effects. The next chapter will proceed with this issue, but focus on the YBCO/LSMO interface.

The linear conductance spectra observed in high-T_c tunnel junctions are quite interesting. The linearity is pronounced and is reproducibly observed for a wide variety of junctions [see also Fig. 4.3(b)]. The linear behavior can be understood in terms of inelastic tunneling,[53] with spin fluctuations as a possible candidate for the inelastic scatter modes. It is an intriguing thought that, while large efforts are made to find subtle signatures of phonons or other bosonic modes in the background of tunnel spectra, the background itself might actually be what is searched for.

The results in this chapter call for a step-by-step examination of the junction surface in various stages of the fabrication process. Currently, such an investigation is conducted on our samples at the Kamerlingh Onnes Laborotory of Leiden University. STM is performed on bare and Au-capped YBCO grown in a tilted fashion on STO (305) substrates (see Chapter 5) and STO (110) substrates. Fig. 3.13 shows an example of a tunnel spectrum obtained on such a sample. The spectrum shows a superconducting gap of about 17 meV and a clear zero bias conductance peak (ZBCP). The STM results might shed light on the anomalous behavior of the proximity effect in Au coated YBCO films.[79] In addition, these measurement can provide information on the YBCO/Au interface with a sensitivity for lateral variations.

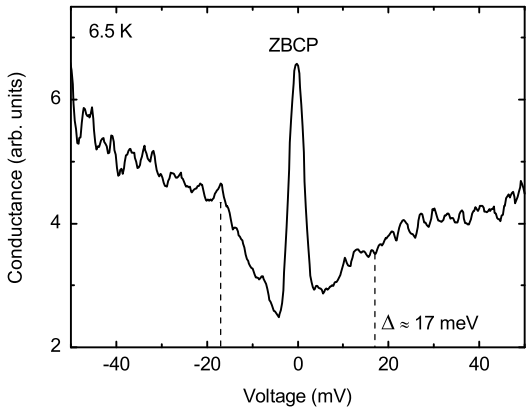

Figure 3.13: STM measurement on epitaxially tilted YBCO grown on STO (305) (see Chapter 5). The spectrum shows a gap of about 17 meV and a ZBCP. The measurement was performed by S. Kelly, F. Galli and J. Aarts at the Kamerlingh Onnes Laborotory of Leiden University.

References

[1] M. A. Biondi, A. T. Forrester, M. P. Garfunkel, and C. B. Satterthwaite, Rev. Mod. Phys. **30**, 1109 (1958).

[2] J. Bardeen, L. N. Cooper, and J. R. Schrieffer, Phys. Rev. **108**, 1175 (1957).

[3] I. Giaever, Phys. Rev. Lett. **5**, 147 (1960).

[4] I. Giaever and K. Megerle, Phys. Rev. **122**, 1101 (1961).

[5] I. Giaever, H. R. Hart, and K. Megerle, Phys. Rev. **126**, 941 (1962).

[6] G. M. Eliashberg, Zh. Ekseperim. i Teor. Fiz. **38** (1960), [translation: Soviet Phys.-JETP **11**, 696 (1960)].

[7] J. M. Rowell, P. W. Anderson, and D. E. Thomas, Phys. Rev. Lett. **10**, 334 (1963).

[8] J. R. Schrieffer, D. J. Scalapino, and J. W. Wilkins, Phys. Rev. Lett. **10**, 336 (1963).

[9] W. L. McMillan and J. M. Rowell, Phys. Rev. Lett. **14**, 108 (1965).

[10] S. Pan, K. W. Ng, A. L. de Lozanne, J. M. Tarascon, and L. H. Greene, Phys. Rev. B **35**, 7220 (1987).

[11] M. Naito, D. P. E. Smith, M. D. Kirk, B. Oh, M. R. Hahn, K. Char, D. B. Mitzi, J. Z. Sun, D. J. Webb, M. R. Beasley, et al., Phys. Rev. B **35**, 7228 (1987).

[12] J. R. Kirtley, C. C. Tsuei, S. I. Park, C. C. Chi, J. Rozen, and M. W. Shafer, Phys. Rev. B **35**, 7216 (1987).

[13] J. Lesueur, L. H. Greene, W. L. Feldmann, and A. Inam, Physica C **191**, 325 (1992).

[14] A. M. Cucolo and R. Di Leo, Phys. Rev. B **47**, 2916 (1993).

[15] L. Alff, H. Takashima, S. Kashiwaya, N. Terada, H. Ihara, Y. Tanaka, M. Koyanagi, and K. Kajimura, Phys. Rev. B **55**, 14757 (1997).

[16] M. Covington, M. Aprili, E. Paraoanu, L. Greene, F. Xu, J. Zhu, and C. Mirkin, Phys. Rev. Lett. **79**, 277 (1997).

[17] M. Aprili, E. Badica, and L. H. Greene, Phys. Rev. Lett. **83**, 4630 (1999).

[18] O. Fischer, M. Kugler, I. Maggio-Aprile, C. Berthod, and C. Renner, Rev. Mod. Phys. **79**, 353 (2007).

[19] J. Wei, N. Yeh, D. Garrigus, and M. Strasik, Phys. Rev. Lett. **81**, 2542 (1998).

[20] G. Deutscher, Rev. Mod. Phys. **77**, 109 (2005).

[21] L. Alff, A. Beck, R. Gross, A. Marx, S. Kleefisch, T. Bauch, H. Sato, M. Naito, and G. Koren, Phys. Rev. B **58**, 11197 (1998).

[22] H. Hilgenkamp and J. Mannhart, Rev. Mod. Phys. **74**, 485 (2002).

[23] Y. Tanaka and S. Kashiwaya, Phys. Rev. Lett. **74**, 3451 (1995).

[24] S. Kashiwaya and Y. Tanaka, Rep. Prog. Phys. **63**, 1641 (2000).

[25] T. Timusk and B. Statt, Rep. Prog. Phys. **62**, 61 (1999).

[26] C. Renner, B. Revaz, J.-Y. Genoud, K. Kadowaki, and O. Fischer, Phys. Rev. Lett. **80**, 149 (1998).

[27] M. C. Boyer, W. D. Wise, K. Chatterjee, M. Yi, T. Kondo, T. Takeuchi, H. Ikuta, and E. W. Hudson, Nat. Phys. **3**, 802 (2007).

[28] K. M. Lang, V. Madhavan, J. E. Hoffman, E. W. Hudson, H. Eisaki, S. Uchida, and J. C. Davis, Nature **415**, 412 (2002).

[29] J. E. Hoffman, E. W. Hudson, K. M. Lang, V. Madhavan, H. Eisaki, S. Uchida, and J. C. Davis, Science **295**, 466 (2001).

[30] Thomson-Reuters ISI Web of Knowledge (2009), Topical search on keywords: (tunnel* or junction*) and (cuprate* or (high-T* and supercond*) or YBa2Cu3O* or Bi2Sr2CaCu2O* or La2-xSrxCuO*).

[31] J. F. Zasadzinski, L. Coffey, P. Romano, and Z. Yusof, Phys. Rev. B **68**, 180504 (2003).

[32] J. F. Zasadzinski, L. Ozyuzer, L. Coffey, K. E. Gray, D. G. Hinks, and C. Kendziora, Phys. Rev. Lett. **96**, 017004 (2006).

[33] J. Lee, K. Fujita, K. McElroy, J. A. Slezak, M. Wang, Y. Aiura, H. Bando, M. Ishikado, T. Masui, J.-X. Zhu, et al., Nature **442**, 546 (2006).

[34] H. Shim, P. Chaudhari, G. Logvenov, and I. Bozovic, Phys. Rev. Lett. **101**, 247004 (2008).

[35] Q. Huang, J. F. Zasadzinski, N. Tralshawala, K. E. Gray, D. G. Hinks, J. L. Peng, and R. L. Greene, Nature **347**, 369 (1990).

[36] I. W. Sumarlin, J. W. Lynn, D. A. Neumann, J. J. Rush, C.-K. Loong, J. L. Peng, and Z. Y. Li, Phys. Rev. B **48**, 473 (1993).

[37] V. Z. Kresin and S. A. Wolf, Rev. Mod. Phys. **81**, 481 (2009).

[38] L. H. Greene, M. Aprili, M. Covington, E. Badica, D. E. Pugel, H. Aubin, Y. M. Xia, M. B. Salamon, S. Jain, and D. G. Hinks, J. Supercond. **13**, 703 (2000).

[39] J. Mannhart, A. Kleinsasser, J. Ströbel, and A. Baratoff, Physica C **216**, 401 (1993).

[40] J. Mannhart and H. Hilgenkamp, Supercond. Sci. Tech. **10**, 880 (1997).

[41] M. Naito, H. Yamamoto, and H. Sato, Physica C **335**, 201 (2000).

[42] I. Bozovic, G. Logvenov, M. A. J. Verhoeven, P. Caputo, E. Goldobin, and T. H. Geballe, Nature **422**, 873 (2003).

[43] I. Bozovic, G. Logvenov, M. A. J. Verhoeven, P. Caputo, E. Goldobin, and M. R. Beasley, Phys. Rev. Lett. **93**, 157002 (2004).

[44] G. Koster, B. L. Kropman, G. J. H. M. Rijnders, D. H. A. Blank, and H. Rogalla, Appl. Phys. Lett. **73**, 2920 (1998).

[45] J. G. Simmons, J. Appl. Phys. **34**, 1793 (1963).

[46] E. Wolf, *Principles of electron tunneling spectroscopy* (Oxford University Press, New York, 1989).

[47] H. Weaver, J. Phys. Chem. Solids **11**, 274 (1959).

[48] C. Doughty, A. Walkenhorst, X. X. Xi, C. Kwon, Q. Li, S. Bhattacharya, A. T. Findikoglu, S. N. Mao, T. Venkatesan, N. G. Spencer, et al., IEEE T. Appl. Supercon. **3**, 2910 (1993).

[49] Y. Tanaka and S. Kashiwaya, Phys. Rev. Lett. **74**, 3451 (1995).

[50] G. E. Blonder, M. Tinkham, and T. M. Klapwijk, Phys. Rev. B **25**, 4515 (1982).

[51] J. Z. Wu and W. K. Chu, Phys. Rev. B **49**, 1381 (1994).

[52] B. H. Moeckly, D. K. Lathrop, and R. A. Buhrman, Phys. Rev. B **47**, 400 (1993).

[53] J. R. Kirtley and D. J. Scalapino, Phys. Rev. Lett. **65**, 798 (1990).

[54] A. T. Fiory, S. Martin, R. M. Fleming, L. F. Schneemeyer, and J. V. Waszczak, Phys. Rev. B **41**, 2627 (1990).

[55] Y. Dagan, A. Kohen, and G. Deutscher, Eur. Phys. J. B **19**, 353 (2001).

[56] C. A. Chatzidimitriou-Dreismann, Physica C **219** (1994).

[57] F. Sharifi, A. Pargellis, and R. C. Dynes, Phys. Rev. Lett. **67**, 509 (1991).

[58] P. W. Anderson and Z. Zou, Phys. Rev. Lett. **60**, 132 (1988).

[59] K. Flensberg, P. Hedegård, and M. Brix, Phys. Rev. B **38**, 841 (1988).

[60] H. R. Zeller and I. Giaever, Phys. Rev. **181**, 789 (1969).

[61] L. I. Glazman and K. A. Matveev, Sov. Phys. JETP **67**, 1276 (1988).

[62] M. A. J. Verhoeven, G. J. Gerritsma, H. Rogalla, and A. A. Golubov, Appl. Phys. Lett. **69**, 848 (1996).

[63] J. R. Kirtley, S. Washburn, and D. J. Scalapino, Phys. Rev. B **45**, 336 (1992).

[64] J. R. Kirtley, Phys. Rev. B **47**, 11379 (1993).

[65] M. E. Hawley, K. E. Gray, D. W. Capone II, and D. G. Hinks, Phys. Rev. B **35**, 7224 (1987).

[66] M. D. Kirk, D. P. E. Smith, D. B. Mitzi, J. Z. Sun, D. J. Webb, K. Char, M. R. Hahn, M. Naito, B. Oh, M. R. Beasley, et al., Phys. Rev. B **35**, 8850 (1987).

[67] M. F. Crommie, L. C. Bourne, A. Zettl, M. L. Cohen, and A. Stacy, Phys. Rev. B **35**, 8853 (1987).

[68] Y. Kohsaka, C. Taylor, K. Fujita, A. Schmidt, C. Lupien, T. Hanaguri, M. Azuma, M. Takano, H. Eisaki, H. Takagi, et al., Science **315**, 1380 (2007).

[69] M. Randeria, R. Sensarma, N. Trivedi, and F.-C. Zhang, Phys. Rev. Lett. **95**, 137001 (2005).

[70] M. Grajcar, A. Plecenik, P. Seidel, V. Vojtanik, and K.-U. Barholz, Phys. Rev. B **55**, 11738 (1997).

[71] D. R. Harshman and A. P. Mills, Phys. Rev. B **45**, 10684 (1992).

[72] A. G. Loeser, Z.-X. Shen, D. S. Dessau, D. S. Marshall, C. H. Park, P. Fournier, and A. Kapitulnik, Science **273**, 325 (1996).

[73] G. V. M. Williams, J. L. Tallon, E. M. Haines, R. Michalak, and R. Dupree, Phys. Rev. Lett. **78**, 721 (1997).

[74] A. Ino, T. Mizokawa, K. Kobayashi, A. Fujimori, T. Sasagawa, T. Kimura, K. Kishio, K. Tamasaku, H. Eisaki, and S. Uchida, Phys. Rev. Lett. **81**, 2124 (1998).

[75] A. Ino, C. Kim, M. Nakamura, T. Yoshida, T. Mizokawa, A. Fujimori, Z.-X. Shen, T. Kakeshita, H. Eisaki, and S. Uchida, Phys. Rev. B **65**, 094504 (2002).

[76] T. Sato, T. Yokoya, Y. Naitoh, T. Takahashi, K. Yamada, and Y. Endoh, Phys. Rev. Lett. **83**, 2254 (1999).

[77] T. Yoshida, X. J. Zhou, D. H. Lu, S. Komiya, Y. Ando, H. Eisaki, T. Kakeshita, S. Uchida, Z. Hussain, Z. X. Shen, et al., J. Phys. Cond. Mat. **19**, 125209 (2007).

[78] H.-J. H. Smilde, H. Hilgenkamp, G. Rijnders, H. Rogalla, and D. H. A. Blank, Appl. Phys. Lett. **80**, 4579 (2002).

[79] I. Asulin, A. Sharoni, O. Yulli, G. Koren, and O. Millo, Phys. Rev. Lett. **93**, 157001 (2004).

Chapter 4 Interface resistance of $YBa_2Cu_3O_{7-\delta}/La_{0.67}Sr_{0.33}MnO_3$ ramp-type contacts

Abstract

We fabricated and characterized $YBa_2Cu_3O_{7-\delta}/La_{0.67}Sr_{0.33}MnO_3$ (YBCO/LSMO) ramp-type contacts and junctions. It was found that, on average, the resistance of this particular interface is high compared to the resistance of YBCO interfaces to several other materials, among which the epitaxially grown ferromagnetic oxide $SrRuO_3$. The YBCO/LSMO interfaces were characterized electrically and were found to show a large negative, linear magnetoresistance. From the comparison of the various materials and electron energy loss spectroscopy experiments, we conclude that the high interfacial resistance is likely explained by the effect of charge transfer at the interface. The observed magnetoresistance can be understood from the interplay between the induced antiferromagnetic region in the YBCO and the spin polarization in the LSMO.

4.1 Introduction

The behavior of heterostructures is often strongly influenced by the physics at the interfaces. In this respect, studies on the $YBa_2Cu_3O_{7-\delta}/La_{0.67}Sr_{0.33}MnO_3$ (YBCO/LSMO) interface are of high importance, because of the exotic properties of the constituents, namely high-temperature superconductivity in YBCO and full spin polarization[1] (or half-metallicity) in LSMO.

In YBCO/LSMO/YBCO junctions in the superconducting regime, the half-metallic nature of the barrier might induce spin-triplet supercurrents.[2–4] Future applications consisting of LSMO/YBCO/LSMO trilayers might employ switching of the ferromagnetic layers to turn on and off superconductivity through the superconducting spin-switch mechanism,[5,6] the injection of spin-polarized electrons,[7,8] or stray fields.[9] Furthermore, crossed Andreev reflection might be especially pronounced in these structures due to the half-metallic nature of LSMO.[10,11]

It is, however, not only in the superconducting regime that interesting phenomena can be expected. A transition from metallic to insulating behavior was

reported near the YBCO/$La_{0.67}Ca_{0.33}MnO_3$ (LCMO) interface, both in the superconducting and the normal state.[12] As a possible explanation, a long range charge transfer between the two materials was put forward. Such a mechanism was also mentioned to explain the observation of suppressed magnetization near this interface.[13] Recent experiments suggest orbital reconstructions and the formation of covalent Cu-Mn bonds over the interface.[14] The influence of these effects on transport across cuprate/manganite interfaces remains elusive.

Many transport studies on YBCO/LSMO and YBCO/LCMO heterostructures focus on phenomena such as the suppression of T_c in such structures.[15,16] There are a number of studies that report on the transport properties of YBCO/LSMO junctions. Sawa *et al.*[17] investigated cross-strip junctions, in which they found a zero-bias conductance peak (ZBCP) and an asymmetric background conductance. The data were shown to be consistent with theory for tunneling spectroscopy on *d*-wave superconductor/half-metal junctions, if the presence of an insulating ferromagnetic layer in between was assumed. Chen *et al.*[18] performed differential conductance measurements in a planar geometry, and discussed the role of Andreev bound states in such structures. The interface conductivity for YBCO/LCMO planar junctions was investigated by Mikheenko *et al.*,[19] who suggested that the observed resistance increase at low temperatures stems from the interplay between spin polarization in LCMO and antiferromagnetic spin fluctuations in YBCO in the pseudogap state.

In this chapter we will employ ramp-type structures. The advantage of this configuration is twofold. In the first place, transport takes place in the direction of YBCO's crystallographic *ab* plane, in which the superconducting coherence length is the largest. Secondly, the fabrication process yields well-defined small-area junctions, allowing for a precise determination of the specific junction resistance, R_nA, and critical current density, J_c. Little work has been done in this direction. Huang *et al.* report on the fabrication and characterization of YBCO ramp junctions with manganite barriers.[20] They find a large normal state resistance for their junctions, which largely exceeds the value expected from the bulk resistivity of the barrier material. Some of their junctions exhibit a supercurrent. Schoop *et al.*[21] investigated in-plane YBCO/LCMO contacts as well as ramp-type junctions with an LCMO barrier. Their junctions can be divided into two categories: low-resistive junctions, showing a supercurrent with a large excess current component and high-resistive junctions, showing insulating behavior at low temperatures.

In our work we apply an interlayer technique, which was found to improve the quality of high-T_c/low-T_c superconducting contacts dramatically and to decrease the normal state resistance of those junctions by a factor of 10^4 (Ref. 22). Without vacuum breaking, the YBCO ramp is etch-cleaned, after which the YBCO interlayer is grown in order to repair the stoichiometry at the ramp and subsequently the top electrode is grown. It is expected that the interlayer technique can be useful for all-oxide junctions as well.

Despite the use of an interlayer, we find that the YBCO/LSMO interface is characterized by an unusually large contact resistance, which is the central theme

Table 4.1: Structures used in this research. The interlayer material is YBCO, unless specified otherwise.

Name	Interlayer thickness (nm)	Top electrode
SFS1	7	8 nm LSMO, 100 nm YBCO
SFS2	7	30 nm LSMO, 100 nm YBCO
SF1	7	100 nm LSMO
SF2	20	100 nm LSMO
SF3	7	280 nm SRO
SN1	10	Au
SN2	10 Ca-YBCO[a]	Au
SN3	7	Pt

[a] $Y_{0.7}Ca_{0.3}Ba_2Cu_3O_{7-\delta}$

of this research. We have compared different structures and replaced the LSMO by several other materials, in order to investigate the origin of the high resistance. A summary of the different structures used, can be found in Table 4.1.

4.2 Experimental details

4.2.1 Sample fabrication

All structures were grown with pulsed laser deposition on $SrTiO_3$ (STO) substrates. The STO (001) substrates were chemically treated[23] and annealed for at least two hours at 950 °C in an oxygen flow to produce atomically flat, TiO_2-terminated surfaces. The deposition settings for the various materials are summarized in Table 4.2. All junctions and contacts (see Fig. 4.1) were formed from a bilayer consisting of a 200 nm YBCO base electrode and a 100 nm STO insulation layer. After the growth of the bilayer, the sample was cooled down to 600 °C, at which temperature the oxygen pressure was increased to slightly below atmospheric pressure. The sample was then cooled down to room temperature at a rate of 4 °C min^{-1}. After this, the bottom electrode with the ramp was defined by photolithography and a subsequent argon ion milling step under an angle of 45°. During the etching, the sample was rotated in plane. Then, the photoresist was removed and the sample was placed back in the deposition chamber, where the exposed ramp was cleaned by argon ion milling. The etch-cleaning was performed in two steps: the first step with an acceleration voltage of 500 V to remove amorphous material from the ramp, the second step with 50 V to improve the smoothness of the ramp. In both steps, the sample was oriented perpendicular to the ion beam. After the cleaning, a thin interlayer of YBCO was grown using the normal YBCO deposition settings. After this, the top electrode was grown and the sample was cooled down using the annealing procedure described above. For Au

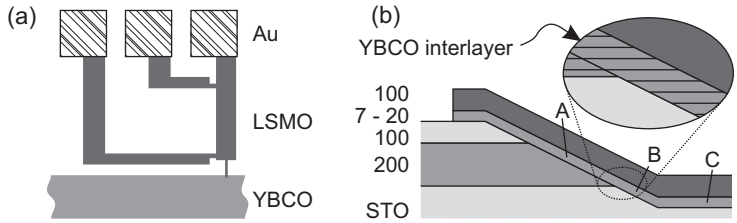

Figure 4.1: (a) Geometry of the structures used in this chapter. The top electrode is fabricated with one current and two voltage contacts, to allow the determination of its resistivity, in order to subtract the electrode contribution from the junction resistance, in the case of a non-superconducting top-electrode. The junctions are 10 or 40 μm wide. (b) Schematic view of the junction cross-section. The layer thicknesses are as indicated (in nm). Three distinct interlayer parts can be identified, here labeled by A, B, and C. The magnified section shows a detailed view of the interlayer. The directions of the YBCO *ab* planes are as shown.

Table 4.2: Pulsed laser deposition settings for the materials used in this research.

Material	Laser fluence ($J\,cm^{-2}$)	Temperature (°C)	Pressure (mbar)
YBCO	1.5	780	0.25 O_2
Ca-YBCO	1.5	780	0.25 O_2
LSMO	2.0	800	0.16 O_2
SRO	2.5	600	0.13 O_2
STO	1.5	740	0.10 O_2
Au	3.5	100	0.22 Ar
Pt	4.3	100	0.10 Ar

and Pt top electrodes, the sample was annealed first and cooled down to 100 °C, before depositing the top electrode. The last step consisted of the definition of the top electrode by photolithography and Ar-ion milling. Each sample consisted of 10 and 40 μm wide junctions. Lastly, Ti/Au contact pads were fabricated by sputter deposition and lift-off.

In the course of the experiments, it was found for LSMO that tuning of the substrate-target distance improved the quality of the epitaxial growth, as witnessed by the peak width in x-ray diffraction measurements. We will investigate the influence of this optimization on the junction properties.

4.2.2 Electrode characterization

The design of the top electrode [see Fig. 4.1(a)] allowed separate electrical characterization of it. The YBCO top electrode showed a T_c varying from 78 to 89 K. For LSMO, resistance-versus-temperature (RT) measurements had the typical LSMO bell-shape, with the maximum at 310 K. The SRO top electrodes showed a Curie temperature of 140 K, as determined from a kink in the RT curve.

It was found that in these all-oxide epitaxial structures the interlayer can become superconducting at much smaller thicknesses than when covered by a Au or Pt top electrode. In the latter case we did not observe superconductivity in 10 nm thick interlayers. When underneath LSMO or SRO, even 7 nm interlayers turn superconducting with a maximum T_c of 25 K. However, a superconducting current path shunting the junction was only observed for SF2, which has a 20 nm interlayer, and SN2, with a 10 nm $Y_{0.7}Ca_{0.3}Ba_2Cu_3O_{7-\delta}$ (Ca-YBCO) interlayer. The absence of a continuous superconducting current path through 7 nm YBCO interlayers likely means that the interlayer is non-superconducting at the bottom of the ramp, i.e., section B as indicated in Fig. 4.1(b). This point will be further discussed in Sec. 4.3.2.

When resistances of contacts with non-superconducting materials are measured, an electrode contribution adds to the contact's interface resistance. To determine this contribution, we locally measure the resistivity of the top electrode. Since the width of the top electrode varies toward the contact, as can be seen in Fig. 4.1(a), a finite element method was used to numerically calculate the electrode resistance. In this way, we can accurately determine the contact resistance, which typically is about 10 % of the total measured resistance.

4.2.3 Scanning SQUID microscopy

SFS1 has been examined in a scanning SQUID microscope (SSM).[24] The sample contained a ring-shaped structure allowing a closed current path through the YBCO of the base and top electrode via two YBCO/LSMO/YBCO junctions. The sample was cooled down to 4.2 K in zero magnetic field. A pick-up loop with an effective area of about 10 μm^2 coupled to a SQUID magnetometer was scanned over the sample while in contact with the surface. This way, the perpendicular component of the magnetic field at the sample surface is predominantly measured. The result is shown in Fig. 4.2(a). Despite the small thickness of the LSMO layer of 8 nm, a magnetic signal is clearly visible. Stray fields from ferromagnetic domain walls penetrate the 100 nm thick superconducting layer covering the LSMO. This observation will be of importance to Chapter 5. The largest stray fields are observed near the junctions. This is not just because there the stray fields can come out from under the YBCO of the top electrode, since this is the case for the entire boundary of the top electrode. Instead, we believe that the increased stray fields in the junction region indicate the upward bending of magnetic field lines by the superconducting YBCO ramp, which is present underneath the LSMO barrier at this position.

4.2.4 Superconducting properties of YBCO/LSMO/YBCO junctions

The main theme of this chapter is the interface resistance of our junctions. For completeness, we will briefly summarize their superconducting properties. On

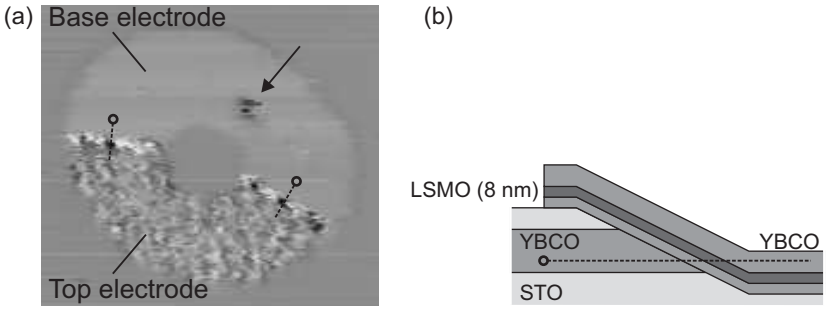

Figure 4.2: (a) Scanning SQUID microscopy graph (4.2 K) of a ring-shaped structure comprising two 40 μm wide junctions. The base electrode is a 200 nm YBCO layer, the top electrode consists of a 7 nm YBCO interlayer, an 8 nm LSMO barrier and a 100 nm YBCO layer, as shown in (b). Despite the small thickness of the LSMO layer, the signal from the ferromagnetic domains is clearly detected at 4.2 K. The sample was cooled down in zero background magnetic field. The largest fields penetrate the junctions. The YBCO base electrode is visible because its inductance is different from the substrate. An Abrikosov vortex is present in the base electrode (indicated by an arrow).

SFS1, roughly 50 % of the junctions showed a supercurrent, the critical current densities J_c being in the range of 0.2–0.6 kA cm^{-2} and featuring I_cR_n (I_c is the critical current of the junction and R_n the normal state resistance) products of up to 2.5 mV at 4.2 K. (Throughout this chapter, we use the full ramp area $A = Wd/\sin\alpha$, with W the junction width, d the thicness of the YBCO bottom electrode and α the ramp angle, for the determination of J_c and R_nA.) When using an effective barrier thickness of 300 nm (the London penetration depth for YBCO is about 150 nm), we find a Josephson penetration depth $\lambda_J \approx 15$ μm. Upon microwave irradiation, Shapiro steps were observed clearly, however the modulation of the critical current in a magnetic field remained below 1 % up to 1 mT. For the given λ_J, a larger modulation could be expected for a homogeneous Josephson junction. In SFS2, only one junction showed a supercurrent, and the modulation in magnetic field showed the typical SQUID-like periodic pattern. This is most likely caused by the presence of separate pinholes in this specific junction. The high I_cR_n values and absence of field dependence in the other junctions that show supercurrents, strongly point in the direction of the presence of pinholes in these junctions too. We did not find unambiguous Josephson junction behavior in one of our samples. The presence of pinholes did not strongly influence the junction R_nA. All junctions exhibit R_n values within the same range and the influence of pinholes on R_n is therefore negligible. This is possible because of the small size of the pinholes. We have not excluded the junctions with pinholes from the analysis of the interface resistance.

4.3 Experimental results

4.3.1 YBCO/LSMO/YBCO junctions

The normal state resistances of junctions on samples SFS1 and SFS2 at 4.2 K are displayed in Fig. 4.3(a). Although the data show a large spread around the mean, the normal state resistances are on average unusually high. For comparison, we fabricated a YBCO/Au ramp-type contact which showed an $R_{\mathrm{n}}A$ of 0.03 $\mu\Omega\mathrm{cm}^2$, which is equal to the value reported for YBCO/Au/Nb ramp-type junctions.[22] For the YBCO/LSMO/YBCO junctions, we find a logarithmic average of 2.6 $\mu\Omega\mathrm{cm}^2$ (the normal average yields 3.5 $\mu\Omega\mathrm{cm}^2$). This number exceeds the resistance that can be expected from the bulk LSMO resistivity by a factor of 10^3. The reason that SFS2 tends to have a somewhat lower interface resistance, despite the thicker LSMO barrier, is likely due to the optimization of the substrate-target distance, as described in Sec. 4.2.1.

We characterized one of the junctions (with no measurable supercurrent) on SFS1 , by recording a differential conductance spectrum, $\mathrm{d}J/\mathrm{d}V(V)$, measuring the temperature dependence of its resistance and the magnetoresistance [Fig. 4.3(b-d)]. The conductance spectrum measured at 2 K clearly shows a zero bias conductance peak (ZBCP). The width of this peak is larger than the conductance peaks due to supercurrents usually are and therefore cannot be attributed to the presence of a small supercurrent in the junction. The conductance spectrum further shows a linear background conductance and a kink at 18 mV. In all these details the spectrum compares well to data obtained from YBCO/LSMO cross-strip junctions that are reported in the literature.[17] In those junctions, the contact between the YBCO and LSMO is partially in the *ab* direction. The data were interpreted in terms of Andreev bound states in ferromagnet/ferromagnetic insulator/*d*-wave superconductor junctions.[25] The similarities between the literature spectra and ours indicate that such a ferromagnetic insulator might be present in our junctions as well. This scenario would imply either a spin polarization of the ferromagnetic insulator of less than 100 % or the presence of domain walls, since the ZBCP would be suppressed by full spin polarization.[17] In Fig. 4.2, we have seen that domain walls can be present in our junctions.

Figure 4.3(c) depicts the temperature dependence of the junction resistance. The result is representative for other junctions on SFS1 and SFS2. The transition temperatures of the base and top electrode (89 K) cannot be distinguished. Above T_{c}, we have subtracted the YBCO electrode contribution yielding the bare junction resistance. It shows a minimum around 200 K. The sharp dip around T_{c} of the YBCO electrode is an artifact of the subtraction procedure. Below T_{c} the junction resistance increases and shows a maximum at 25 K. The decrease of resistance below that temperature is ascribed to the developing ZBCP at low temperature.

Ramp-type junctions fabricated without interlayer sometimes show a strongly increasing resistance for low temperatures.[20,21] This is apparently diminished by the use of an interlayer. Our junction resistances compare well to the literature

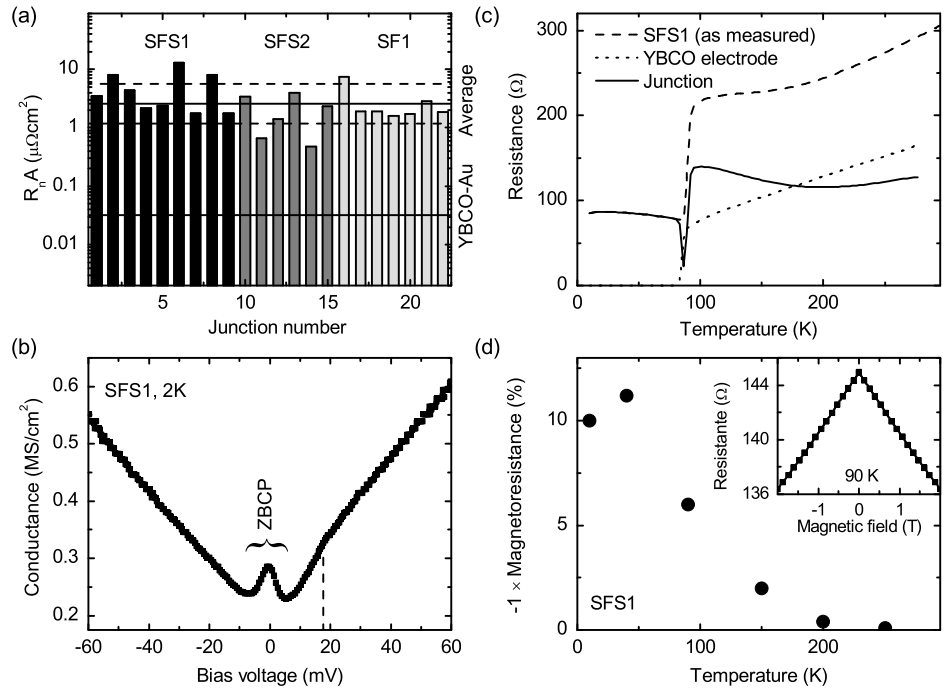

Figure 4.3: (a) Summary of the specific resistances at 4.2 K of 15 YBCO/LSMO/YBCO junctions and 7 YBCO/LSMO contacts on three different samples. The logarithmic average yields 2.6 $\mu\Omega cm^2$. The logarithmic standard deviation is indicated by dashed lines. For comparison, the resistance of YBCO/Au junctions is indicated in the graph as well. (b) The conductance spectrum of one of the 10 μm wide SFS1 junctions at 2 K. It features a ZBCP, a linear background and a kink at 18 mV (indicated by a dashed line). (c) Temperature dependence of the junction resistance. The dashed line is as measured and the solid line is with the electrode contribution (dotted line) subtracted. The T_c's of the top and bottom electrode cannot be distinguished. Below T_c, the junction resistance shows a maximum at 25 K and above T_c, a minimum near 200 K. (d) The junction resistance exhibits a linear, negative magnetic field dependence (shown in the inset). The magnetoresistance (at 2 T) is shown for different temperatures. Magnetoresistance appears around 200 K.

values for selected junctions that do not show such a strong increase.[17,21]

Figure 4.3(d) shows the magnetoresistance, $[R(2\ \mathrm{T}) - R(0\ \mathrm{T})]/R(0\ \mathrm{T})$, of the junction as a function of temperature. The negative and linear magnetoresistance vanishes above 200–250 K, which coincides with the minimum in the RT measurement. This point will be discussed in more detail in Sec. 4.4.

4.3.2 YBCO/LSMO contacts

In addition to junctions, we have also fabricated YBCO/LSMO contacts and determined the interface resistance at 4.2 K by subtraction of the electrode contribution.

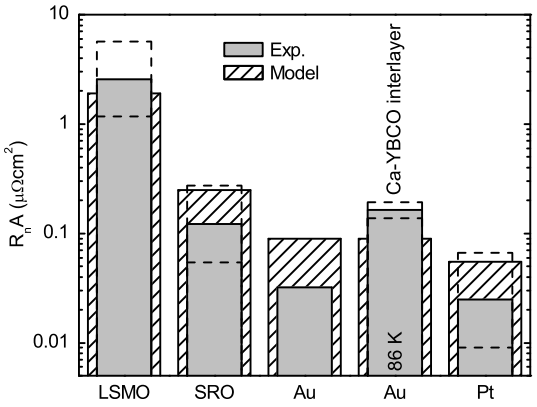

Figure 4.4: Summary of the interface resistances (narrow, grey bars) for contacts with YBCO for different materials. Logarithmic standard deviations are indicated by dashed lines. All resisances are determined at 4.2 K, except for the junction with the Ca-YBCO interlayer. The wider, hatched bars are estimates from a Schottky junction model as described in Sec. 4.4.

The values found are comparable to the ones found for the junctions, indicating that the resistance stems from the YBCO/LSMO interface. A possible factor of 1/2 due to the fact that the contacts contain a single YBCO/LSMO interface and the junctions two, cannot be resolved due to the scatter of the data.

As was noted in Sec. 4.2.1, the interlayer of SF1 underneath the LSMO top electrode [region C in Fig. 4.1(b)] becomes superconducting below 25 K despite of its small thickness of 7 nm. However, the contact resistance does not vanish when the interlayer becomes superconducting, indicating the absence of a superconducting path between the interlayer part C and the YBCO base electrode. Most likely, the non-superconducting region is part B of the interlayer, grown on the bottom of the ramp. The current is then forced to pass through the LSMO electrode and the YBCO/LSMO interface. It is an interesting possibility that the suppression of superconductivity in part B of the interlayer is induced by the proximity of the LSMO, similar to the suppression observed for *c*-axis YBCO/LCMO superlattices.[12,16,26] The fact that superconductivity is not suppressed in part C of the interlayer could be explained by a less effective coupling in the *c* direction. We have increased the interlayer thickness to 20 nm for SF2 and for this case we did observe a superconducting path over the ramp. We thus know that a possible suppression of superconductivity in YBCO by contact with LSMO in the *ab* direction takes place over length scales smaller than 20 nm.

4.3.3 Comparison to other materials

We have already mentioned the comparison with YBCO/Au junctions, to point out the unusually large normal state resistance of the YBCO/LSMO junctions, despite

the use of an interlayer. The extension to other materials could shed a further light on this. Therefore, we varied the top electrode material and included the oxide ferromagnet $SrRuO_3$. Although in the bulk, SRO is orthorhombic, it is very close to the cubic perovskite structure.[27] It can grow fully coherent on STO. Our x-ray measurements show a slightly elongated lattice constant in the *c*-direction of 3.95 Å, whereas the pseudocubic lattice constant is 3.93 Å; most likely, the elongation is caused by the epitaxial compressive strain from the STO substrate. The difference in lattice constant of less than 2 % compared to LSMO, together with the fact that both materials are grown at high temperatures and exposed to the same annealing procedure, justify a direct comparison of the two materials. In addition, we fabricated YBCO/Pt junctions and YBCO/Au junctions in which the YBCO interlayer was replaced by $Y_{0.7}Ca_{0.3}Ba_2Cu_3O_{7-\delta}$ (Ca-YBCO). The latter was expected to reduce R_nA since the effects of Ca are to induce additional holes in YBCO and to significantly lower grain boundary resistances.[28–31] The number of junctions measured to determine the average R_nA were 5, 2, and 4 for the cases of Pt, Ca-YBCO/Au, and SRO. The grey bars in Fig. 4.4 summarize the results (the wider, hatched bars are calculated results of the Schottky junction model as will be discussed in Sec. 4.4). All normal state resistances are measured at 4.2 K, except for the junctions with Ca-YBCO interlayer, since superconductivity in the interlayer led to a superconducting shunt. The average junction R_nA of 0.1 $\mu\Omega cm^2$ for the YBCO/SRO contacts is lower by more than a factor of 20 than for the YBCO/LSMO interfaces. This indicates that the high resistance of the latter can not be an effect of ferromagnetism alone, although it might contribute. The YBCO/SRO values compare reasonably well to values listed in the literature,[32,33] but the average value and the spread might be slightly smaller in our case due to the application of the interlayer. The YBCO/Pt contacts are comparable to the YBCO/Au contacts, which is also the case for *c*-axis contacts.[34] The Ca-YBCO/Au interface resistance was obtained at a higher temperature than the other R_nA values, and it is unclear whether the increase with respect to the YBCO/Au interface should be attributed to the higher measurement temperature, or is intrinsically related to Ca substitution.

4.4 Origin of the interface resistance

There are several possible explanations for the large resistance of the YBCO/LSMO interface. These can be divided into (1) electronic effects, such as charge transfer, (2) spin effects due to the spin-polarized nature of LSMO and (3) structural effects, such as defects and oxygen vacancies.

Many studies have demonstrated the possibility of epitaxial growth on YBCO etched ramps.[22,35–37] In transmission electron microscope images, the boundary between the YBCO ramp and the interlayer is indiscernible.[22] Nevertheless, the possibility remains that the material grown on the ramp possesses an increased number of defects, which can lead to bad conductivity. The mere presence of elastic

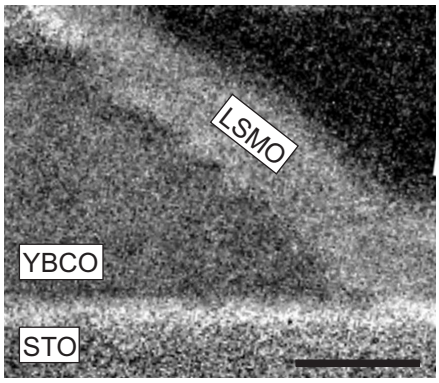

Figure 4.5: Oxygen mapping of the junction obtained with EELS. Oxygen depletion near the YBCO/LSMO interface is below the detection limit. Note the increased intensity at the YBCO/STO interface. The scale bar denotes 100 nm.

scatter centers cannot account for the high $R_{\mathrm{n}}A$ value for YBCO/LSMO interfaces. Assuming that the interface resistance comes from a region less than 10 nm thick, which is likely from the discussion in section 4.3.2, the specific resistivity, ρ, would have to be larger than 2 Ωcm for LSMO. Within the Drude model, we estimate the scattering time τ from $\rho = m_{\mathrm{e}}/ne^2\tau$, with m_{e}, n and e the electron mass, density and charge respectively. From $l_{\mathrm{e}} = v_{\mathrm{F}}\tau$, with v_{F} the Fermi velocity, we conservatively estimate the mean free path $l_{\mathrm{e}} < 0.02$ Å, smaller than the interatomic distance. The resistance arising from elastic scattering is thus unlikely.

Instead, the presence of a carrier depleted insulating or nearly insulating region more likely underlies the high $R_{\mathrm{n}}A$. An often suggested cause for insulating behavior is oxygen off-stoichiometry at the interface. There are two possible reasons for such an off-stoichiometry to arise: (1) the migration of oxygen from one material to the other and (2) the creation of vacancies or interstitial oxygen near the interface as a result of epitaxial strain.

Possibility (1) can be expected if it is accompanied by a lowering of the Gibbs free energy. We estimate whether this is the case by comparing the free energy changes upon oxidation[38] for the individual elements in the materials under study. For Au and Pt, the free energy change is positive and it is therefore unlikely that these materials would take up oxygen out of the YBCO. The largest free energy decrease (per oxygen atom and at 300 K) is shown by Y, followed by La, Sr, Ba, Mn, Cu and Ru, the latter two significantly smaller than the others. Therefore, oxygen migration is expected to be the strongest from YBCO to LSMO and to a lesser degree from YBCO to SRO, or perhaps even from SRO to YBCO. The increasing tendency for oxygen migration in YBCO/Pt, YBCO/Au, YBCO/SRO and YBCO/LSMO junctions is thus compatible with the observed increasing junction $R_{\mathrm{n}}A$ for these interfaces. We note, however, that in the process of epitaxial growth and in the subsequent annealing step, abundant oxygen is present. Under

such circumstances, single thin films are fully oxidized and it can be questioned why this would not be the case for heterostructures consisting of two materials.

The interplay between oxygenation and strain [scenario (2)] was clearly demonstrated in the cuprate parent compound La_2CuO_4.[39] In the present case the lattice mismatch between LSMO ($a = 3.885$ Å) and YBCO in the direction of the chains ($b = 3.88$ Å) is nearly zero. LSMO thus does not hinder the uptake of oxygens in the YBCO chains and an oxygen deficiency due to strain seems unlikely. SRO has a slightly larger lattice constant (3.95 Å in the c-direction and likely some 3.92 Å in the a- and b-directions, assuming the volume of the unit cell remains constant under strain). As a result, oxygen at interstitial sites might be present. The additional oxygen would donate holes to the YBCO CuO_2 planes. The interfacial resistance of YBCO/SRO is indeed smaller than that of YBCO/LSMO. Although both oxygen off-stoichiometry scenarios (1) and (2) are consistent with the observed trends, there are some unsatisfactory features.

We estimate from literature values for the resistivity of strongly oxygen depleted YBCO (with on average 6.2 oxygen atoms per unit cell) (Ref. 40) that a 10–100 nm oxygen deficient layer would be needed to explain the YBCO/LSMO interface R_nA. The presence of such a layer would be reflected in a strongly increasing resistance with decreasing temperatures, which is incompatible with our experimental results. Second, because of the inert nature of Au and Pt, oxygen off-stoichiometry is unlikely for the YBCO/Pt and YBCO/Au contacts. Nevertheless, the resistances of these contacts are larger than expected for highly transparent interfaces. A value of $2 \times 10^{-10}\ \Omega\,\mathrm{cm}^2$ was estimated for the YBCO/noble metal interface, taking into account the mismatch of Fermi velocities.[34] The latter argument of course cannot exclude a possible contribution of oxygen depletion to the YBCO/LSMO and YBCO/SRO interfaces.

As a test for the presence of oxygen off-stoichiometry near the YBCO/LSMO interface, we have performed electron energy loss spectroscopy (EELS) on the ramp region of SF1. With a focused ion beam, a transmission electron microscopy (TEM) specimen was prepared, allowing a cross-sectional view of the YBCO/LSMO contact. Using energy-filtered TEM, images were recorded before and after the ionization edge of the O K shell. An oxygen mapping was obtained by subtracting the pre-edge image from the postedge image. The result is shown in Fig. 4.5. With the resolution we could achieve and a detection limit of about 5 %,[41] it seems clear that the oxygen content of the YBCO and LSMO film is homogeneous to within at least 10 nm of the ramp and we find no indications for a 10–100 nm oxygen deficient layer. We therefore conclude that, although we cannot fully exclude the influence of oxygen off-stoichiometry, an additional mechanism leading to interface resistivity must be active.

A candidate is the electronic mechanism of charge transfer across the interface, which was proposed to be of importance to interfaces involving cuprate superconductors.[30,42] The transfer of charge can lead to the formation of a charge carrier depleted region on one or both sides of the junction, which gives rise to interface resistance. For YBCO/metal interfaces, the formation of a Schottky barrier can

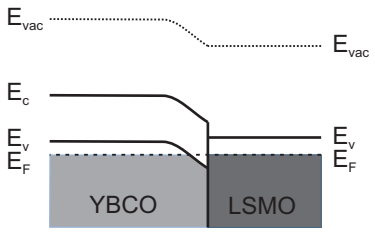

Figure 4.6: Schematic view of the band bending picture for the YBCO/LSMO interface. The larger work function of YBCO leads to a downward bending of the bands and consequently to a depletion of holes near the interface. Note that YBCO is treated as a degenerate semiconductor, which is appropriate due to the relatively large carrier density. Therefore, the Fermi energy is depicted below the bandgap in the valence band.

be expected as for semiconductor/metal interfaces. Schottky barriers result from work function differences between the semiconductor and the metal. A Schottky barrier was suggested to underlie the low interface transparency of YBCO/Au and YBCO/Pt interfaces.[34] Tunnel experiments with YBCO/Au/Nb junctions have indeed demonstrated the presence of a tunnel barrier at the YBCO/Au interface.[43]

The transfer of charge across the YBCO/LCMO interface was suggested by several experiments.[12,13] Theory predicts a 2-3 unit cell thick antiferromagnetic insulating region in the cuprate resulting from charge transfer, which also for this interface is driven by the work function difference between YBCO and LCMO.[44] However, the phase diagrams of strongly correlated materials are complex and rich and substantial deviations from ideal Schottky behavior can be expected. Schottky behavior would be easily recognizable in current-voltage-characteristics from the rectifying properties of the Schottky junction. We have indeed measured some asymmetry in the YBCO/LSMO conductance for opposite polarities [Fig. 4.3(b)]. For the low bias voltages at which we have measured, no strong rectification can be expected. Moreover, the conductance spectrum for the YBCO/LSMO junction is dominated by a linear background which might have an origin unrelated to the Schottky junction (see Sec. 3.3.3).

It is instructive to obtain an estimate of the interface resistances for the various material combinations from the Schottky junction model. The picture we have in mind is sketched in Fig. 4.6. YBCO is depicted as a p-type degenerate semiconductor, with the Fermi energy below the bandgap in the valence band. As a result of the work function difference between YBCO and LSMO, the YBCO bands bend downward. This leads to the depletion of holes in the YBCO near the interface. Transport through the junction is expected to be dominated by tunneling (instead of thermionic emission), because the high carrier density leads to a small depletion width. More quantitative, the appropriate regime is determined by E_{00}, defined by $E_{00} \equiv e\hbar\sqrt{n/m_e\epsilon_r\epsilon_0}/2$ with $\hbar$ the reduced Planck constant, ϵ_r and ϵ_0 the relative and vacuum permittivity, respectively. The condition $E_{00} \gg k_B T$ (k_B being the

Boltzmann constant) is fulfilled, which means that the junction is in the tunneling regime.[45] The junction resistance then follows from[45]

$$R_{\mathrm{n}}A = \frac{k_{\mathrm{B}} \sin \pi c_1 k_{\mathrm{B}} T}{A^{**} \pi e T} \exp \frac{\phi}{E_{00}}\,, \tag{4.1}$$

with

$$c_1 = \frac{1}{2E_{00}} \ln \frac{4\phi}{E_{\mathrm{v}} - E_{\mathrm{F}}}\,. \tag{4.2}$$

Here ϕ is the Schottky barrier height, which for the ideal Schottky junction is equal to the difference between the work functions of the two materials. For the effective Richardson constant A^{**} we take the free electron value of 120 $\mathrm{A/cm^2K^2}$ and we further use the parameters $n \approx 10^{21}$ $\mathrm{cm^{-3}}$, $\epsilon_r \approx 30$ (Ref. 46) and for the energy separation between the Fermi energy and the valence band $E_{\mathrm{v}} - E_{\mathrm{F}} \approx 0.1$ eV (Ref. 47).

The work function of LSMO is 4.8-4.9 eV.[48–50] Au and Pt have work functions of 5.1 and 5.65 eV, respectively.[51] For SRO, the values in the literature vary from 5.0-5.2 eV.[50,52–54] The interface resistance of the YBCO/SRO interface is larger than that of the YBCO/Au interface, which implies a larger energy barrier. We therefore take the value of 5.0 eV for SRO. The scatter in work function data for YBCO is particularly large, the work function will likely be in the range of 5–6 eV: a work function of about 5 eV was found in Refs. 55–57, whereas values up to 6 eV and even higher were reported in 58 and 59. If we take the YBCO work function to be 5.6 eV, we evaluate the junction $R_{\mathrm{n}}A$ for LSMO, SRO and Au as indicated by the shaded bars in Fig. 4.4 For Pt, the work function is almost equal to 5.6 eV, which would yield a vanishingly small $R_{\mathrm{n}}A$. However we find that the effective work function of Pt, when grown on HfO_2 is reduced to 5.15 eV. We used this value for the YBCO/Pt $R_{\mathrm{n}}A$ estimate in Fig. 4.4. We like to stress here that the calculation of the Schottky resistance only serves as an illustration and is not meant to argue that the interfaces described in this chapter behave as ideal Schottky junctions. Nevertheless, the estimated values are quite well in the range of the experimental ones. We have not taken into account deviations from ideal Schottky behavior, such as the presence of surface states, which lead to a work function independence of the Schottky barrier.[45] This might be an alternative explanation of why the YBCO/Pt resistance is comparable to the YBCO/Au resistance.

Since the Schottky resistance depends sensitively on the charge carrier density, it is expected that the sample with the Ca-YBCO interlayer has a low interface resistance, because of the induced additional hole doping.[30,31] However, our Ca-YBCO/Au contact shows a higher resistance than the YBCO/Au contact. Although the resistance of the Ca-YBCO interface was measured at 86 K, it is not expected that it is lower than the YBCO/Au resistance at 4.2 K, for the interface resistance only weakly depends on temperature [see Fig. 4.3(c)]. Possibly, the Ca substitution leads to an increased amount of surface states and thereby influences the Schottky barrier height.

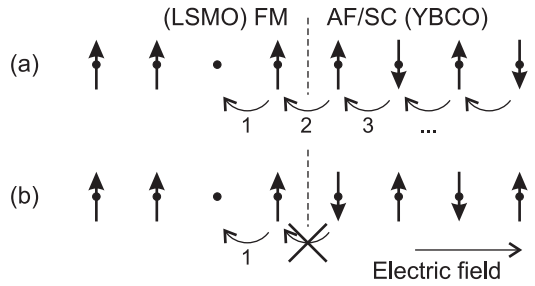

Figure 4.7: Schematic view of a possible mechanism leading to interfacial resistance due to the combination of a high degree of spin polarization in the ferromagnet and antiferromagnetic spin fluctuations in the superconductor. A similar mechanism was suggested in Ref. 19. In (a) the hole in the ferromagnet can freely penetrate into the superconductor under the applied electric field as indicated in the picture. However, in the situation depicted in (b), the hole will be blocked at the interface, since the spin-down electron cannot hop into the ferromagnet.

The width of the charge carrier depleted region can within the Schottky model be estimated from the values we have found for the barrier height by using the standard expression $x_{\mathrm{d}} = \sqrt{2\epsilon_{\mathrm{r}}\epsilon_0\phi/e^2n}$. We find values in the range of 3–4 unit cell, which corresponds roughly to the 2–3 unit cells found by Yunoki *et al.*[44] by static and dynamical mean-field theory. It is well known that the undoped cuprate parent compounds are antiferromagnetic insulators and antiferromagnetism is also expected for the depletion region near YBCO interfaces.[44] One might wonder what would be the interplay between such an antiferromagnetic surface layer and the high degree of spin polarization in LSMO.

Interestingly, we have seen in Fig. 4.4 that the Schottky junction model overestimates the interface resistances of the YBCO/SRO, YBCO/Au, and YBCO/Pt contacts, while it underestimates the resistance of the YBCO/LSMO interface. This might indicate that spin polarization plays a role, since LSMO is reported to be fully spin polarized,[1] while the spin polarization of SRO is about 50 %.[60] The additional resistance exhibited by the YBCO/LSMO interface might well be related to the half-metallic nature of LSMO.

Figure 4.7 presents a sketch of the situation arising at the YBCO/LSMO interface. There are two distinct situations. In (a), a hole coming from the side of the LSMO can freely cross the interface, which results in a new configuration of spins in the YBCO as indicated in (b). A second hole will now be blocked at the interface, since the spin-down electron in the YBCO is not allowed to hop into the LSMO. The interplay between antiferromagnetism and half-metallicity can thus induce an additional contribution to the interface resistance. Because of the two-dimensional nature of the interface and a finite antiferromagnetic correlation length, the interface resistance will not be infinite, as the schematic picture in Fig. 4.7 might suggest. Note that for the proposed mechanism the presence of a depletion layer is not strictly necessary. Even in the optimally doped cuprates antiferromagnetic correlations are present.[61–65] Mikheenko *et al.*[19] have suggested

that such correlations contribute to the junction resistance. They reported an increasing junction resistance for planar YBCO/LCMO contacts below 200 K, which temperature was associated with the pseudogap temperature. In our junctions, the junction resistance also increases below 200 K; see Fig. 4.3(c). At the same temperature, magnetoresistance appears. This coincidence indicates a contribution to the interface resistance of magnetic origin, possibly by a mechanism as described above.

4.5 Conclusion

We have observed an unusually large interfacial resistance for YBCO/LSMO interfaces, when compared to several other materials. We have shown that this is likely caused by the phenomenon of charge transfer and resulting carrier depletion in these interfaces, that has received a lot of attention in recent years.[12,13,44] In addition, a contribution related to the spin-polarized nature of LSMO might also be present.

The fundamental origin of the resistivity of YBCO interfaces has important consequences for the fabrication of devices. High-quality interfaces might face a lower boundary of the contact resistance, depending on parameters such as the work function of the material being contacted. The effects of Ca substitution should be further investigated and it would be desirable to apply the Ca only locally on the ramp in order to prevent the Ca-YBCO interlayer from shunting the junction.

In a planar geometry, accurate values for the YBCO/LSMO interface $R_{\mathrm{n}}A$ are difficult to obtain, but they are not expected to be much smaller than the values we have obtained for *ab* contacts. For YBCO/noble metal interfaces, the resistance for a *c*-axis contact is even larger than for an *ab*-axis contact. For *c*-axis YBCO/LSMO and YBCO/LCMO heterostructures, it is often concluded from the atomical sharpness of the interfaces, that the contacts are electrically highly transparent. We challenge this assumption, since the occurrence of charge transfer seems not to be restricted to unsharp interfaces.

The results of this chapter are of relevance to the next chapter, in which we will investigate LSMO/YBCO/LSMO heterostructures in a so-called superconducting spin-switch geometry.[5] For the interpretation of the data, the limited transparency of the YBCO/LSMO is of importance. Switching cannot arise from a mechanism that relies on high interface transparency and in the next chapter, it is confirmed that this is indeed not the case.

References

[1] J. H. Park, E. Vescovo, H. J. Kim, C. Kwon, R. Ramesh, and T. Venkatesan, Nature **392**, 794 (1998).

[2] R. S. Keizer, S. T. B. Goennenwein, T. M. Klapwijk, G. Miao, G. Xiao, and A. Gupta, Nature **439**, 825 (2006).

[3] Y. Asano, Y. Tanaka, and A. A. Golubov, Phys. Rev. Lett. **98** (2007).

[4] M. Eschrig and T. Löfwander, Nat. Phys. **4**, 138 (2008).

[5] L. R. Tagirov, Phys. Rev. Lett. **83**, 2058 (1999).

[6] A. I. Buzdin, A. V. Vedyayev, and N. V. Ryzhanova, Europhys. Lett. **48**, 686 (1999).

[7] V. Peña, Z. Sefrioui, D. Arias, C. Leon, J. Santamaria, J. L. Martinez, S. G. E. te Velthuis, and A. Hoffmann, Phys. Rev. Lett. **94**, 057002 (2005).

[8] N. M. Nemes, M. García-Hernández, S. G. E. te Velthuis, A. Hoffmann, C. Visani, J. Garcia-Barriocanal, V. Peña, D. Arias, Z. Sefrioui, C. Leon, et al., Phys. Rev. B **78**, 094515 (2008).

[9] M. van Zalk, M. Veldhorst, A. Brinkman, J. Aarts, and H. Hilgenkamp, Phys. Rev. B **79**, 134509 (2009).

[10] T. Yamashita, H. Imamura, S. Takahashi, and S. Maekawa, Phys. Rev. B **67**, 094515 (2003).

[11] F. Giazotto, F. Taddei, F. Beltram, and R. Fazio, Phys. Rev. Lett. **97**, 087001 (2006).

[12] T. Holden, H.-U. Habermeier, G. Cristiani, A. Golnik, A. Boris, A. Pimenov, J. Humlícek, O. I. Lebedev, G. Van Tendeloo, B. Keimer, et al., Phys. Rev. B **69**, 064505 (2004).

[13] A. Hoffmann, S. G. E. te Velthuis, Z. Sefrioui, J. Santamaría, M. R. Fitzsimmons, S. Park, and M. Varela, Phys. Rev. B **72**, 1404079(R) (2005).

[14] J. Chakhalian, J. W. Freeland, H. U. Habermeier, G. Cristiani, G. Khaliullin, M. van Veenendaal, and B. Keimer, Science **318**, 1114 (2007).

[15] Z. Sefrioui, M. Varela, V. P. na, D. Arias, C. León, J. Santamaría, J. E. Villegas, J. L. Martínez, W. Saldarriaga, and P. Prieto, Appl. Phys. Lett. **81**, 4568 (2002).

[16] B. S. H. Pang, R. I. Tomov, and M. G. Blamire, Supercond. Sci. Technol. **17**, 624 (2004).

[17] A. Sawa, S. Kashiwaya, H. Obara, H. Yamasaki, M. Koyanagi, N. Yoshida, and Y. Tanaka, Physica C **339**, 287 (2000).

[18] Z. Y. Chen, A. Biswas, I. Žutić, T. Wu, S. B. Ogale, R. L. Greene, and T. Venkatesan, Phys. Rev. B **63**, 212508 (2001).

[19] P. Mikheenko, R. Chakalova, and C. M. Muirhead, Phys. Rev. B **71**, 184517 (2005).

[20] M. Huang, Z. Ivanov, P. Komissinski, and T. Claeson, Physica C **326**, 79 (1999).

[21] U. Schoop, M. Schonecke, S. Thienhaus, F. Herbstritt, J. Klein, L. Alff, and R. Gross, Physica C **350**, 237 (2001).

[22] H.-J. H. Smilde, H. Hilgenkamp, G. Rijnders, H. Rogalla, and D. H. A. Blank, Appl. Phys. Lett. **80**, 4579 (2002).

[23] G. Koster, B. L. Kropman, G. J. H. M. Rijnders, D. H. A. Blank, and H. Rogalla, Appl. Phys. Lett. **73**, 2920 (1998).

[24] A. G. P. Troeman, *NanoSQUID magnetometers and high resolution scanning SQUID microscopy* (Ph.D. Thesis, University of Twente, Enschede, 2007).

[25] S. Kashiwaya, Y. Tanaka, N. Yoshida, and M. R. Beasley, Phys. Rev. B **60**, 3572 (1999).

[26] Z. Sefrioui, D. Arias, V. Peña, J. E. Villegas, M. Varela, P. Prieto, C. León, J. L. Martinez, and J. Santamaria, Phys. Rev. B **67**, 214511 (2003).

[27] C. W. Jones, P. D. Battle, P. Lightfoot, and W. T. A. Harrison, Acta Cryst. Sect. C **45**, 365 (1989).

[28] A. Schmehl, B. Goetz, R. R. Schulz, C. W. Schneider, H. Bielefeldt, H. Hilgenkamp, and J. Mannhart, Europhys. Lett **47**, 110 (1999).

[29] G. Hammerl, A. Schmehl, R. R. Schulz, B. Goetz, H. Bielefeldt, C. W. Schnelder, H. Hilgenkamp, and J. Mannhart, Nature **407**, 162 (2000).

[30] H. Hilgenkamp and J. Mannhart, Rev. Mod. Phys. **74**, 485 (2002).

[31] M. A. Schofield, M. Beleggia, Y. Zhu, K. Guth, and C. Jooss, Phys. Rev. Lett. **92**, 195502 (2004).

[32] R. Dömel, C. Horstmann, M. Siegel, A. I. Braginski, and M. Y. Kupriyanov, Appl. Phys. Lett. **67**, 1775 (1995).

[33] L. Antognazza, K. Char, T. H. Geballe, L. L. H. King, and A. W. Sleight, Appl. Phys. Lett. **63**, 1005 (1993).

[34] H.-J. H. Smilde, *Josephson contacts between high-T_c and low-T_c superconductors* (Ph.D. Thesis, University of Twente, Enschede, 2001).

[35] M. Gustafsson, E. Olsson, M. Q. Huang, P. V. Komissinski, P. B. Mozhaev, and Z. G. Ivanov, J. Low Temp. Phys. **117**, 575 (1999).

[36] Y. Yang, J. Gao, J. L. Sun, T. C. Chui, and L. Li, Physica C **300**, 151 (1998).

[37] J. G. Wen, N. Koshizuka, C. Traeholt, H. W. Zandbergen, E. M. C. M. Reuvekamp, and H. Rogalla, Physica C **255**, 293 (1995).

[38] R. C. Weast, *Handbook of Chemistry and Physics* (CRC Press, 1972), 53rd ed.

[39] W. Si and X. X. Xi, Appl. Phys. Lett. **78**, 240 (2001).

[40] K. Semba, M. Mukaida, and A. Matsuda, Physica B **312**, 74 (2002).

[41] R. F. Egerton, *Electron energy-loss spectroscopy in the electron microscope* (Plenum Press, New York, 1996), 2nd ed.

[42] J. Mannhart and H. Hilgenkamp, Physica C **317-318**, 383 (1999).

[43] B. Chesca, D. Doenitz, T. Dahm, R. P. Huebener, D. Koelle, R. Kleiner, Ariando, H.-J. H. Smilde, and H. Hilgenkamp, Phys. Rev. B **73**, 014529 (2006).

[44] S. Yunoki, A. Moreo, E. Dagotto, S. Okamoto, S. S. Kancharla, and A. Fujimori, Phys. Rev. B **76**, 064532 (2007).

[45] S. M. Sze and K. K. Ng, *Physics of Semiconductor Devices* (Wiley-Interscience, New York, 2007), 3rd ed.

[46] C. Y. Chen, R. J. Birgeneau, M. A. Kastner, N. W. Preyer, and T. Thio, Phys. Rev. B **43**, 392 (1991).

[47] Y. Xu and J. W. Ekin, Phys. Rev. B **69**, 104515 (2004).

[48] M. P. de Jong, V. A. Dediu, C. Taliani, and W. R. Salaneck, J. Appl. Phys. **94**, 7292 (2003).

[49] D. W. Reagor, S. Y. Lee, Y. Li, and Q. X. Jia, J. Appl. Phys. **95**, 7971 (2004).

[50] M. Minohara, I. Ohkubo, H. Kumigashira, and M. Oshima, Appl. Phys. Lett. **90**, 132123 (2007).

[51] H. B. Michaelson, IBM J. Res. Dev. **22** (1978).

[52] K. Fröhlich, K. Hůseková, D. Machajdík, R. Lupták, M. Ťapajna, J. C. Hooker, F. Roozeboom, A. P. Kobzev, C. Wiemer, S. Ferrari, et al., Mat. Sc. Sem. Proc. **7**, 265 (2004).

[53] A. J. Hartmann, M. Neilson, R. N. Lamb, K. Watanabe, and J. F. Scott, Appl. Phys. A **70**, 239 (2000).

[54] X. Fang and T. Kobayashi, Appl. Phys. A **69**, 587 (1999).

[55] J. DeVries, S. S. Wakisaka, and R. E. Spjut, J. Mater. Res. **8**, 1497 (1993).

[56] G. Rietveld, N. Y. Chen, and D. van der Marel, Phys. Rev. Lett. **69**, 2578 (1992).

[57] S. Urazhdin, W. K. Neils, S. H. Tessmer, N. O. Birge, and D. J. Van Harlingen, Supercond. Sci. Technol **17**, 88 (2004).

[58] T. Hirano, M. Ueda, K. Matsui, T. Fujii, K. Sakuta, and T. Kobayashi, Jpn. J. Appl. Phys **31**, L1345 (1992).

[59] S. I. Shkuratov, S. N. Ivanov, and S. N. Shilimanov, Surf. Sci. **266**, 224 (1992).

[60] B. Nadgorny, M. S. Osofsky, D. J. Singh, G. T. Woods, J. R. J. Soulen, M. K. Lee, S. D. Bu, and C. B. Eom, Appl. Phys. Lett. **82**, 427 (2003).

[61] R. J. Birgeneau, D. R. Gabbe, H. P. Jenssen, M. A. Kastner, P. J. Picone, T. R. Thurston, G. Shirane, Y. Endoh, M. Sato, K. Yamada, et al., Phys. Rev. B **38**, 6614 (1988).

[62] E. Dagotto, Rev. Mod. Phys. **66**, 763 (1994).

[63] M. Sato, S. Shamoto, J. M. Tranquada, G. Shirane, and B. Keimer, Phys. Rev. Lett. **61**, 1317 (1988).

[64] J. M. Tranquada, W. J. L. Buyers, H. Chou, T. E. Mason, M. Sato, S. Shamoto, and G. Shirane, Phys. Rev. Lett. **64**, 800 (1990).

[65] J. Rossat-Mignod, L. P. Regnault, M. J. Jurgens, C. Vettier, P. Burlet, J. Y. Henry, and G. Lapertot, Physica B **163**, 4 (1990).

Chapter 5 Magnetization-induced resistance-switching effects in $La_{0.67}Sr_{0.33}MnO_3/YBa_2Cu_3O_{7-\delta}$ bi- and trilayers

Abstract

We have studied the influence of the magnetization on the superconducting transition temperature (T_c) in bi- and trilayers consisting of the half-metallic ferromagnet $La_{0.67}Sr_{0.33}MnO_3$ and the high-temperature superconductor $YBa_2Cu_3O_{7-\delta}$ (YBCO). We have made use of tilted epitaxial growth in order to achieve contacts between the two materials that are partly in the crystallographic *ab* plane of the YBCO. As a result of uniaxial magnetic anisotropy in the tilted structures, we observe sharp magnetization-switching behavior. At temperatures close to T_c, the magnetization-switching induces resistance jumps in trilayers, resulting in a magnetization dependence of T_c. In bilayers, this switching effect can be observed as well, provided that the interface to the ferromagnetic layer is considerably rough. Our results indicate that the switching behavior arises from magnetic stray fields from the ferromagnetic layers that penetrate into the superconductor. A simple model describes the observed behavior well. We find no evidence that the switching behavior is caused by a so-called superconducting spin switch, nor by accumulation of spin-polarized electrons. Observation of magnetic coupling of the ferromagnetic layers, through the superconductor, supports the idea of field-induced resistance switching. This chapter was published identically in Physical Review B.[1]

5.1 Introduction

The interplay between superconductivity and ferromagnetism is a rapidly developing field in condensed-matter physics. In hybrid heterostructures, where the two different orders meet at the interface, interesting physics arises. One of the promising structures is the so-called superconducting spin switch,[2,3] which consists of two ferromagnetic (F) metallic layers, sandwiching a superconductor (S). An early theoretical proposal for a spin switch, involving ferromagnetic insulators, was made by De Gennes.[4] Here, the average exchange field induced in the superconductor depends on the relative orientation of the ferromagnetic layers. As a

result, the superconducting transition temperature T_c depends on this orientation. Recently, such geometries were investigated for the case of metallic weak ferromagnets and it was predicted that, under the right circumstances, superconductivity can be switched on and off by applying a small external field.[2,3] This switching was suggested to result from interference between the superconducting wave functions transmitted through the S/F interface and reflected at the F surface. An alternative scenario for spin switching is in terms of crossed Andreev reflection:[5] when the ferromagnetic layers are magnetized in the antiparallel (AP) direction, Cooper pair formation due to crossed Andreev reflection is enhanced, compared to the parallel (P) configuration. This effect is the largest for strongly spin-polarized magnets, when crossed Andreev reflection occurs *only* in the case of antiparallel magnetization.

Although full switching of superconductivity has never been observed, a resistance drop has been found in F/S/F systems with weak ferromagnets when switching the magnetization from the P to the AP state.[6,7] In systems with strong ferromagnets, the opposite effect was observed by Rusanov *et al.*,[8] which was attributed to an increased number of quasiparticles in the superconductor as a result of the enhanced reflection of the spin-polarized quasiparticles. However, Moraru *et al.*[9,10] found the standard spin-switch effect in a comparable system. The contradictory results might be related to the employment of the exchange bias mechanisms in some of these works.[11] Recently, T_c shifts in F/I/S/I/F (in which "I" denotes an insulator) multilayer systems were observed that could not be fully explained by the spin-switch effect, but were partly attributed to spin imbalance in the superconductor, induced by the ferromagnet.[12] However, it was pointed out by Steiner and Ziemann[13] that stray fields due to specific magnetic domain configurations can lead to changes in T_c. Stamopoulos *et al.*[14,15] reported stray-field-based magnetoresistance in $Ni_{80}Fe_{20}/Nb/Ni_{80}Fe_{20}$ trilayers, which emerges from a magnetostatic coupling of the ferromagnetic layers. The importance of stray fields was further established by Carapella *et al.*,[16] who found that a glassy vortex phase induced by magnetic stray fields explains the switching behavior in their Co/Nb/Co trilayers. Thus, magnetic stray field effects are a potential problem for the interpretation of data obtained on structures with ferromagnets in close proximity to superconductors.

Studies on F/S hybrid systems have not been limited to conventional superconductors and ferromagnets. Combinations of the oxide materials $La_{0.67}Sr_{0.33}MnO_3$ (LSMO) and $La_{1-x}Ca_xMnO_3$ (LCMO) with $YBa_2Cu_3O_{7-\delta}$ (YBCO) have been used because of the high spin-polarization of LSMO (Ref. 17) and the good lattice match, allowing the growth of epitaxial structures. In these systems, large magnetoresistance and an inverse spin-switch effect were found and attributed to the transmission of spin-polarized carriers into the superconductor.[18,19] Vortex effects were ruled out as a cause for the observed phenomena, since no effects were seen in bilayers. Anisotropic magnetoresistance effects were excluded on the basis of the absence of a dependence of the magnetoresistance peak on the relative orientation of current and magnetic field.[20] However, the role of spin injection

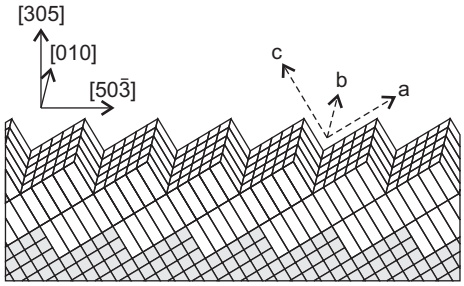

Figure 5.1: Schematic picture of YBCO grown on STO (305). Indicated are the in-plane and out-of-plane crystallographic orientations and the YBCO a, b, and c directions. The c axis makes an angle of 31° with respect to the sample surface.

in LCMO/YBCO structures is not entirely clear. Gim *et al.*[21] found no conclusive evidence of suppression of superconductivity from their quasiparticle injection experiments using LCMO/LSMO and YBCO. A similar conclusion was reached recently by Deng *et al.*[22] from mutual inductance measurements on YBCO/LCMO bilayers, which were optimized for the experiment by growing YBCO with the c axis in the plane of the film. These kind of experiments are performed under equilibrium conditions in the bilayers and might be more comparable to the current-in-plane (CIP) measurements in Ref. 18 than quasiparticle injection experiments. In the mutual induction experiments, suppression of superconductivity was found near the coercive field of the LCMO layer, which was attributed to magnetic field effects.

It has been known from other systems as well that the effects of field can be important. For example, they can give rise to domain-wall-guided superconductivity[23] and flux-flow-induced giant-magnetoresistance (GMR) effects.[24] The volume magnetization of LSMO, $\mu_0 M$, can reach 0.8 T and it therefore is reasonable to expect a strong influence of stray fields. In a recent publication, Mandal *et al.*[25] pointed out a distinct contribution of the dipolar field to the magnetoresistance in F/S/F trilayers with $Y_{0.6}Pr_{0.4}Ba_2Cu_3O_7$ used for the superconductor. However the relative contribution to the magnetoresistance of the depairing due to accumulation of spin-polarized electrons remains unclear. Furthermore, the higher resistance seen in the state of AP magnetization is not understood.

So far, c-axis-oriented YBCO/LSMO superlattices, such as those grown on $SrTiO_3$ (STO) (001) substrates, have been widely exploited. A disadvantage of these structures is the weak coupling between the superconductor and the ferromagnet, due to the strongly anisotropic nature of superconductivity in YBCO. In order to achieve coupling that is (partly) in the ab plane, we will exploit coherently tilted epitaxial growth[26] of YBCO on STO (305) substrates. On these substrates, YBCO grows with the c axis making a 31° angle with respect to the sample surface, as indicated in Fig. 5.1. A second advantage of using the (305)-oriented structures is that remarkably sharp magnetization-switching behavior can be realized, caused

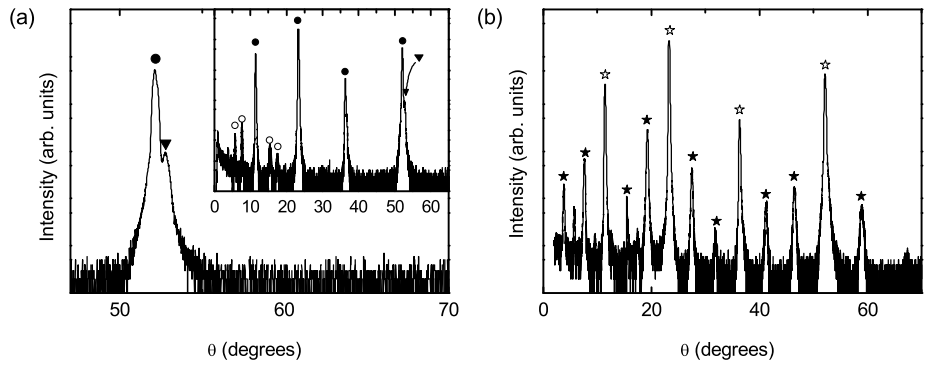

Figure 5.2: (a) θ-2θ scan of LSMO grown on STO (305). Triangles denote LSMO peaks, which largely overlap with the STO peaks, indicated by closed circles. Peaks indicated by open circles are due to higher harmonics in the beam. (b) θ-2θ scan for a YBCO/LSMO bilayer. Filled stars correspond to YBCO peaks; open stars indicate overlapping STO, LSMO, and YBCO peaks.

by the induced uniaxial magnetic anisotropy, with the easy axis along the [010] direction. This enables us to prepare a well-defined state of P or AP magnetization in trilayers.

In this chapter, we show that the trilayer resistance shows a sharp drop when the magnetization is switched from the AP to the P state within the superconducting transition. However, we find that the observed switching behavior is incompatible with the superconducting spin-switch model and models based on spin imbalance. We find a natural explanation in terms of stray fields from the LSMO layers that penetrate the superconductor. Our measurements show clearly that the switching behavior can be understood completely from changes in the effective field when one of the ferromagnetic layers switches. We will show that we can even obtain switching behavior in bilayers, as expected within our model, by exploiting the controllable surface roughness of the ferromagnetic layers.

5.2 Experimental details

5.2.1 Film growth and characterization

All thin films were grown on STO substrates. The STO (001) substrates were chemically treated[27] and annealed for at least 2 h at 950 °C in an oxygen flow to produce atomically flat TiO_2-terminated surfaces. For the (305)-oriented substrates a single termination does not exist, but the surfaces were atomically flat and substrate steps were observed, due to a small miscut with respect to the (305) plane. The thin-film heterostructures were grown with pulsed laser deposition using a laser fluence of 1.5 J cm^{-2} for both YBCO and LSMO. Film thicknesses were in the ranges of 50–150 nm for LSMO and 20–100 nm for YBCO. The deposition

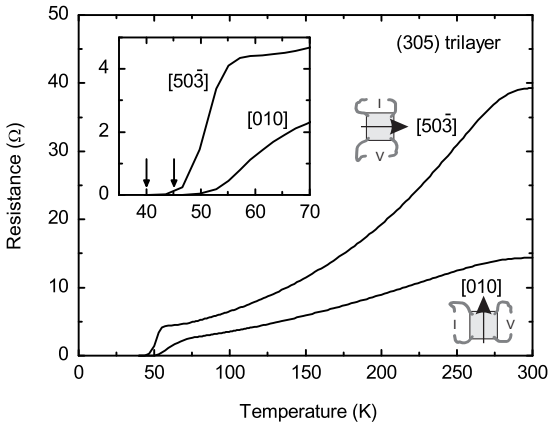

Figure 5.3: Temperature-dependence of the resistance for a (305)-oriented F/S/F trilayer for two different directions of the applied current, as indicated. The layer thicknesses for the bottom F, S, and top F layer are 50, 30, and 150 nm, respectively. The inset shows the behavior around T_c; vertical arrows indicate T_c.

temperature and oxygen pressure were, respectively, 780 °C and 0.25 mbar for YBCO and 800 °C and 0.16 mbar for LSMO. For LSMO, the quality of epitaxial growth depends on the flux rate of the ablated material. We used the substrate-target distance to optimize the epitaxy of the LSMO layers. After deposition, the thin films were annealed for 10 min at 600 °C in oxygen close to atmospheric pressure and subsequently cooled down at a rate of 4 °C min^{-1}.

X-ray-diffraction (XRD) measurements confirmed the epitaxial growth of the multilayers on both types of substrates (Fig. 5.2). YBCO showed a slightly distorted unit cell on STO (305): the angle between the crystallographic a and c axes was 90.7(4)°, resulting in a monoclinic unit cell. However, a single film on STO (305) showed an almost nominal value for T_c of 90 K.

LSMO grows smoothly on STO (305) substrates. Atomic force microscope (AFM) measurements on a 150 nm film showed a root-mean-square (rms) roughness of 2 nm and a peak-to-peak (pp) roughness of 5 nm. YBCO was much rougher with a pp roughness of 30 nm (5 nm rms) for a 100 nm film. The AFM images are shown as insets in Fig. 5.5. We attribute this large roughness to differences in growth rate between the YBCO ab and c directions. Second, nucleation effects are expected, since the YBCO lattice vector in the crystallographic c-direction is three times as large as that of STO. As a result, an integer number of YBCO unit cells will not always fit between two nucleation sites. We therefore expect a large number of antiphase boundaries in these films. When LSMO was grown on top of YBCO, the average roughness did not further increase. For bilayers, this implies that we can choose to grow a smooth LSMO/YBCO interface, by putting the LSMO underneath the YBCO layer, or a rough interface, by putting LSMO

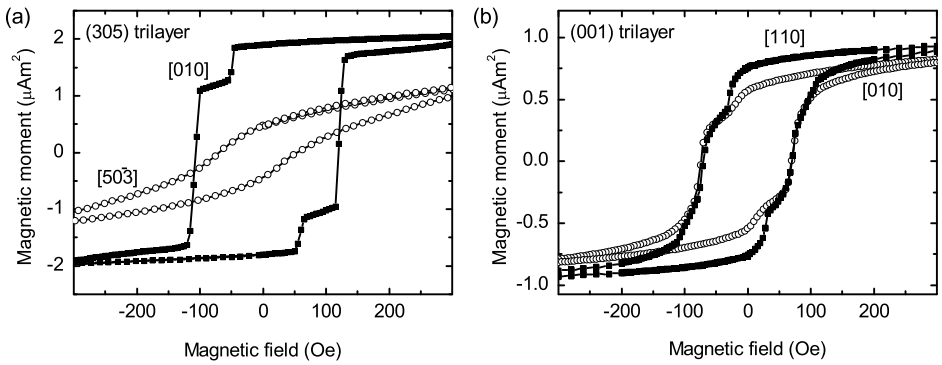

Figure 5.4: Magnetization measurements on (a) (305)-oriented and (b) (001)-oriented F/S/F trilayers. The bottom and top F layers are 50 and 150 nm, respectively; the S layer is 30 nm. Measurements are taken at temperatures slightly above T_c of the superconductor. The magnetic field directions are indicated in the figure. The (305)-oriented trilayers show uniaxial magnetic anisotropy. The magnetization loop for the (001)-oriented trilayers shows somewhat sharper features when measured along the [110] direction than along the [010] direction, in accordance with literature (Ref. 28).

on top of YBCO, making roughness a controllable parameter in unraveling the spin-switch mechanism.

5.2.2 Transport and magnetization properties

Temperature-dependent resistance (RT) measurements on trilayers clearly showed a parallel contribution of both LSMO and YBCO. In Fig. 5.3, RT-curves are shown that are measured for two different directions of the current in a four-point configuration with electrical connections to the corners of the trilayer. This configuration was used in all measurements. In the [010] direction the resistance has a YBCO-like linear temperature dependence. The resistance measured in the [50$\bar{3}$] direction is larger and has the bell shape that is typical for LSMO, indicating that the YBCO resistance is higher in this direction. We attribute this to the c-axis transport component, which is present for this direction. In addition, a contribution of the antiphase boundaries can be expected predominantly in this direction. The thinnest YBCO films in bi- and trilayers exhibited a reduced T_c, probably related to strain effects. In some structures we found two values for T_c depending on the direction of measurement. Thus, a superconducting path between the current electrodes in the [010] direction could be formed at a higher temperature than in the [50$\bar{3}$] direction. By using a zero-resistance criterion for T_c, we found 45 K (40 K in the [50$\bar{3}$] direction), for thickness of 30 nm, which decreased to 20 K (both directions) for 20 nm films.

Magnetization measurements were performed using a vibrating-sample magnetometer (VSM) mounted in the same system in which the transport measure-

ments were taken. In one occasion, a superconducting quantum interference device (SQUID) magnetometer was used. Small field offsets (less than 20 Oe) observed in the VSM were absent in the SQUID magnetometer. Our thin films showed slightly reduced Curie temperatures in the range of 320–350 K. Hysteresis loops with the field oriented along the [010] direction and the $[50\bar{3}]$ direction are presented in Fig. 5.4(a) for an F/S/F trilayer with bottom and top layers of 50 and 150 nm, respectively, and a YBCO thickness of 30 nm. The contributions of the two individual LSMO layers are clearly visible and sharp magnetization switching is observed when the field is applied in the [010] easy direction. Since the magnetic anisotropy of LSMO is sensitive to strain and uniaxial strain was found to induce uniaxial magnetic anisotropy,[29] we expect uniaxial magnetic anisotropy for LSMO on STO (305) as well. Indeed, the $[50\bar{3}]$ direction is clearly not an easy axis. We tried to fit both curves using the Stoner-Wohlfarth model[30] for a single-domain ferromagnet, but could not find a satisfactory fit using a single set of parameters. The (001)-oriented trilayers are expected to show biaxial magnetic anisotropy at low temperatures.[28] Although the difference is small, the magnetization loop measured along the [110] easy direction (measured in the SQUID magnetometer) as shown in Fig. 5.4(b) shows sharper features and larger saturation magnetization than the one measured along the [010] hard direction. Although two coercive fields are observed for both directions, the switching is less sharp than for the (305)-oriented trilayer and the AP state is poorly defined. We conclude that this is due to the biaxial magnetic anisotropy.

5.3 Results and discussion

5.3.1 Resistance switching in F/S bilayers

We have grown bilayers on STO (305) both with the LSMO underneath YBCO (F/S) and with the LSMO on top (S/F). In both structures, the YBCO thickness is 30 nm and the LSMO thickness is 150 nm. Both structures show a reduced T_c of 60 K. The resistance as a function of magnetic field is measured in the superconducting transition (at 61 K) using a CIP technique. Magnetic fields are applied along the easy axis. In the STO (305)/F/S structure, which has a smooth LSMO layer, the observed hysteresis is the largest for temperatures above T_c. Even here, it is smaller than 0.2 % and is a direct result of the butterfly-shaped magnetoresistance of the LSMO layer. The magnetoresistance in the superconducting transition at 61 K is shown in Fig. 5.5(a). When the order of the layers is reversed, which yields a rougher interface, a large hysteresis in the superconducting transition appears, which is too large to arise from the LSMO magnetoresistance. A typical result is depicted in Fig. 5.5(b). Starting from large negative fields, the resistance shows a parabolic dependence on the field with a minimum around -200 Oe. Then, reaching the positive coercive field of 80 Oe, indicated by a vertical arrow, a peak structure can be observed in the magnetoresistance. Above

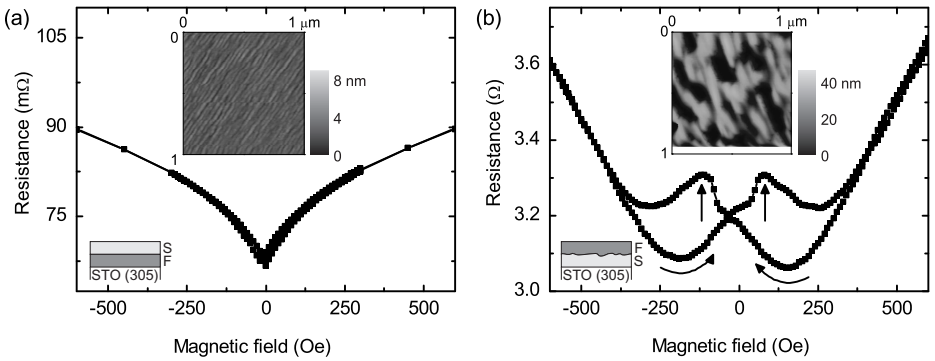

Figure 5.5: Resistance measurements at 61 K in the superconducting transition as a function of magnetic field on (a) an STO (305)/LSMO/YBCO bilayer (150/30 nm) and (b) an STO (305)/YBCO/LSMO bilayer (30/150 nm) measured in a current-in-plane configuration. The magnetic field is applied along the [010] easy axis. The sweep direction is indicated by arrows; the vertical arrows indicate the coercive field of the ferromagnetic layer. The inset in (a) shows an AFM image obtained on a 150 nm single LSMO film, which is much smoother than a 100 nm single YBCO film, as shown in (b).

200 Oe, the resistance starts following the parabolic dependence again, however now displaced over the horizontal axis by a value of approximately 350 Oe. Since there is only one ferromagnetic layer we cannot analyze our results in terms of the relative orientation of ferromagnetic layers ruling out the spin-switch effect as a cause of the observed shift. Similarly, explanations using spin imbalance or increased quasiparticle densities fail for bilayers, since in these models there is no dependence on the direction of the spins. In fact, the observation of hysteresis effects in bilayers strongly points at an influence of the magnetization direction of the layer and its relative direction to the applied magnetic field. One can think of the total magnetic field, given by the contributions of the applied field and the stray fields of the ferromagnetic layer, as the main parameter determining the resistance of the bilayer. The peak structure around the coercive field is then most likely caused by stray fields at domain walls, due to the reorientation of magnetic domains. The larger S/F surface roughness of the STO (305)/S/F compared to the STO (305)/F/S bilayer might be expected to increase stray field effects.[31] The larger hysteresis observed in the STO (305)/S/F structures confirms this picture, in agreement with Ref. 14.

5.3.2 Resistance switching in F/S/F trilayers

In addition to bilayers, we observe clear switching effects in trilayers. In Fig. 5.6, the magnetization curve of a (305)-oriented F/S/F trilayer together with the field dependence of the resistance of the trilayer is presented. The layer thicknesses are 50, 30, and 150 nm for the bottom F, S, and top F layers, respectively. The

T_c of the trilayer is 40 K and the measurement is performed at 44 K. When the bottom LSMO layer switches, the trilayer resistance shows a small downward deviation from the parabolic curve. A large resistance drop occurs upon switching the thicker and rougher top layer. If the resistance-switching effects resulted from switching from P to AP states, an *increase* in resistance of equal magnitude would be expected at the lowest coercive field. In addition, in the region around zero field, between the lowest positive and negative coercive fields, the system would be in the same P state and the curves measured in increasing magnetic field and decreasing field would have to overlap. The observed switching behavior thus cannot be attributed to switching from P to AP states, but rather arises from the switching of the individual layers. It is interesting that we can observe a small resistance change as a result of the switching of the smooth F bottom layer, while

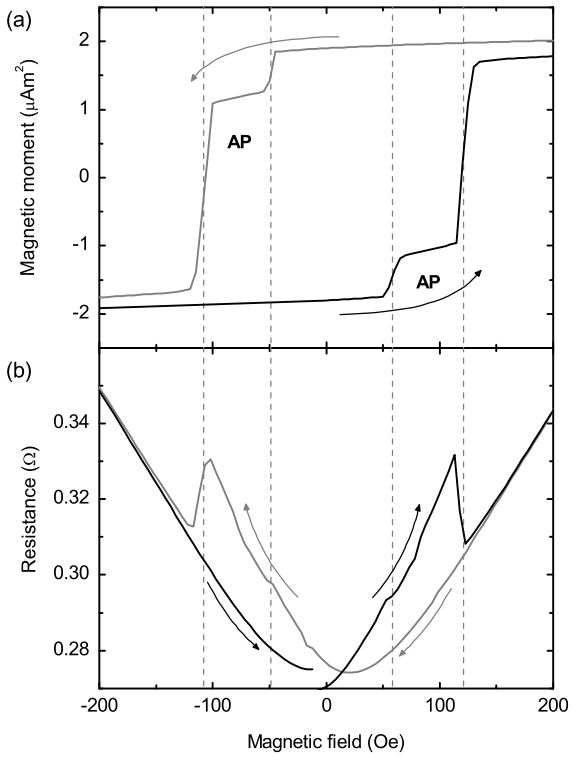

Figure 5.6: (a) Magnetization of a (305) F/S/F trilayer (50/30/150 nm) as measured with a VSM at 40 K. The dashed lines correspond to the coercive fields of the top and bottom layer. The highest coercive field is from the thicker top layer. The field range where the magnetization direction of the two layers is AP is indicated. (b) Magnetization-induced resistance-switching effects at the superconducting transition (44 K). The apparent discontinuity at zero field is due to a small and smooth temperature drift in the system. Arrows denote the field sweep direction.

we cannot see it in an STO (305)/F/S bilayer. Apparently, stray fields more easily penetrate the superconductor in trilayers than in bilayers. Similar behavior was recently observed in Ref. 14, where it was attributed to a magnetostatic coupling of the ferromagnetic layers.

Before discussing the data further in terms of stray fields, we would first like to discuss whether a superconducting spin-switch effect could be detectable in our system given the thickness of the superconductor being several times the coherence length of YBCO, which is about 2–3 nm in the *ab* plane. In the original picture by Tagirov,[2] the superconducting spin-switch effect depends on the parameter $(\xi_s/d_s)^2$, in which d_s is the thickness of the superconducting layer and $\xi_s = \sqrt{\hbar D_s/2\pi k_B T_c}$, D_s being the diffusion constant in the superconductor, and $\hbar$ and k_B being the Planck and the Boltzmann constants, respectively. The Ginzburg-Landau coherence length ξ_{GL} at 0 K is approximately equal to ξ_s: $\xi_s = 2\xi_{GL}(0)/\pi$.[32] Although the T_c shift due to the spin-switch effect could be numerically calculated explicitly, we can safely conclude from the small value of $(\xi_s/d_s)^2$ that it would be small. In Ref. 5, a magnetoresistance effect resulting from crossed Andreev reflection processes is predicted up to approximately ten times the coherence length. This approaches our film thicknesses, but it should be taken into account that the electrons traversing the superconductor on the *ab* planes will experience a film thickness of 60 nm due to the 31° angle of the planes with respect to the sample surface. On the other hand, if the (inverse) spin switch originates from the injection of spin-polarized electrons, the characteristic length scale is set by the spin-diffusion length in YBCO, which might well be larger than our film thickness.[19,33]

5.3.3 Penetrating field model

We have shown above that the resistance-switching effect in trilayers is larger when the top layer switches than when the bottom layer switches. The difference seems to be too large to arise solely from the different thicknesses of the top and

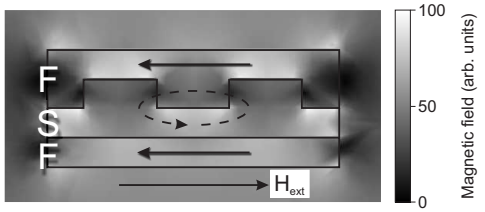

Figure 5.7: Simulated field distribution in an F/S/F trilayer with roughness. Arrows denote the field and magnetization directions. Roughness increases the field in the superconductor. At the thinnest parts of the superconductor, the stray fields (dashed line) are locally opposite to the magnetization direction. The situation as depicted exists when the system has been saturated in a strong negative field (pointing to the left), after which the field has been set to positive, but smaller than the lowest switching field.

bottom layer. We have already seen for the bilayers that roughness can increase the stray fields from the ferromagnetic layers. If the magnetization would be perfectly homogeneous and in plane, the field induced in the superconductor due to the magnetization of the F layers would be very small and in fact only nonzero due to the finite size of the layers. This is the reason that in bilayers switching effects are absent when the F layer is the smooth bottom layer. To substantiate the effects of roughness further, we have carried out finite element simulations on a trilayer with one rough and one smooth F layer. Indeed, a substantial field is predicted to be induced in the superconductor; see Fig. 5.7. In the simulation, we neglect screening effects in the superconductor, which in practice will be small, since the temperature is above T_c. The essential point is that in parts where the superconductor is thin (which contribute the most to the resistance), the induced field will be *opposite* to the magnetization of the layer, and can be either parallel or antiparallel to the applied field, depending on the preparation of the system. We can therefore write for the total field $B_{\rm tot}$ in the superconductor

$$B_{\rm tot} = \mu_0 \left(H_{\rm ext} - \alpha_1 M_1 - \alpha_2 M_2 \right), \tag{5.1}$$

where $H_{\rm ext}$ is the externally applied field and $\alpha_{1,2}$ are positive constants, relating the magnetization in the layers 1 and 2 to the induced field in the superconductor. It will be clear that α is larger for the rougher layer. Now we can combine this

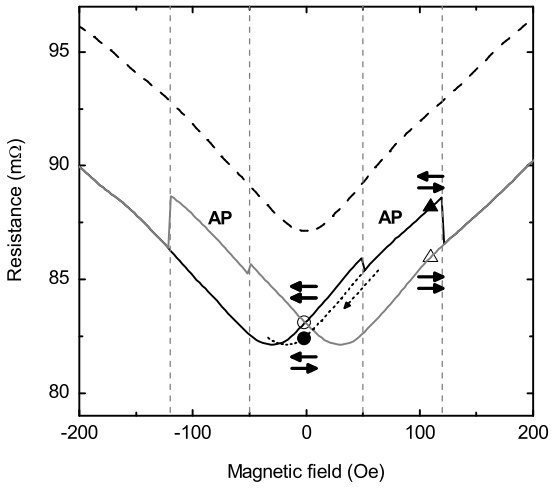

Figure 5.8: Reconstruction of the trilayer magnetic field dependence [solid black (grey) line for increasing (decreasing) magnetic field] starting from the field dependence of a single YBCO layer in the superconducting transition (dashed curve, arbitrary offset). The vertical dotted lines denote the coercive fields of the ferromagnetic layers. The open circle and triangle denote parallel states at different field values at which antiparallel states can be prepared as well (filled symbols). Horizontal arrows represent the magnetization state of the F layers; arrows to the right (left) indicate magnetization in the positive (negative) direction.

with the field dependence of YBCO in the absence of F layers, which is given in Fig. 5.8 by the dashed line. At a large positive field, the resistance will be lower than for the bare YBCO, due to the stray fields induced by the roughness, which are antiparallel to $H_{\rm ext}$. Upon lowering the field the curve goes through a minimum at positive $H_{\rm ext}$ because of the cancellation of external and stray fields. Further lowering yields a resistance increase because now the external and stray fields point in the same direction. At the coercive fields of the F layers 1 and 2, the curve then shifts down, because the magnetization and therefore the stray fields switch and become again antiparallel. The switching of the ferromagnetic layers leads thus to lateral shifts of the dashed curve at the coercive fields. If we take the coercive fields to be 50 and 120 Oe and use $\mu_0\alpha_1 M_1 = 5$ Oe and $\mu_0\alpha_2 M_2 = 25$ Oe, we get the curve represented by the solid line. This would correspond to values for $\alpha_{1,2}$ of 0.2 % and 1 %, respectively. In the light of the previously suggested superconducting spin-switch models, it is surprising that such a simple model can reproduce the observed behavior so well.

To further substantiate this result, we prepared the system to be in the states

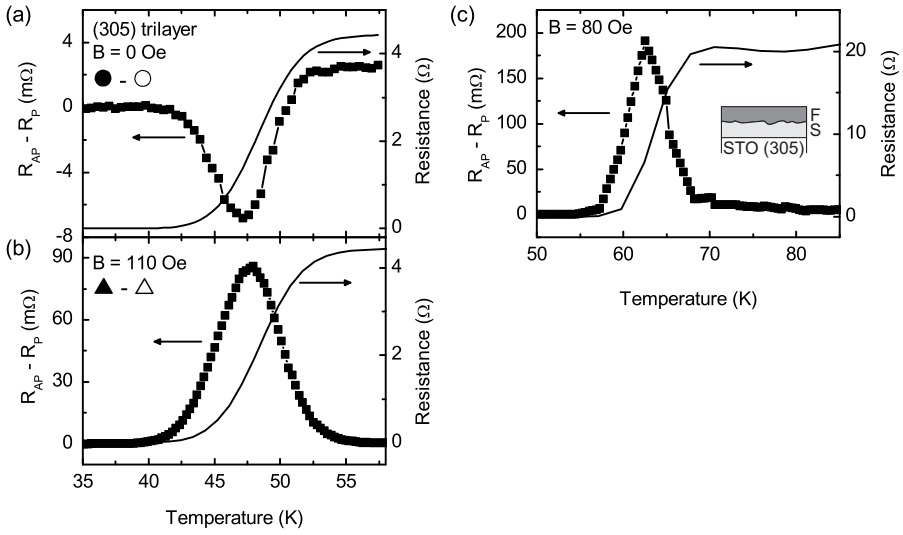

Figure 5.9: [(a) and (b)] Resistance differences (line and symbols) between antiparallel and parallel states for a (305)-oriented F/S/F trilayer (50/30/150 nm). The symbols correspond to the symbols used in Fig. 5.8. The temperature dependence of the resistance itself is indicated by the solid line (corresponding to the scale on the right). The resistance difference between the antiparallel state and the parallel state is opposite in sign and different in size for two different field values, which is difficult to account for within the spin-switch model but has a clear origin in the stray fields from the individual ferromagnetic layers, penetrating the superconductor. (c) In an S/F *bilayer* (30/150 nm), at a finite field value below the coercive field, the switching of the ferromagnetic layer yields a comparable signal, supporting the idea that stray fields play an important role in these structures.

as indicated by the circles and triangles in Fig. 5.8 and looked at the temperature dependence of the resistance difference between the open and filled symbols. Thus, we investigated the pure effect of the switching of the top or bottom layer on the resistance. It is clear from Fig. 5.9 that we only see resistance differences around the superconducting transition. This is due to the fact that the magnetoresistance of YBCO above T_c is small, and below T_c large fields are required to suppress superconductivity. Note that an increase in resistance could be interpreted as a decrease in T_c. At zero field, the difference between the AP and P states is small, which is due to the fact that it is the smooth bottom layer that is switched between the measurements. The signal is negative, which is clear from inspection of Fig. 5.8 since we are probing the difference between the filled and open circles. When we now compare this to the effect of switching the upper layer again parallel to the bottom layer, i.e., taking the difference between the open and filled triangles, we find a much larger signal of positive sign. It is interesting to see that we can mimic this behavior in a bilayer by measuring in a finite field (below the coercive field) with the magnetization AP and P with respect to the field. In Fig. 5.9(c) we find a resistance-switching effect that has similar sign and magnitude as found in the trilayer.

We have also studied the effect of inhomogeneous magnetization in the layers either by applying a demagnetization procedure or by applying fields perpendicular to the sample. We find in both cases an increase in the resistance, which we attribute to the increased contribution of magnetic stray fields as was also found for F/S/F triple layers with perpendicular magnetic anisotropy by Singh *et al.*.[34]

5.3.4 Switching in (001)-oriented F/S/F trilayers

We have also fabricated a (001)-oriented F/S/F trilayer, using the same layer thicknesses as were used for the (305) trilayer. The trilayer showed a T_c of 60 K. In Sec. 5.2.2, we have seen that for the (001)-oriented structures the magnetization switching is less well defined than for the (305)-oriented structures. Still, we observe resistance-switching effects near the coercive fields, indicated by dashed lines in Fig. 5.10. Our data on (001)-oriented structures are similar to data published in the literature.[18,19] Measurements are taken at 61 K. The resistance-switching effects are superimposed on a background dip which will be discussed below in Sec. 5.3.6. When the field is applied along the [010] direction, an increase in the resistance is observed between -200 and 200 Oe, in the regime where the hysteresis loop of the magnetization starts to open. Switching is not as sharp as in the case of the (305) trilayers, and we propose that the increase in the resistance here is due to non-homogeneous magnetization as a result of in-plane domain reorientation. Important to note is that at both switching fields the resistance appears to go down rather than up, again suggesting that for each layer the direction with respect to the applied field is more important than their relative orientations. When the field is applied along the [110] easy axis, the magnetization loop is sharper and domain-reorientation effects play less a role. The effect on the resistance is clear;

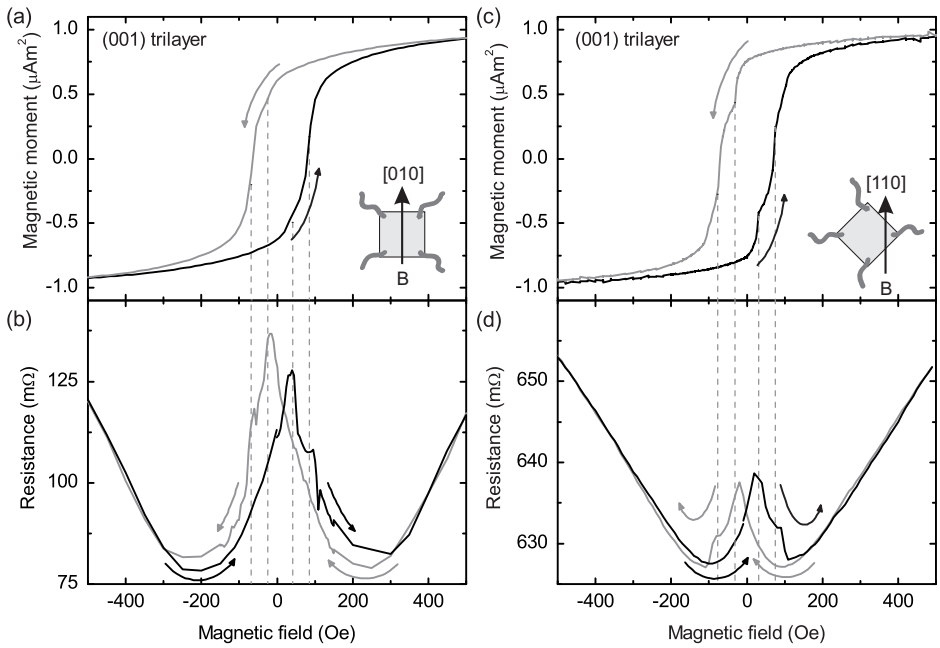

Figure 5.10: Magnetization [(a) and (c)] and resistance [(b) and (d)] measurements of a (001)-oriented F/S/F trilayer (50/30/150 nm) at 61 K in the superconducting transition for different magnetic field orientations as indicated. At the coercive field values, indicated by vertical dashed lines, resistance switching is observed. When the field is applied in the [010] direction, an increase in the resistance is observed between −200 and 200 Oe. This increase arises from in-plane domain-reorientation effects which correspond to the rounding of the magnetization curve. When the field is applied in the [110] easy direction the rounding decreases, resulting in a reduced resistance increase.

the increase in resistance between −200 and 200 Oe reduces dramatically. Notice that the smoother growth of YBCO on STO (001) diminishes the difference in roughness between the top and bottom layers and the roughness of both interfaces will be comparable to the bottom interface in the (305) structures. We can thus only explain the strong resistance change from domain effects, which certainly are present, as the magnetization loop is still rounded. This probably underlies dissimilarities between the data obtained on (305)- and (001)-oriented trilayers.

Let us now compare the relative magnitude of the resistance-switching effect for the (001) structures with that for the (305) structures. We adopt the definition $\Delta R = (R_{\max} - R_{\min})/R_{\mathrm{nor}}$,[14] in which $R_{\min}$ and $R_{\max}$ are the resistance minimum and the maximum induced by the switching and R_{nor} is the resistance of the trilayer in the normal state. We find $\Delta R = 0.7$ % for the (001) trilayer when the field is applied in the [010] direction and 0.2 % when applied in the [110] direction. For the (305) trilayer the individual contributions of both layers are clearly visible

and we find 0.4 % when the top layer is switched and we estimate 0.04 % for the bottom layer. We thus obtain that the magnitude of the resistance switching in the (305) structure is relatively large, given the sharp magnetization switching, which we attribute to the roughness of the corresponding interface. The much smoother bottom interface shows indeed a smaller switching effect than the (001)-oriented structures.

5.3.5 Switchable coupling of F layers

We have made another observation that indicates the importance of the magnetic field penetrating the superconductor in this particular kind of structures. In Fig. 5.11 we show magnetization loops of a (001)-oriented F/S/F trilayer both above T_c at 80 K and well below T_c at 25 K. Although, as stated above, structures with this orientation do not show single-domain magnetization-switching behavior, we can observe a steplike magnetization curve well above T_c, arising from two independent coercive fields. When the temperature is lowered to below T_c, this two-step behavior disappears and the coercive fields seem to merge. This behavior is likely due to the sudden change in screening behavior of the S layer. The interplay between magnetic domain structures and vortices were studied in Refs. 35–37. It is well known that superconductivity in S/F hybrid structures can modify the magnetization state.[38–40] While it is difficult here to identify exactly the mechanism leading to the observed coupling of the ferromagnetic layers through superconductivity, it is clear from the measurement that magnetic interactions

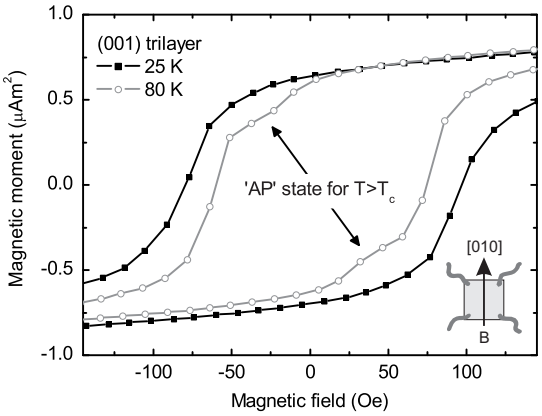

Figure 5.11: Upon decreasing the temperature below T_c of the superconductor in a (001) F/S/F trilayer (50/30/150 nm), we observe the loss of the "AP" state due to a change in the mutual influence of the layers. This observation provides further proof that the F layers feel each others' magnetic fields and, therefore, field effects on the superconductor cannot be neglected. AP is put between quotation marks here, since due to the biaxial magnetic anisotropy, it is questionable whether this state is truly antiparallel.

between the F layers through the superconductor take place, which stresses the importance of stray fields in these structures.

5.3.6 High-field behavior of the magnetoresistance

Finally we would like to discuss the high-field behavior of the F/S/F trilayers. In Ref. 18, peaks in the magnetoresistance, centered at zero field, were attributed to spin imbalance due to the injection of spin-polarized carriers in a fashion that resembles the GMR effect. In Fig. 5.12(a) the high-field dependence of a (305)-oriented trilayer at temperatures in the range from 34 to 51 K is displayed. We observe a dip, rather than a peak, which directly reflects the magnetic field dependence of the YBCO in the superconducting transition. Note that the switching effects that have been discussed in Secs. 5.3.1–5.3.5. take place at the bottom of the dip. In a (001)-oriented trilayer, however, we observe the crossover from a peak to a dip depending on the temperature; see Fig. 5.12(b). We propose a straightforward explanation for this crossover. Especially around T_c, small inho-

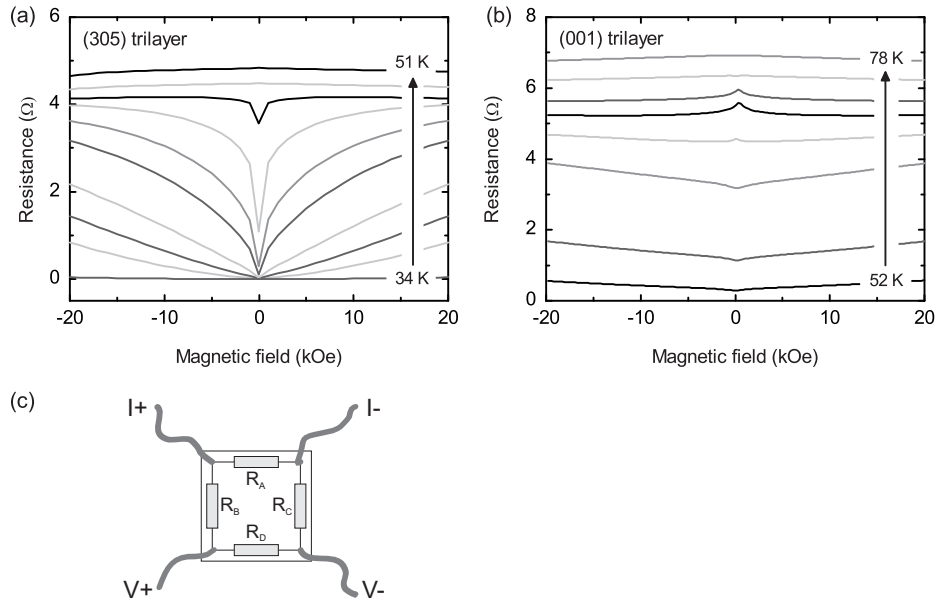

Figure 5.12: High-field magnetoresistance behavior for various temperatures from just below T_c to just above T_c for (a) (305)- and (b) (001)-oriented trilayers. In both trilayers, the bottom F, S, and top F layer are 50, 30, and 150 nm, respectively. In the (305) structure we find a dip, reflecting the magnetoresistance of the YBCO in the superconducting transition. The (001) structures show a crossover from a peak to a dip centered around zero field. (c) Resistor network representing a simplified scheme of the sample resistance. When R_B and R_C decrease the measured resistance increases. This effect might explain the peak-to-dip crossover observed in (b).

mogeneities in the film can lead to large resistance variations over the sample. For example, a small variation in T_c over the sample can lead to a considerable resistance variation over the sample. With the help of a simplified resistor network in Fig. 5.12c it is easy to see that when a current I_{tot} is passed through the current contacts I^+ and I^-, the voltage over the voltage contacts (V_D) will be given by $I_{tot}R_AR_D/(R_A + R_B + R_C + R_D)$. This means that when the resistances R_B and R_C *decrease*, the resistance we measure (i.e., V_D/I_{tot}) *increases*. Indeed, in (305)-oriented trilayers, where superconducting paths are achieved at higher temperatures in the [010] direction than in the [50$\bar{3}$] direction, the superconducting transition in one direction is sometimes accompanied by a resistance increase in the other direction. In Fig. 5.3 a weak signature of this effect can be seen. In a similar way, if a superconducting path is achieved in the direction perpendicular to the one in which the measurement is performed [in Fig. 5.12(c), for example, R_B], this will generate a magnetoresistance with a dip, which now appears as a peak in the actual measurement. For lower temperatures, the dip in the initial superconducting path becomes weaker, but a direct superconducting connection between the voltage contacts will appear, resulting in the recovery of a dip.

5.4 Conclusion

We have searched for the superconducting spin-switch effect in F/S/F LSMO/YBCO bi- and trilayers that were optimized for the effect by making the contact between the materials partly in YBCO's crystallographic *ab* plane. Although we find sharp magnetization-switching behavior in these structures, with a well-defined antiparallel state, we do not observe any signature of a spin-switch effect. Instead, our data provide compelling evidence that the observed resistance-switching effects are caused by magnetic stray fields from the ferromagnetic layers, and that also interface roughness can play a role in the observed effects. In the case of the sharply switching (305)-oriented structures, we find that we can explain the data by taking such roughness into account explicitly. In (001)-oriented structures, we have shown that domain reorientation effects have a strong contribution. Moreover, the same description allows explanation of data taken on bilayers with either rough or smooth interfaces. The results may be a warning sign that magnetic field effects, although often not considered to play a role in this kind of structures, might be important after all.

References

[1] M. van Zalk, M. Veldhorst, A. Brinkman, J. Aarts, and H. Hilgenkamp, Phys. Rev. B **79**, 134509 (2009).

[2] L. R. Tagirov, Phys. Rev. Lett. **83**, 2058 (1999).

[3] A. I. Buzdin, A. V. Vedyayev, and N. V. Ryzhanova, Europhys. Lett. **48**, 686 (1999).

[4] P. G. De Gennes, Phys. Lett. **23**, 10 (1966).

[5] F. Giazotto, F. Taddei, F. Beltram, and R. Fazio, Phys. Rev. Lett. **97**, 087001 (2006).

[6] J. Y. Gu, C. Y. You, J. S. Jiang, J. Pearson, Y. B. Bazaliy, and S. D. Bader, Phys. Rev. Lett. **89**, 267001 (2002).

[7] A. Potenza and C. H. Marrows, Phys. Rev. B **71**, 180503(R) (2005).

[8] A. Y. Rusanov, S. Habraken, and J. Aarts, Phys. Rev. B **73**, 060505(R) (2006).

[9] I. C. Moraru, W. P. Pratt, Jr., and N. O. Birge, Phys. Rev. Lett. **96**, 037004 (2006).

[10] I. C. Moraru, W. P. Pratt, Jr., and N. O. Birge, Phys. Rev. B **74**, 220507(R) (2006).

[11] D. Stamopoulos, E. Manios, and M. Pissas, Phys. Rev. B **75**, 014501 (2007).

[12] G. X. Miao, K. S. Yoon, T. S. Santos, and J. S. Moodera, Phys. Rev. Lett. **98**, 267001 (2007).

[13] R. Steiner and P. Ziemann, Phys. Rev. B **74**, 094504 (2006).

[14] D. Stamopoulos, E. Manios, and M. Pissas, Phys. Rev. B **75**, 184504 (2007).

[15] D. Stamopoulos, E. Manios, and M. Pissas, Supercond. Sci. Technol. **20**, 1205 (2007).

[16] G. Carapella, F. Russo, and G. Costabile, Phys. Rev. B **78**, 104529 (2008).

[17] J. H. Park, E. Vescovo, H. J. Kim, C. Kwon, R. Ramesh, and T. Venkatesan, Nature **392**, 794 (1998).

[18] V. Peña, Z. Sefrioui, D. Arias, C. Leon, J. Santamaria, J. L. Martinez, S. G. E. te Velthuis, and A. Hoffmann, Phys. Rev. Lett. **94**, 057002 (2005).

[19] N. M. Nemes, M. García-Hernández, S. G. E. te Velthuis, A. Hoffmann, C. Visani, J. Garcia-Barriocanal, V. Peña, D. Arias, Z. Sefrioui, C. Leon, et al., Phys. Rev. B **78**, 094515 (2008).

[20] C. Visani, V. Peña, J. Garcia-Barriocanal, D. Arias, Z. Sefrioui, C. Leon, J. Santamaria, N. M. Nemes, M. Garcia-Hernandez, J. L. Martinez, et al., Phys. Rev. B **75**, 054501 (2007).

[21] Y. Gim, A. W. Kleinsasser, and J. B. Barner, J. Appl. Phys. **90**, 4063 (2001).

[22] X. Deng, M. Joshi, R. Chakalova, M. S. Colclough, R. Palai, Y. Y. Tse, I. P. Jones, H. Huhtinen, and C. M. Muirhead, Phys. Rev. B **77**, 144528 (2008).

[23] Z. Yang, M. Lange, A. Volodin, R. Szymczak, and V. V. Moshchalkov, Nat. Mater. **3**, 793 (2004).

[24] C. Bell, S. Turşucu, and J. Aarts, Phys. Rev. B **74**, 214520 (2006).

[25] S. Mandal, R. C. Budhani, J. He, and Y. Zhu, Phys. Rev. B **78**, 094502 (2008).

[26] W. A. M. Aarnink, E. Reuvekamp, M. A. J. Verhoeven, M. V. Pedyash, G. J. Gerritsma, A. van Silfhout, H. Rogalla, and T. W. Ryan, Appl. Phys. Lett. **61**, 607 (1992).

[27] G. Koster, B. L. Kropman, G. J. H. M. Rijnders, D. H. A. Blank, and H. Rogalla, Appl. Phys. Lett. **73**, 2920 (1998).

[28] M. Mathews, F. Postma, J. Lodder, R. Jansen, G. Rijnders, and D. Blank, Appl. Phys. Lett. **87**, 242507 (2005).

[29] Y. Suzuki, H. Y. Hwang, S. W. Cheong, and R. B. van Dover, Appl. Phys. Lett. **71**, 140 (1997).

[30] E. C. Stoner and E. P. Wohlfarth, Philos. Trans. R. Soc. London, Ser. A **240**, 599 (1948), reprinted in IEEE Trans. Magn. **27**, 3475 (1991).

[31] B. D. Schrag, A. Anguelouch, S. Ingvarsson, G. Xiao, Y. Lu, P. L. Trouilloud, A. Gupta, R. A. Wanner, W. J. Gallagher, P. M. Rice, et al., Appl. Phys. Lett. **77**, 2373 (2000).

[32] Z. Radović, L. Dobrosavljević-Grujić, A. I. Buzdin, and J. R. Clem, Phys. Rev. B **38**, 2388 (1988).

[33] S. Soltan, J. Albrecht, and H.-U. Habermeier, Phys. Rev. B **70**, 144517 (2004).

[34] A. Singh, C. Sürgers, M. Uhlarz, S. Singh, and H. von Löhneysen, Appl. Phys. A **89**, 593 (2007).

[35] F. Laviano, L. Gozzelino, E. Mezzetti, P. Przyslupski, A. Tsarev, and A. Wisniewski, Appl. Phys. Lett. **86**, 152501 (2005).

[36] F. Laviano, L. Gozzelino, R. Gerbaldo, G. Ghigo, E. Mezzetti, P. Przyslupski, A. Tsarou, and A. Wisniewski, Phys. Rev. B **76**, 214501 (2007).

[37] L. Gozzelino, F. Laviano, P. Przyslupski, A. Tsarou, A. Wisniewski, D. Botta, R. Gerbaldo, and G. Ghigo, Supercond. Sci. Technol. **19**, S50 (2006).

[38] C. Monton, F. de la Cruz, and J. Guimpel, Phys. Rev. B **75**, 064508 (2007).

[39] H.-Y. Wu, J. Ni, J.-W. Cai, Z.-H. Cheng, and Y. Sun, Phys. Rev. B **76**, 024416 (2007).

[40] C. Monton, F. de la Cruz, and J. Guimpel, Phys. Rev. B **77**, 104521 (2008).

Chapter 6 Large negative magnetoresistance and magnetoresistance oscillations at the $LaAlO_3/SrTiO_3$ interface

Abstract

A high magnetic field (up to 30 T) low-temperature (50 mK–4.2 K) transport study was performed of the quasi-two-dimensional electron gas at the $LaAlO_3/SrTiO_3$ interface. Samples were fabricated using a relatively high oxygen deposition pressure, and featured non-monotonous resistance-versus-temperature behavior, with a minimum around 70 K. It was shown that the electron gas at these interfaces shows a large, negative and magnetic-field-orientation independent magnetoresistance, which is attributed to spin scattering off localized magnetic moments. Magnetoresistance oscillations of unknown origin have been observed.

6.1 Introduction

The recent discovery of interface conductivity in stackings of the insulators $LaAlO_3$ (LAO) and $SrTiO_3$ (STO) by Ohtomo and Hwang[1] has attracted a lot of attention. Two-dimensional electron gases (2DEGs) in semiconductor heterostructures have become workhorses for the semiconductor industry and solid-state research. The high electron mobilities that can be achieved in 2DEGs have resulted in discoveries as for instance the quantum Hall effect (QHE).[2] Such two-dimensional (2D) behavior, in combination with the rich physics shown by the oxides with their complex phase diagrams, could possibly lead to novel phenomena and applications. A number of experiments indicate that the conducting layer at the LAO/STO system is confined to within a few nm from the interface.[1,3–8] But what is the ground state of the interface electron gas? And would it be possible to observe quantum Hall behavior at the LAO/STO interface? In search for answers to these questions, we have explored the high-field magnetotransport properties in the sub-K temperature regime.

6.1.1 Properties of LAO/STO interfaces

LAO/STO interfaces are characterized by a number of remarkable features. First of all, the interface behavior depends strongly on the stacking sequence of atomic layers. LAO and STO are both perovskites, which can be considered as alternating stacks of $(SrO)^0$ and $(TiO_2)^0$ for STO and stacks of $(LaO)^+$ and $(AlO_2)^-$ for LAO; see Fig. 6.1(a) and (b). The superscripts denote the charge of these layers, obtained from the formal valence state counting of the constituents, i.e., within the purely ionic limit. The interface can then be constructed in two different ways: the $(TiO_2)^0/(LaO)^+$ interface arises from deposition of LAO on a TiO_2-terminated STO substrate, while the $(SrO)^0/(AlO_2)^-$ interface can be created by first depositing a monolayer of SrO on such a substrate, followed by the deposition of LAO. It turns out that while the $(TiO_2)^0/(LaO)^+$ interface is conducting, the $(SrO)^0/(AlO_2)^-$ is insulating.[1] The LAO thickness plays a crucial role for the conductivity of the $(TiO_2)^0/(LaO)^+$ interface. It was shown that the conductivity shows an abrupt onset when a critical thickness of 4 unit cells is exceeded.[4] In STO/LAO/STO and LAO/STO/LAO heterostructures the coupling of the complementary $(SrO)^0/(AlO_2)^-$ and $(TiO_2)^0/(LaO)^+$ interfaces was reported when brought together less than 6 unit cells, leading to a decrease of interface conductivity.[3]

The interface behavior is sensitive to the oxygen pressure during growth. We can identify three pressure regimes, as indicated in Fig. 6.1(c). The low pressure regime ($pO_2 < 10^{-5}$ mbar) is characterized by a dominant contribution of oxygen vacancies and the conducting layer has a three-dimensional character.[9–11] In the intermediate regime ($10^{-5} \leq pO_2 < 10^{-3}$ mbar), the interfaces exhibit superconductivity below 200 mK.[6] The superconducting layer is confined to a sheet of about 10 nm thickness. For higher oxygen pressures ($pO_2 \geq 10^{-3}$ mbar), the interfaces are characterized by an upturn in resistance below 70 K for decreasing temperatures and a large negative magnetoresistance.[12] These interfaces will be studied in this chapter. We will argue that the magnetoresistance is due to spin scattering. It was recently reported that it is possible to tune the interface between the states corresponding to the intermediate pressure and the high pressure regime by applying an electric field.[13] This suggests that it is the charge carrier density at the interface that determines its behavior, although a recent study points out the possibility of modulation of the carrier mobility by electric field.[14]

6.1.2 Mechanisms for interface conductivity

An appealing explanation for the LAO/STO interface conductivity is the mechanism of electronic reconstruction.[1,15,16] It is the electronic counterpart of a structural reconstruction[17] that can occur for a polar/non-polar interface as a result of a potential buildup in the polar material. The potential buildup arises from the stacking of positively and negatively charged atomic layers. The potential grows while increasing the layer thickness of the polar material. When a critical thickness

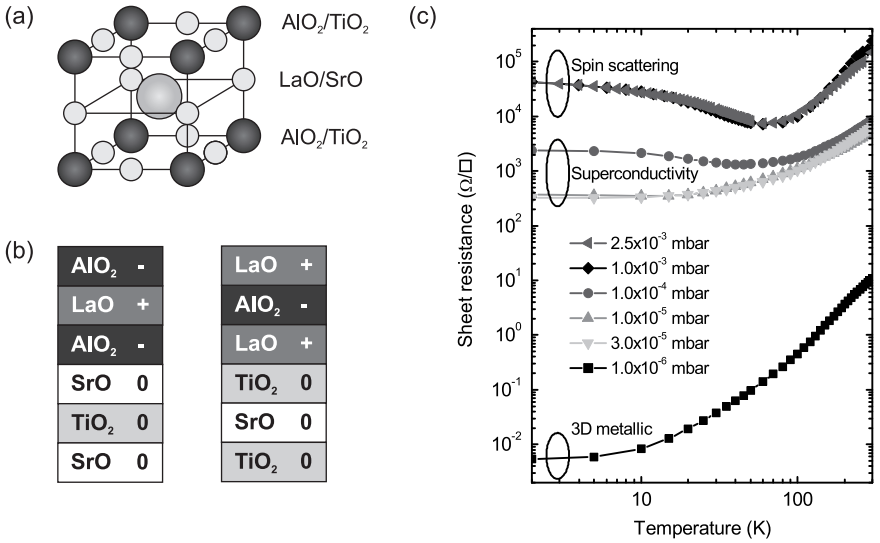

Figure 6.1: (a) General perovskite crystal structure consisting of layers of LaO and AlO_2 for $LaAlO_3$ and layers of SrO and TiO_2 for $SrTiO_3$. (b) Sketch of the two possible ways to construct the $LaAlO_3/SrTiO_3$ interface. The layer charge in the purely ionic limit is indicated. The structure on the right is the one studied in this chapter. (c) The temperature dependence of the interface resistance depends on the oxygen deposition pressure during growth. In order to minimize the possible influence of oxygen vacancies, we have studied the samples grown at the highest oxygen pressures of 1×10^{-3} and 2.5×10^{-3} mbar.

is exceeded, a reconstruction occurs, to counteract the diverging electric potential. If the reconstruction takes place by transferring charge to the otherwise uncharged layer of the non-polar material, it can be called an electronic reconstruction. In the specific case of the $(TiO_2)^0/(LaO)^+$ interface, it is proposed that half an electron per unit cell is transferred to the uncharged TiO_2 terminating layer of the STO.[1] It is therefore also called the n-type interface. The transferred electrons will enter the Ti $3d$ conduction band, where they give rise to conduction. In addition, when the amount of carriers reaches 0.5 electron per unit cell, it is theoretically proposed that charge and spin ordering might occur.[18]

An alternative picture can explain many observations for the LAO/STO interface, namely the presence of oxygen vacancies in the STO.[9–11] It is well known that oxygen vacancies can be induced in STO by reducing the material at high temperature in a low oxygen pressure environment.[19] The oxygen vacancies are highly mobile at high temperatures and turn the material from insulating to conducting. The oxygen deposition pressure dependence of the LAO/STO interface properties as shown in Fig. 6.1(c) strongly suggests a crucial role of oxygen vacancies for these interfaces too. Moreover, the interfaces share many properties with reduced STO crystals including superconductivity below 300 mK, high electron mobility, a large ratio between room temperature resistivity and low-temperature resistivity

and a positive parabolic magnetoresistance. We have chosen to study samples grown at high oxygen deposition pressure ($\geq 10^{-3}$ mbar), in order to diminish the influence of oxygen vacancies and promote the confinement of the electron gas at the interface. The sheet carrier density of our samples as determined at 20 K is about 10^{13} cm^{-2}.

In addition to electronic reconstruction and oxygen vacancies, structural deformations and cation disorder were also shown to play a role at the LAO/STO interface.[16,20,21] It is possible that structural reconstructions, such as distortions of the oxygen octahedra, occur in conjunction with electronic reconstruction.[22,23]

6.1.3 Feasibility of the QHE at the LAO/STO interface

The electron gas at the LAO/STO interface is confined to within a few nanometer from the interface.[1,3–7] Yet, it is generally not referred to as a 2DEG, but rather as a quasi-2DEG. In this section, we will specify the difference and assess the feasibility for observing 2D behavior at LAO/STO interfaces.

In semiconductor heterostructures, electrons can be trapped in a narrow well arising from band bending at certain interfaces, like for instance the GaAs/AlGaAs interface. The confinement of the electron gas gives rise to separate energy levels, at which electronic subbands exist that describe the transport along the interface. The 2DEG is now characterized by the population of only a single subband.

When a magnetic field is applied, the electronic states are further quantized by the formation of Landau states, which arise from the circular motion of electrons in magnetic fields. The electron wave function becomes localized around some point, and the continuity of the wave function imposes quantization. The Landau energy levels shift linearly to higher energy for increasing magnetic fields, and one by one cross the Fermi energy. The crossing gives rise to a resistance maximum and as a result, H^{-1} spaced maxima appear in the longitudinal magnetoresistance in magnetic field. This is the Shubnikov-de Haas effect. Concomitantly, quantum Hall steps appear in the Hall resistance. A necessary condition for the formation of Landau levels is that the time needed for the electron wave to traverse the circular orbit (ω_c^{-1}, being the inverse of the cyclotron frequency) is smaller than the elastic scattering time τ, i.e., $\omega_c\tau \gg 1$. This condition is equivalent to $\mu\,\mu_0 H \gg 1$, with μ the electron mobility.

The question rises whether this condition can be fulfilled for our LAO/STO interfaces grown at high oxygen deposition pressure. These exhibit a high resistance and a mobility of the order of 10 cm^2/Vs. However, the resistance in these samples was found to be anisotropic and the anisotropy could be related to the step edge orientation of the STO substrate (in a way that resemble the anisotropy measurements of Chapter 2). Resistance contributions from the step edges might arise from the discontinuity of the interface across these step edges, acting as a scatter center or tunnel barrier. In addition, the resistance might arise from residual insulating SrO terminated regions between the TiO_2-terminated terraces, which are too narrow to be observed by atomic force microscopy. For a series of

randomly oriented measurement structures, a resistance ratio of 10 was measured for two orthogonal directions, which sets a minimum for the resistance ratio when measured exactly perpendicular to, and along step edges. The step-edge induced anisotropy in itself is a nice argument for quasi-2D behavior of the LAO/STO interfaces. It also opens up the possibility that the microscopic mobility, i.e., when measured between the step-edges, is much higher than the macroscopic mobility, as measured for a 5×5 mm^2 sample. By this argument, it might be possible to observe signatures of the QHE at high-pressure grown LAO/STO interfaces.

6.2 Experimental details

To realize the LAO/STO interfaces, we used STO (001) substrates that were TiO_2-terminated by a buffered-HF and annealing treatment.[24] Atomically smooth surfaces with clear unit-cell-height steps were observed with atomic force microscopy. On top of that, LAO films were grown at 850 °C in pO_2 of 1.0×10^{-3} or 2.5×10^{-3} mbar by pulsed laser deposition using a single-crystal LAO target. The growth was monitored by *in situ* reflective high-energy electron diffraction (RHEED).[25] The observed intensity oscillations clearly indicated a layer-by-layer growth mode with a very smooth surface and without any island growth. The thickness of the LAO layers was 26 unit cells, approximately 10 nm, as determined from the RHEED oscillations. After growth, the samples were cooled to room temperature in oxygen at the deposition pressure. Smooth surface morphology and the correct crystal structure of the final sample were confirmed by atomic force microscopy and x-ray diffraction.

Unstructured samples were wire-bonded to the corners, allowing us to contact the interface and measure the transport properties. Some samples were structured into a Hall-bar geometry. The structures were defined by argon ion etching, while keeping the etched surface insulating by optimizing the etch time and a short anneal in oxygen. These samples were electrically connected by wire-bonding to Au contact pads.

Measurements were conducted at the High Field Magnet Laboratory in Nijmegen in magnetic fields up to 30 T either in a ^{3}He cryostat or in a dilution refrigerator with a base temperature of 40 mK. Resistance measurements were performed using a standard low-frequency lock-in technique and high-impedance preamplifiers. Heating effects due to the measurement currents were excluded by using a measurement current of less than 5 nA, well within the range where the resistance was current-independent.

6.3 Sub-Kelvin high-magnetic-field transport measurements on LAO/STO interfaces

The low-temperature high magnetic field measurements of the LAO/STO interface grown at 1.0×10^{-3} mbar are characterized by three different phenomena:[12] (1) large, negative magnetoresistance, (2) (time-dependent) hysteresis and (3) oscillatory behavior. Because it is currently not completely sure whether the origin of the hysteresis is intrinsic to the LAO/STO interface or not, we leave the hysteresis out of consideration in the discussion of the magnetoresistance. We therefore first focus only on the magnetic field downsweeps, i.e., the magnetoresistance recorded in magnetic field decreasing to zero from a finite field value. The magnetic field downsweep coincides with the upsweep in the limit of infinitely low upsweep rate. Since the oscillatory behavior and the hysteresis are to a certain extent interrelated, we will present both up- and downsweeps in this discussion.

6.3.1 Magnetoresistance

The magnetoresistance, $[R(H) - R(0)]/R(0)$, in perpendicular magnetic field H of an LAO/STO interface grown at 1×10^{-3} mbar is shown in Fig. 6.2. At 50 mK, the magnetoresistance exceeds -50 % at 30 T. At 300 mK, the sample was *in situ* rotated in magnetic field, from which it was found that the magnetoresistance is independent of the orientation of the applied magnetic field. Experiments at 50 mK were performed with the applied field perpendicular to the sample surface and under an angle of 30° with respect to the surface. The magnetoresistance was larger (63 %) for the 30° orientation than for the perpendicular orientation (43 %). If the magnetoresistance would be determined by only the perpendicular component of the applied field, the magnetoresistance is expected to be *smaller* for the 30° orientation. Instead of being a field-orientation effect, the increased magnetoresistance for the 30° orientation was attributed to the observed increased resistance of the interface (at zero field) from 32 kΩ to 80 kΩ in the one month timelap between these experiments.

The magnetic field orientation independence of the magnetoresistance rules out any orbital explanations of the magnetoresistance including 2D weak localization as was suggested in Ref. 13. Weak localization in three dimensions is ruled out because the characteristic magnetic field dependence and power-law temperature dependence[26] are not shown by our data. Moreover, magnetoresistance effects due to weak localization are typically much smaller (< 1 %) (Ref. 27) than what is observed (> 50 %) for the LAO/STO interface.

Although magnetoresistance arising from magnetic order often is anisotropic, whereas the magnetoresistance of the high-pressure grown LAO/STO interfaces is independent of magnetic field orientation, it is worthwhile discussing the possibility of magnetic ordering in these interfaces. One of the key parameters in this respect is the fraction of occupied Ti 3*d* sites. The carrier density determined from

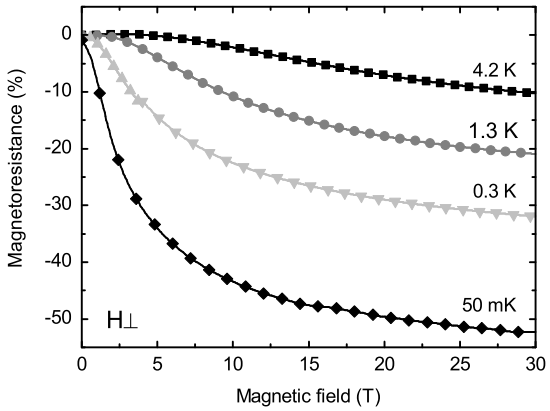

Figure 6.2: The magnetoresistance in perpendicular magnetic field for the LAO/STO interface grown at 10^{-3} mbar at several temperatures. The negative magnetoresistance exceeds -50 % at 50 mK.

transport measurements is about 10^{13} cm^{-2}, which is equivalent to 0.015 electrons per unit cell area. This is far below the nominal value of 0.5 electrons per unit cell that is expected from the electronic reconstruction scenario. It can be shown that this nominal value is only expected for infinitely thick LAO layers.[28] Of importance is also whether the electrons are localized or itinerant. X-ray photoelectron spectroscopy, which is sensitive to both localized and mobile electrons, measures a larger fraction of occupied Ti 3*d* sites than transport measurements.[7] This implies that part of the electrons is localized and a part is mobile, the latter giving rise to transport. Recent optical studies[29,30] and a theoretical study[31] substantiate this scenario. Interestingly, the x-ray photoelectron experiment also detects a fraction of Ti sites occupied for a 2 unit cell LAO sample, which is insulating for transport. The coexistence of localized and mobile electrons in the Ti 3*d* band is therefore plausible.

The itinerant carriers could induce ferromagnetic ordering of the local moments when coupled either ferromagnetically or antiferromagnetically to them. Antiferromagnetic ordering in a random distribution of local moments is not possible, although the RKKY (Refs. 32,33) exchange interaction, mediated by conduction electrons and oscillating in sign in real space, can give rise to a spin-glass state.[34]

If not ordered, local moments will still give rise to scattering. The best-known example is the Kondo system,[35] a dilute magnetic alloy in which conduction electrons scatter off localized magnetic moments. Typical Kondo systems are metals like Au or Cu doped with magnetic impurities such as Mn or Fe. Local moments arise from an unpaired spin in the atomic-like (localized) *d* or *f* shell of the impurity in the metallic host. In the Kondo problem, the localized moments are assumed isolated, i.e., indirect exchange interactions between the impurities via the conduction electrons are neglected. Therefore, Kondo systems contain few

magnetic impurities, typically of the order of 100 parts-per-million (ppm). Note that this concentration would translate to about 0.2 % for two dimensions, when the average nearest neighbor distance is kept constant. Kondo behavior in non-dilute magnetic impurity alloys occurs when inter-impurity interactions are small, for example in the heavy-fermion systems.[36]

The Kondo effect is characterized by a logarithmically increasing resistance for decreasing temperatures. In combination with T^2 and T^5 temperature dependences that are common for electron-electron and electron-phonon scattering, this gives rise to a resistance minimum as a function of temperature. The resistance minimum observed in Fig. 6.1 could be an indication for Kondo behavior in the LAO/STO interfaces. Indeed the upturn in resistance below 70 K is logarithmic

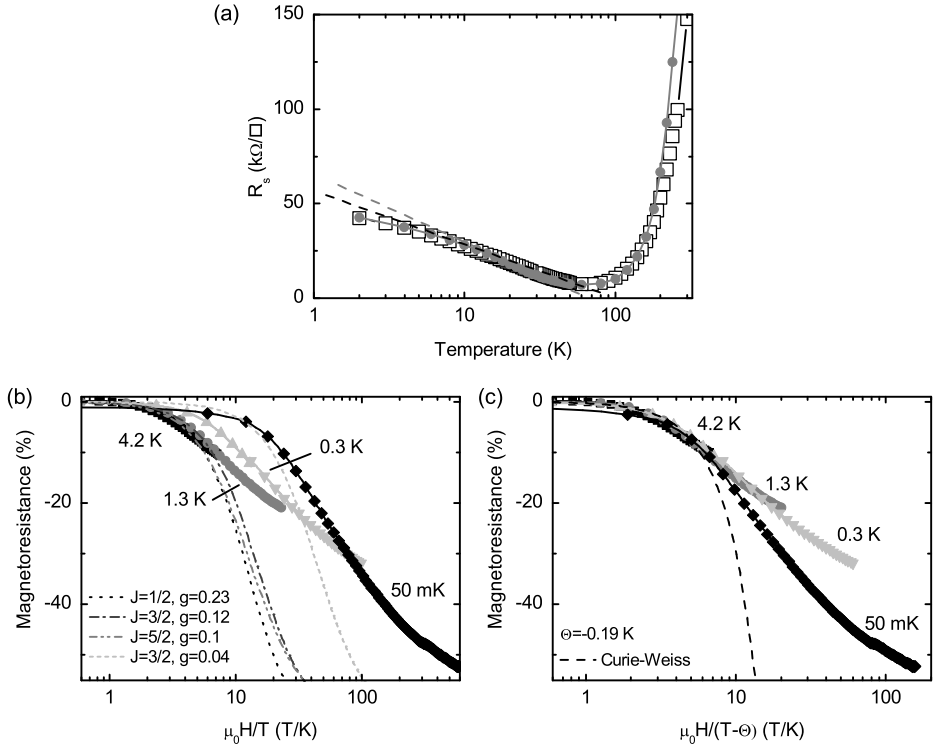

Figure 6.3: (a) The sheet resistances of the $pO_2 = 1 \times 10^{-3}$ mbar (filled circles) and 2.5×10^{-3} mbar (open squares) LAO/STO interfaces show a logarithmic temperature dependence at low temperatures, as indicated by the dashed lines. (b) The negative magnetoresistance as function of $\mu_0 H/T$. Broken lines would be expected for a magnetoresistance proportional to M^2, with the magnetization M following the Brillouin function with the total angular momentum quantum number J and the Landé factor g as fit parameters. (c) The negative magnetoresistance as function of $\mu_0 H/(T - \Theta)$, with a negative Weiss temperature $\Theta = -0.19$ K. The dashed line is a fit for M following the Curie-Weiss law.

over one decade (5–50 K) as demonstrated in Fig. 6.3(a).

Kondo systems display a fair (−15 % at 1.5 K, in a field of 2 T) amount of magnetoresistance, which is isotropic and negative in sign.[37] The negative magnetoresistance results from the alignment of the localized magnetic moments by magnetic field and therefore scales with the magnetization due to the local moments M and often shows M^2 dependence.[37,38] For paramagnetic impurities, M only depends on H/T, and is for small fields linear with the applied field (Curie's law) and for large fields given by the Brillouin function.[39] In Fig. 6.3(b) we plotted the negative magnetoresistance as function of H/T. The magnetoresistance curves for 4.2 and 1.3 K coincide. For 300 and 50 mK the low-field part deviates, but the curves concur for higher fields. We tried to fit the magnetoresistance curve by using the Brillouin function[39] $B_J(gJ\mu_B\mu_0 H/k_B T)$ for the calculation of M for different values of the total angular momentum quantum number J (μ_B is the Bohr magneton, g the Landé factor and k_B the Boltzmann constant). For free ions, the Landé factor follows from the angular momentum quantum numbers,[39] but for a reasonable fit, we had to decrease the calculated value by a factor of 0.04–0.1 [Note that the Landé factor for GaAs is reduced to −0.44 (Ref. 40)]. Fits for several values of J are included in Fig. 6.3(c). The Brillouin fits overestimate the magnetoresistance for high fields. In Fig. 6.3(c) we introduced a negative Weiss temperature of −0.19 K and now all curves coincide for low magnetic fields. A Curie-Weiss dependence is followed there as indicated by the dashed curve which represents $M^2 \propto [H/(T-\Theta)]^2$. A negative Curie-Weiss temperature Θ would be indicative for antiferromagnetic ordering (with a Néel temperature $T_N = -\Theta$), and Curie-Weiss behavior can in fact only be expected for $T > |\Theta|$. It is clear from these fitting attempts that the full details of the origin of the magnetoresistance are unclear. Either the proportionality between the magnetoresistance and M^2 does not hold over the complete temperature and magnetic field range, or M deviates from ideal paramagnetic behavior. Nevertheless, it seems not unreasonable to attribute the observed magnetoresistance at the LAO/STO interface to spin scattering off localized magnetic moments. The observed logarithmic increase of the resistance for decreasing temperature could then be related to the Kondo effect.

6.3.2 Magnetoresistance oscillations

At the lowest temperature of 50 mK, oscillations were observed in the magnetoresistance of the unstructured 5×5 mm^2 sample. In perpendicular fields, a weak oscillating signal was observed superposed on a background magnetoresistance curve. The oscillations were present both in the magnetic field upsweep and in the downsweep. In Fig. 6.4(a) the downsweep is presented. The background was fitted with the smooth function $-98 + 92(\mu_0 H)^{-0.23}$, which was subtracted from the signal leaving the resistance variation around the background as shown in Fig. 6.4(b). A few oscillations were resolved this way, with the minimum and maximum positions indicated in the figure.

The oscillations were also observed when the magnetic field was applied under

a 30° angle with respect to the sample surface. As was mentioned before, the resistance measurements at low temperature show a time-dependent hysteresis loop around zero magnetic field. When the magnetic field sweep rate was increased from 33.3 mT s^{-1}, it was found that the hysteresis loop opened up further. Although this hysteretic behavior might be not intrinsic to the LAO/STO interface, we find that it enhances the magnetoresistance oscillations that are weakly present in the magnetic field downsweep [Fig. 6.4(c)]. For the downsweep, we have no indications that heating effects, or other extrinsic phenomena influence the data. In Fig. 6.4(d), the upsweeps are plotted against the square root of the magnetic field.

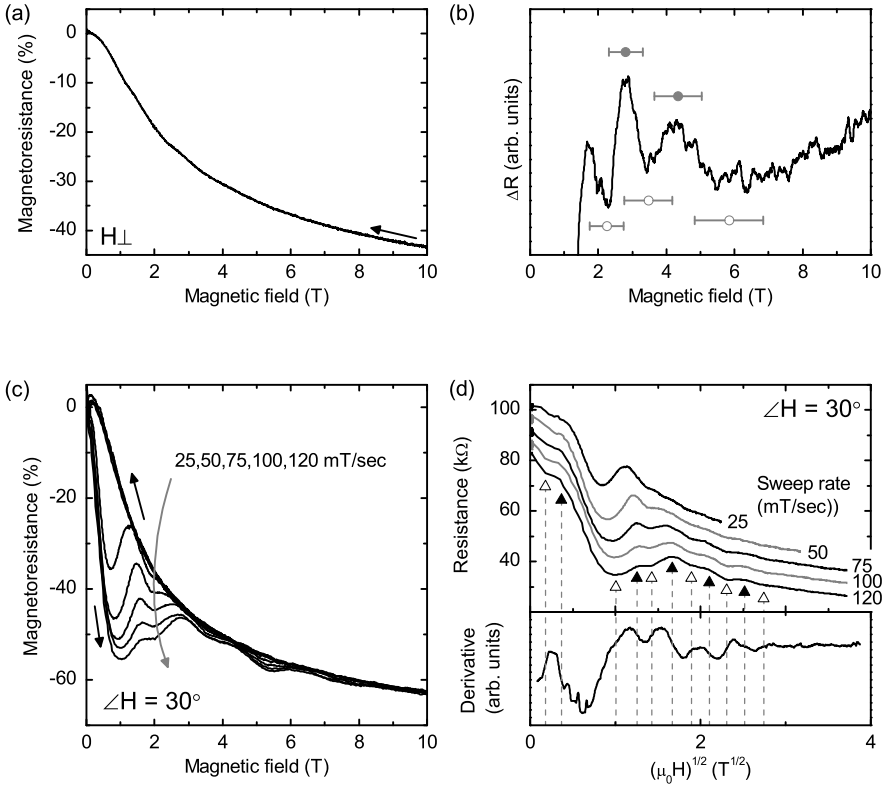

Figure 6.4: (a) The magnetoresistance of the 10^{-3} mbar sample shows weak fluctuations at 50 mK in perpendicular magnetic field. The curve was recorded using a magnetic field sweep rate of 33.3 mT s^{-1}. (b) Magnetoresistance oscillations were found after subtracting the smooth function $-98+92(\mu_0 H)^{-0.23}$ from the curve in (a). Three minimum and two maximum positions are indicated. (c) The same sample was mounted such that the angle between the field and the sample surface was 30°. At 50 mK, the magnitude of the oscillations could be enhanced in the hysteresis loop for increasing field by using higher field sweep rates. In (d) the upsweeps are plotted (offset for clarity) as function of $\sqrt{H}$ and minimum and maximum positions were determined for the 120 mT s^{-1} sweep rate.

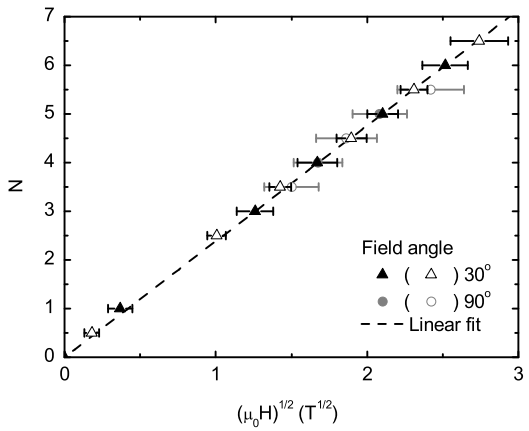

Figure 6.5: By counting, (half) integer values were attributed to the maxima (minima) in Fig. 6.4. The magnetoresistance oscillations show a $\sqrt{H}$ periodicity.

Because of the advantage of resolving more oscillations, we have used the highest sweep rate of 120 mT s^{-1} to determine minima and maxima for the oscillations in the upsweep. Note that the minimum and maximum positions appear to be only weakly dependent on the field sweep rate, so that this choice is justified.

We have, by counting, assigned a number to the minima and maxima (integer values for the maxima) and plotted these numbers against the square root of the magnetic field. When we assume that there is one oscillation hidden in the steep resistance decrease around $\sqrt{\mu_0 H} = 0.6$ T$^{1/2}$, we find a striking $\sqrt{H}$ dependence of the periodicity of the oscillations (Fig. 6.5). A H^{-1} or H periodicity as arising due to the Shubnikov-de Haas or commensurability oscillations in semiconductor 2DEGs certainly does not fit. The $\sqrt{H}$ behavior possibly indicates a connection with the Landau length $l_{\mathrm{L}} = \sqrt{\hbar/e\mu_0 H}$. Commensurability of the Landau length and an external length scale W, giving rise rise to a condition $N \times 2l_{\mathrm{L}} = W$, with N an integer, would explain the observed $\sqrt{H}$ behavior of the minimum and maximum positions. The extracted value for W (122 nm) compares reasonably well to the average terrace width of the STO substrate as determined by AFM (190 nm). Such a scenario matches well with the observation of resistance anisotropy mentioned in Sec. 6.1.3. However, the datapoints obtained in perpendicular field in Fig. 6.4(b) coincide perfectly with those obtained for the 30° orientation. This would imply that the oscillations are unrelated to the possible two-dimensionality of the interface electron gas, and the applicability of the commensurability model is questionable. However, it should be noted that the sample resistance had increased between the measurement for different orientations, so that the apparent orientation independence could be a coincidence.

The oscillatory behavior was reproduced on a 20×30 μm^2 cloverleaf structure at 50 mK (Fig. 6.6). In this case, oscillations were observed up to the highest fields

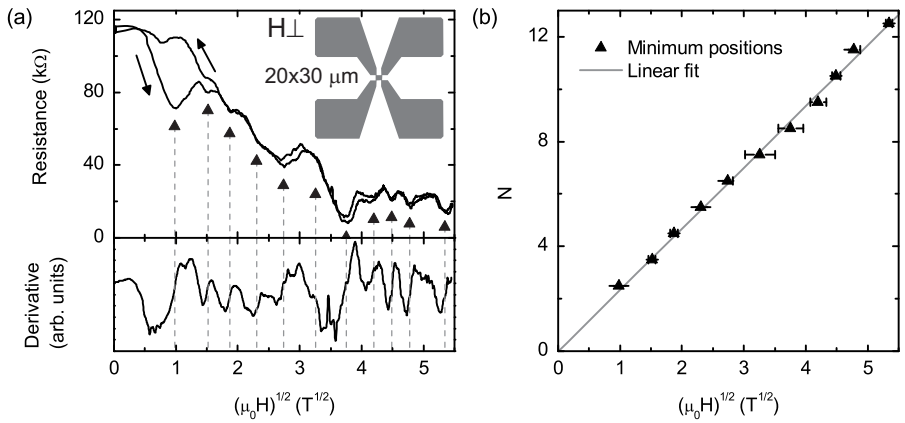

Figure 6.6: (a) Measurements on a 20×30 μm^2 cloverleaf structure grown at $pO_2 = 10^{-3}$ mbar show oscillations as well at 50 mK. The magnetic field was applied perpendicular to the interface. Minimum positions are denoted by triangles. The $\sqrt{H}$ periodicity of the oscillations is shown in (b).

of 30 T, both in increasing as well as in decreasing fields. The oscillations were found to be sweep rate independent and persisted for the lowest field sweep rates (1 mT s^{-1}). Sweep rate dependent hysteresis was also present in this sample. The periodicity of the oscillations observed for this sample is consistent with the $\sqrt{H}$-periodicity observed for the unstructured sample. Preliminary *in situ* rotation experiments indicate independence of magnetic field orientation for the structured sample too, which further indicates that the oscillations do not originate from the two-dimensional nature of the interface electron gas.

Magnetic field sweeps on the structured sample are well reproducible for subsequent magnetic field sweeps, however over a timescale of hours, the oscillatory pattern of the resistance as a function of magnetic field changes, accompanied by an increase in the sample resistance. In one occasion the sample became completely insulating and no measurable currents would flow for voltages up to 5 V. The conducting behavior was then restored by warming up the sample to room temperature, after which it was cooled down again, without leaving the cryostat. Similar behavior is sometimes observed for semiconductor heterostructures, which can become carrier depleted for instance when exposed to high voltages due to static electricity. A recent study also reports history effects of the LAO/STO interface resistance. [14]

The increase of interface resistance over time mentioned above for the structured sample, was found to be accompanied by an increasing nonlinearity of the current-voltage characteristics of the contacts. For low voltages over the contact, the contact resistance could become large ($> M\Omega$). For these high contact resistances, we still observed magnetoresistance oscillations and therefore we speculate

that the oscillatory behavior of the magnetoresistance might be related to the contacting of the interface. However, magnetic field dependent measurements of the contact current-voltage characteristics did not directly reveal oscillatory behavior, so the specific role of the contacts remains unclear.

6.4 Conclusion and outlook

Magnetoresistance measurements on LAO/STO interfaces grown at high ($pO_2 > 10^{-3}$ mbar) oxygen deposition pressure reveal a strong negative magnetoresistance response. This observation is consistent with the finding of negative magnetoresistance for LAO/STO interfaces under application of an electric gate field,[13] suggesting that such behavior is characteristic for the LAO/STO interface in the low carrier density limit.

Independence of the magnetic field orientation indicates that the magnetoresistance is caused by spin scattering. This suggests that part of the Ti $3d$ electrons near the interface is localized and acts as a scatter center to the other electrons in the Ti $3d$ conduction band. Within such a scenario, the resistance minimum observed as a function of temperature, might be related to the Kondo effect.

Magnetoresistance oscillations were observed at 50 mK. The oscillatory behavior is unusual and shows a $\sqrt{H}$ periodicity. The oscillations are therefore unrelated to Shubnikov-de Haas resistance oscillations. The origin of the oscillations is yet unclear. To rule out any effects due to the contacting of the interface, the development of ohmic, low-resistive contacts to the interface is of importance.

The conductivity and magnetic effects induced at the interface between two non-magnetic, insulating complex oxides is quite interesting. The LAO/STO system illustrates the possibility to stabilize electronic phases at complex oxide interfaces, that are not shown by the bulk materials in which they lie between.

References

[1] A. Ohtomo and H. Y. Hwang, Nature **427**, 423 (2004).

[2] K. v. Klitzing, G. Dorda, and M. Pepper, Phys. Rev. Lett. **45**, 494 (1980).

[3] M. Huijben, G. Rijnders, D. H. A. Blank, S. Bals, S. Van Aert, J. Verbeeck, G. Van Tendeloo, A. Brinkman, and H. Hilgenkamp, Nat. Mater. **5**, 556 (2006).

[4] S. Thiel, G. Hammerl, A. Schmehl, C. W. Schneider, and J. Mannhart, Science **313**, 1942 (2006).

[5] M. Basletic, J.-L. Maurice, C. Carrétéro, G. Herranz, O. Copie, M. Bibes, É. Jacquet, K. Bouzehouane, S. Fusil, and A. Barthélémy, Nat. Mater. **7**, 621 (2008).

[6] N. Reyren, S. Thiel, A. D. Caviglia, L. Kourkoutis, G. Hammerl, C. Richter, C. W. Schneider, T. Kopp, A. S. Rüetschi, D. Jaccard, et al., Science **317**, 1196 (2007).

[7] M. Sing, G. Berner, K. Goß, A. Müller, A. Ruff, A. Wetscherek, S. Thiel, J. Mannhart, S. A. Pauli, C. W. Schneider, et al., Phys. Rev. Lett. **102**, 176805 (2009).

[8] T. Fix, J. L. MacManus-Driscoll, and M. G. Blamire, Appl. Phys. Lett. **94**, 172101 (2009).

[9] W. Siemons, G. Koster, H. Yamamoto, W. A. Harrison, G. Lucovsky, T. H. Geballe, D. H. A. Blank, and M. R. Beasley, Phys. Rev. Lett. **98**, 196802 (2007).

[10] A. Kalabukhov, R. Gunnarsson, J. Börjesson, E. Olsson, T. Claeson, and D. Winkler, Phys. Rev. B **75**, 121404 (2007).

[11] G. Herranz, M. Basletić, M. Bibes, C. Carrétéro, E. Tafra, E. Jacquet, K. Bouzehouane, C. Deranlot, A. Hamzić, J.-M. Broto, et al., Phys. Rev. Lett. **98**, 216803 (2007).

[12] A. Brinkman, M. Huijben, M. van Zalk, J. Huijben, U. Zeitler, J. C. Maan, W. G. van der Wiel, G. Rijnders, D. H. A. Blank, and H. Hilgenkamp, Nat. Mater. **6**, 493 (2007).

[13] A. Caviglia, S. Gariglio, N. Reyren, D. Jaccard, T. Schneider, M. Gabay, S. Thiel, G. Hammerl, J. Mannhart, and J. M. Triscone, Nature **456**, 624 (2008).

[14] C. Bell, S. Harashima, Y. Kozuka, M. Kim, B. G. Kim, Y. Hikita, and H. Y. Hwang, arXiv.org:0906.5310v1 (2009).

[15] S. Okamoto and A. Millis, Nature **428**, 630 (2004).

[16] N. Nakagawa, H. Y. Hwang, and D. A. Muller, Nat. Mater. **5**, 204 (2006).

[17] W. A. Harrison, E. A. Kraut, J. R. Waldrop, and R. W. Grant, Phys. Rev. B **18**, 4402 (1978).

[18] R. Pentcheva and W. E. Pickett, Phys. Rev. B **74**, 035112 (2006).

[19] J. Mannhart and D. G. Schlom, Nature **430**, 620 (2004).

[20] V. Vonk, M. Huijben, K. J. I. Driessen, P. Tinnemans, A. Brinkman, S. Harkema, and H. Graafsma, Phys. Rev. B **75**, 235417 (2007).

[21] P. R. Willmott, S. A. Pauli, R. Herger, C. M. Schlepütz, D. Martoccia, B. D. Patterson, B. Delley, R. Clarke, D. Kumah, C. Cionca, et al., Phys. Rev. Lett. **99**, 155502 (2007).

[22] Z. Zhong and P. Kelly, Europhys. Lett. **84**, 27001 (2008).

[23] C. L. Jia, S. B. Mi, M. Faley, U. Poppe, J. Schubert, and K. Urban, Phys. Rev. B **79**, 081405 (2009).

[24] G. Koster, B. L. Kropman, G. J. H. M. Rijnders, D. H. A. Blank, and H. Rogalla, Appl. Phys. Lett. **73**, 2920 (1998).

[25] G. J. H. M. Rijnders, G. Koster, D. H. A. Blank, and H. Rogalla, Appl. Phys. Lett. **70**, 1888 (1997).

[26] P. A. Lee and T. V. Ramakrishnan, Rev. Mod. Phys. **57**, 287 (1985).

[27] G. Bergmann, Phys. Rep. **107**, 1 (1984).

[28] W.-J. Son, E. Cho, B. Lee, J. Lee, and S. Han, Phys. Rev. B **79**, 245411 (2009).

[29] A. Savoia, D. Paparo, P. Perna, Z. Ristic, M. Salluzzo, F. M. Granozio, U. S. di Uccio, C. Richter, S. Thiel, J. Mannhart, et al., Phys. Rev. B **80**, 075110 (2009).

[30] S. S. A. Seo, Z. Marton, W. S. Choi, G. W. J. Hassink, D. H. A. Blank, H. Y. Hwang, T. W. Noh, T. Egami, and H. N. Lee, arXiv.org:0908.1358v1 (2009).

[31] Z. S. Popović, S. Satpathy, and R. M. Martin, Phys. Rev. Lett. **101**, 256801 (2008).

[32] M. A. Ruderman and C. Kittel, Phys. Rev. **96**, 99 (1954).

[33] C. Kittel, *Introduction to solid state physics* (Wiley, 2005), 8th ed.

[34] K. Moorjani and J. M. D. Coey, *Magnetic glasses*, vol. 6 of *Methods and phenomena* (Elsevier, 1984).

[35] J. Kondo, Prog. Theor. Phys. **32**, 37 (1964).

[36] L. Degiorgi, Rev. Mod. Phys. **71**, 687 (1999).

[37] P. Monod, Phys. Rev. Lett. **19**, 1113 (1967).

[38] K. Yosida, Phys. Rev. **107**, 396 (1957).

[39] N. W. Ashcroft and N. D. Mermin, *Solid state physics* (Thomson Learning, 1976).

[40] M. Oestreich and W. W. Rühle, Phys. Rev. Lett. **74**, 2315 (1995).

Appendix A Electrons and holes. Can the Coulomb force induce a Cooper instability?

Abstract

A multiband description for high-T_c superconductors has often been used to explain certain transport properties. In this appendix, we show that the Coulomb interaction between electrons and holes in a two-band system is insufficient to induce Cooper pairing.

A.1 Multiband model for high-T_c cuprates

The normal-state transport properties of the high-T_c superconductors have puzzled the scientific community ever since the discovery of high-T_c superconductivity in 1986. Over the years, a variety of models have been proposed to explain these transport properties, one of them being the multiband model. Already in 1989, Eagles proposed the coexistence of electrons and holes as an explanation for the temperature-dependence of the Hall coefficient.[1] Later, a similar analysis was performed for $Bi_2Sr_2CaCu_2O_y$.[2] The two-band picture has been embraced in particular for the n-type high-T_c cuprate $Nd_{2-x}Ce_xCuO_{4-\delta}$, due to the anomalous behavior of the transport properties. Jiang *et al.*[3] provided convincing evidence for the participation of both electrons and holes to the charge transport by revealing a sign change of the Hall coefficient as a function of doping and temperature. Two-band behavior was further substantiated by magnetotransport and thermoelectric power measurements.[4–6] The results raised questions about the n-type nature of superconductivity in this compound. But another question is whether the coexistence of both types of carriers is of importance to superconductivity. For $La_{2-x}Sr_xCuO_4$ (LSCO) a doping-dependent crossover from positive to negative Hall coefficient was found at $x = 0.3$.[7] Also for this material a two-band picture was proposed.[8] The observations from transport measurements are largely supported by angle resolved photoemission spectroscopy (ARPES) experiments. For p-type cuprates, the hole-type surface develops into an electron-type surface as a function of doping.[9–11] For the n-type $Nd_{2-x}Ce_xCuO_{4-\delta}$, the opposite effect has been observed.[12] Recent high-field transport studies shed new light on the issue of electrons and holes: a negative Hall coefficient in the field induced normal state

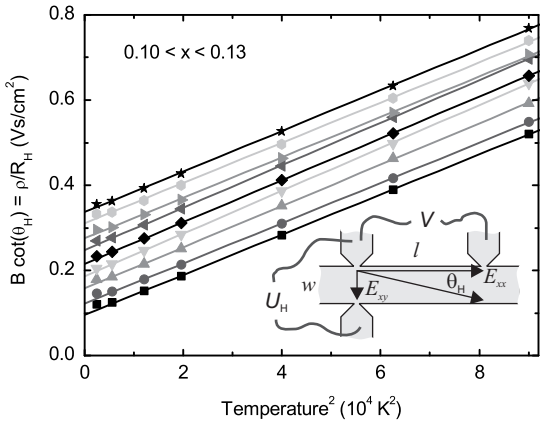

Figure A.1: The Hall angle for LSCO shows a T^2 dependence. Solid lines are linear fits to the data. Upper curves are offset for clarity.

of $YBa_2Cu_3O_y$ (YBCO) indicates the presence of electron pockets in the Fermi surface of this p-type cuprate.

There are, however, also arguments against the multiband description of high-T_c superconductors,[13] one of which we will discuss here. The transport properties of LSCO in the doping range $0.10 < x < 0.15$ were studied in Chapter 2. In Fig. A.1 we have plotted the Hall angle for LSCO ($0.10 < x < 0.13$) versus T^2, T being the temperature. The Hall angle is defined by $\tan\theta_H \equiv E_{xy}/E_{xx}$, where $E_{xx} = V/l$ is the longitudinal electric field and $E_{xy} = U_{\rm H}/w$ the transverse electric field, resulting from the Hall effect. The Hall angle shows a remarkable T^2 dependence, which is typical for LSCO and YBCO.[13,14] A small deviation is only present in the temperature range 50–75 K, where we have seen parabolic magnetoresistance resulting from superconducting fluctuations in Chapter 2. The Hall angle can be expressed in terms of the resistivity ρ and the Hall coefficient $R_{\rm H}$

$$\cot\theta_H = \frac{E_{xx}}{E_{xy}} = \frac{\rho}{R_H}\frac{1}{B}\,. \tag{A.1}$$

The magnetic field dependent resistivity and Hall coefficient for a two-band system with positive and negative charge carriers can be written as:[15]

$$\rho = \frac{1}{e}\frac{p\mu_{\rm p} + n\mu_{\rm n} + \mu_{\rm p}\mu_{\rm n}(\mu_{\rm p}n + \mu_{\rm n}p)B^2}{(p\mu_{\rm p} + n\mu_{\rm n})^2 + \mu_{\rm p}^2\mu_{\rm n}^2(p-n)^2B^2}\,, \tag{A.2}$$

$$R_H = \frac{1}{e}\frac{p\mu_{\rm p}^2 - n\mu_{\rm n}^2 + \mu_{\rm p}^2\mu_{\rm n}^2(p-n)B^2}{(p\mu_{\rm p} + n\mu_{\rm n})^2 + \mu_{\rm p}^2\mu_{\rm n}^2(p-n)^2B^2}\,, \tag{A.3}$$

in which p, n, $\mu_{\rm p}$ and $\mu_{\rm n}$ are respectively the carrier density and mobility of the hole and electron band, e is the elementary charge and B is the magnetic field.

For the two-band model, we find

$$\cot\theta_H = \frac{p\mu_\mathrm{p} + n\mu_\mathrm{n} + \mu_\mathrm{p}\mu_\mathrm{n}(\mu_\mathrm{p}n + \mu_\mathrm{n}p)B^2}{p\mu_\mathrm{p}^2 - n\mu_\mathrm{n}^2 + \mu_\mathrm{p}^2\mu_\mathrm{n}^2(p-n)B^2}\frac{1}{B}\,, \tag{A.4}$$

which reduces for small fields to

$$\cot\theta_H = \frac{p\mu_\mathrm{p} + n\mu_\mathrm{n}}{p\mu_\mathrm{p}^2 - n\mu_\mathrm{n}^2}\frac{1}{B} \tag{A.5}$$

and for a single (hole) band to simply

$$\cot\theta_H = \frac{1}{\mu_\mathrm{p}}\frac{1}{B}\,. \tag{A.6}$$

It is clear from Eq. A.6 that a simple physical law of the form $1/\tau = AT^2 + C$, with A and C constants, would give a satisfactory description of the Hall effect in LSCO. Anderson has proposed a theory which gives rise to such a temperature-dependence of the scattering rate.[16] It is more difficult to reconcile the two-band model with the T^2 behavior of the Hall angle. From Eq. A.5 it follows that the temperature dependences of the carrier densities are reflected in the Hall angle, unless $p(T) \propto n(T)$. But even in this case, there are constraints for μ_p and μ_n to end up with $B\coth\theta_\mathrm{H} \propto AT^2{+}C$. For instance, $\mu_\mathrm{n}^{-1} \propto \mu_\mathrm{p}^{-1} = AT^2{+}B$ would yield such temperature dependence. However, these conditions are generally not met in two-band analyses of the temperature dependent resistivity and Hall coefficient. Thus, for compounds exhibiting T^2 behavior of the Hall angle, care has to be taken when interpreting transport properties in terms of a multiband model.

In spite of these considerations, the coexistence of electrons and holes in itself is interesting and deserves a second thought. In Ref. 17, electron-hole coupling was proposed, either due to a mutual attractive Coulomb interaction, or due to a repulsive interaction between quasiparticles of opposite effective mass. Once formed, the electron-hole pairs might undergo a Bose-Einstein condensation at rather high temperatures (in the range of 10 to 100 K) due to the small masses of the constituents. In Sec. A.2, we will elaborate this idea by looking for an instability of the normal state of a metallic two-band system, consisting of an electron-like and hole-like band, in the presence of a mutual Coulomb interaction. Remember that both in the electron-like and the hole-like band charge transport ultimately takes place by means of electrons. The hole-like character of the latter is the result of the band being filled for the larger part (but not completely). Charge transport can then be described by attributing positive *charge* to the unoccupied states (holes) which behave as quasiparticles with positive mass, hence the hole-like character. The system is equally well described by attributing a negative effective *mass* to the occupied states (electrons) which carry a negative charge.[18] Here, the latter approach will be used. We will find that the Coulomb interaction in such a two-band system cannot invoke an instability. Note the difference between our

electron-hole pairs and excitons: the latter consist of excited electrons, separated from the holes in energy-space by a bandgap. The exciton energy is lowered by the Coulomb interaction between the electron and the hole. However, the energy gain of the interaction is smaller than the initial excitation energy of the electron and hence, excitons will not spontaneously form.

A.2 Cooper instability

The ground state of an electron gas is unstable if a weak attractive interaction is added between each pair of electrons.[19] This Cooper instability leads to the formation of electron pairs (Cooper pairs) and an energy gap, associated with the breaking of such pairs, and underlies superconductivity. In search for a Coulomb force induced instability in a two-band system, we will closely follow the derivation for a Cooper instability in a single band, which can be found for example in DeGennes's textbook (Chapter 4 in Ref. 20).

A.2.1 Wavefunctions

We start by expanding the electron and hole wavefunctions in plane waves:

$$\begin{aligned} \psi_{\rm e}(\mathbf{r}_{\rm e}) &= \sum_{\mathbf{k}} g_{\rm e}(\mathbf{k}) e^{i\mathbf{k}\cdot\mathbf{r}_{\rm e}} , \\ \psi_{\rm h}(\mathbf{r}_{\rm h}) &= \sum_{\mathbf{k}} g_{\rm h}(\mathbf{k}) e^{i\mathbf{k}\cdot\mathbf{r}_{\rm h}} . \end{aligned} \tag{A.7}$$

Assuming an independent electron and hole band, the total wavefunction can be written as the product of the electron and hole wavefunctions

$$\begin{aligned} \psi(\mathbf{R},\mathbf{r}) = \psi_{\rm e}(\mathbf{r}_{\rm e})\psi_{\rm h}(\mathbf{r}_{\rm h}) &= \sum_{\mathbf{k},\mathbf{k}'} g_{\rm e}(\mathbf{k}) g_{\rm h}(\mathbf{k}') e^{i\mathbf{k}\mathbf{r}_{\rm e}} e^{i\mathbf{k}'\mathbf{r}_{\rm h}} \\ &= \sum_{\mathbf{k},\mathbf{k}'} g_{\rm e}(\mathbf{k}) g_{\rm h}(\mathbf{k}') e^{i(\mathbf{k}+\mathbf{k}')\mathbf{R}} e^{i(\mathbf{k}-\mathbf{k}')\frac{1}{2}\mathbf{r}} . \end{aligned} \tag{A.8}$$

Here, the coordinate transformations

$$\begin{aligned} \mathbf{r} &= \mathbf{r}_{\rm e} - \mathbf{r}_{\rm h} \\ \mathbf{R} &= \frac{1}{2}(\mathbf{r}_{\rm e} + \mathbf{r}_{\rm h}) \end{aligned} \tag{A.9}$$

are used. In principle, we could only consider states with zero total momentum, i.e. with $\mathbf{k}' = -\mathbf{k}$. In this case, the wavefunction would be

$$\psi(\mathbf{r}) = \sum_{\mathbf{k}} g_{\rm e}(\mathbf{k}) g_{\rm h}(-\mathbf{k}) e^{i\mathbf{k}\cdot\mathbf{r}} \equiv \sum_{\mathbf{k}} g(\mathbf{k}) e^{i\mathbf{k}\cdot\mathbf{r}} . \tag{A.10}$$

However, we might as well be interested in electrons-hole pairs with non-zero momentum and we will carry out this generalization further on.

A.2.2 Schrödinger equation

The Schrödinger equation for the electron and hole including the Coulomb potential is

$$\left[E_{\mathrm{e}} - \frac{\hbar^2}{2|m_{\mathrm{e}}|}\nabla^2_{\mathbf{r}_{\mathrm{e}}} + E_{\mathrm{h}} + \frac{\hbar^2}{2|m_{\mathrm{h}}|}\nabla^2_{\mathbf{r}_{\mathrm{h}}} + V(\mathbf{r}_{\mathrm{e}} - \mathbf{r}_{\mathrm{h}})\right]\psi(\mathbf{r}_{\mathrm{e}}, \mathbf{r}_{\mathrm{h}}) = (E + 2E_{\mathrm{F}})\psi(\mathbf{r}_{\mathrm{e}}, \mathbf{r}_{\mathrm{h}})\,. \tag{A.11}$$

The opposite signs of the masses of the electrons and holes (m_{e} and m_{h}) are put explicitly in the equation. E_{e} and E_{h} define the bottom of the electron band and the top of the hole band. For both bands to be partly filled $E_{\mathrm{e}} - E_{\mathrm{F}} < 0$ and $E_{\mathrm{h}} - E_{\mathrm{F}} > 0$. After putting the wavefunction of Eq. A.8 into the Schrödinger equation and Fourier transforming it with respect to $\mathbf{r}$ and $\mathbf{R}$, one arrives at

$$\begin{aligned}
&\frac{\hbar^2}{2|m_{\mathrm{e}}|}g_{\mathrm{e}}(\mathbf{k})g_{\mathrm{h}}(\mathbf{k}')k^2 - \frac{\hbar^2}{2|m_{\mathrm{h}}|}g_{\mathrm{e}}(\mathbf{k})g_{\mathrm{h}}(\mathbf{k}')(k')^2 \\
&+ \frac{1}{L^6}\iint V(\mathbf{r})\psi(\mathbf{R}, \mathbf{r})e^{-i\frac{1}{2}(\mathbf{k}-\mathbf{k}')\cdot\mathbf{r}}e^{-i(\mathbf{k}+\mathbf{k}')\cdot\mathbf{R}}\mathrm{d}\mathbf{r}\mathrm{d}\mathbf{R} \\
&= (E - E_{\mathrm{e}} - E_{\mathrm{h}} + 2E_{\mathrm{F}})g_{\mathrm{e}}(\mathbf{k})g_{\mathrm{h}}(\mathbf{k}')\,.
\end{aligned} \tag{A.12}$$

Here, L^3 is the volume of the system.

A.2.3 Coulomb potential

We can proceed by evaluating the interaction term in Eq. A.12 explicitly. Carrying out the Fourier transformation with respect to R yields

$$\begin{aligned}
&\frac{1}{L^6}\iint V(\mathbf{r})\psi(\mathbf{R}, \mathbf{r})e^{-i\frac{1}{2}(\mathbf{k}-\mathbf{k}')\cdot\mathbf{r}}e^{-i(\mathbf{k}+\mathbf{k}')\cdot\mathbf{R}}\mathrm{d}\mathbf{r}\mathrm{d}\mathbf{R} \\
&= \frac{1}{L^3}\sum_{\mathbf{q}'} g_{\mathrm{e}}(\mathbf{k} - \mathbf{q}')g_{\mathrm{h}}(\mathbf{k}' + \mathbf{q}')\int V(\mathbf{r})e^{-i\mathbf{q}'\cdot\mathbf{r}}\mathrm{d}\mathbf{r} \\
&= \frac{1}{L^3}\sum_{\mathbf{q}} g_{\mathrm{e}}(\mathbf{q})g_{\mathrm{h}}(\mathbf{k} + \mathbf{k}' - \mathbf{q})\int V(\mathbf{r})e^{-i(\mathbf{k}-\mathbf{q})\cdot\mathbf{r}}\mathrm{d}\mathbf{r}\,.
\end{aligned} \tag{A.13}$$

The Coulomb potential energy term for the electron-hole pair is

$$V(\mathbf{r}_{\mathrm{e}} - \mathbf{r}_{\mathrm{h}}) = \frac{e^2}{4\pi\epsilon}\frac{1}{|\mathbf{r}_{\mathrm{e}} - \mathbf{r}_{\mathrm{h}}|} = \frac{e^2}{4\pi\epsilon}\frac{1}{|\mathbf{r}|}\,. \tag{A.14}$$

In three dimensions, the Fourier transform of the Coulomb interaction potential is

$$V_{\mathbf{kq}} \equiv \int V(\mathbf{r})e^{-i(\mathbf{k}-\mathbf{q})\cdot\mathbf{r}}\mathrm{d}\mathbf{r} = \frac{e^2}{4\pi\epsilon}\int\frac{1}{|\mathbf{r}|}e^{-i(\mathbf{k}-\mathbf{q})\cdot\mathbf{r}}\mathrm{d}\mathbf{r} = \frac{e^2}{\epsilon}\frac{1}{|\mathbf{k} - \mathbf{q}|^2}\,. \tag{A.15}$$

In realistic metals, there exists screening and we must use a Thomas-Fermi potential. The potential is screened exponentially, the inverse of the screening length

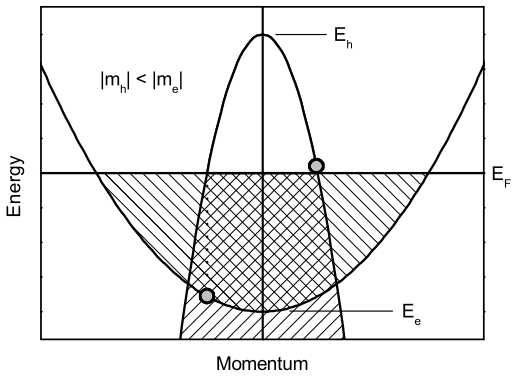

Figure A.2: Schematic picture of a two-band system consisting of a light hole band and a heavy electron band. The pair that is drawn in the picture, has a negative energy relative to the Fermi energy. This is however due to the negative energy of the electron in the electron band. The electron in the hole band would gain energy when relaxing to below the Fermi energy since the interaction energy would not change. Thus, there is no Cooper instability due to the Coulomb interaction in a system with an electron-like and a hole-like band.

being q_0. The Fourier transform of the screened potential reads

$$V_{\mathbf{kq}} = \frac{e^2}{4\pi\epsilon}\int \frac{1}{|\mathbf{r}|}e^{-q_0|\mathbf{r}|}e^{-i(\mathbf{k}-\mathbf{q})\cdot\mathbf{r}}\mathrm{d}\mathbf{r} = \frac{e^2}{\epsilon}\frac{1}{|\mathbf{k}-\mathbf{q}|^2+q_0^2}\,. \tag{A.16}$$

With this, Eq. A.12 can be written as

$$\begin{aligned}&\frac{\hbar^2}{2|m_\mathrm{e}|}g_\mathrm{e}(\mathbf{k})g_\mathrm{h}(\mathbf{k}')k^2 - \frac{\hbar^2}{2|m_\mathrm{h}|}g_\mathrm{e}(\mathbf{k})g_\mathrm{h}(\mathbf{k}')(k')^2\\ &+\frac{1}{L^3}\sum_{\mathbf{q}} g_\mathrm{e}(\mathbf{q})g_\mathrm{h}(\mathbf{k}+\mathbf{k}'-\mathbf{q})V_{\mathbf{kq}}\\ &=(E-E_\mathrm{e}-E_\mathrm{h}+2E_\mathrm{F})g_\mathrm{e}(\mathbf{k})g_\mathrm{h}(\mathbf{k}')\,.\end{aligned} \tag{A.17}$$

A.2.4 Instability

We can now try to find an instability in the two-band system, i.e., solutions to the distribution functions $g_\mathrm{e}(\mathbf{k})g_\mathrm{h}(\mathbf{k}')$ with $E<0$. To simplify Eq. A.17, let us assume that the top of the hole band is just as high above the Fermi level as the bottom of the electron band is below it, so that $2E_\mathrm{F}-E_\mathrm{e}-E_\mathrm{h}=0$. The arising situation is sketched in Fig. A.2. Furthermore let us now look at pairs with zero total momentum, by setting $\mathbf{k}'=-\mathbf{k}$. From Eq. A.16 we see that the interaction $V_{\mathbf{kq}}$ is more or less constant for $|\mathbf{k}-\mathbf{q}|\ll q_0$ and decreases for larger $|\mathbf{k}-\mathbf{q}|$. Here we will approximate it by a constant positive interaction V for small $|\mathbf{k}-\mathbf{q}|$ and zero otherwise. Note that for metals q_0 generally is of the order of k_F. Using all

these approximations and simplifications, one finds:

$$\frac{\hbar^2}{2}\left(\frac{1}{|m_\mathrm{e}|}-\frac{1}{|m_\mathrm{h}|}\right)g(\mathbf{k})k^2+\frac{V}{L^3}\sum_{\mathbf{q}}g(\mathbf{k}-\mathbf{q})=Eg(\mathbf{k})\,. \tag{A.18}$$

For $|m_\mathrm{e}|<|m_\mathrm{h}|$ we find an equation that is very similar to the well-known result for the Cooper problem (see for example Ref. 20), except for the positive potential term, instead of the attractive interaction for a Cooper pair. In this case, a stable pair can never be formed. For $|m_\mathrm{h}|<|m_\mathrm{e}|$, Eq. A.18 looks more promising, since the first term on the left hand side is negative. Now $E<0$ solutions might exist, even though the interaction energy is positive. However, upon multiplying both sides of the equation by -1, one would not only change the sign of the interaction energy, but also that of the energy E. Thus, a solution similar to that for the Cooper instability can be written down, but the energy would again be $E>0$ and no bound states will be formed. In Fig. A.2, we have drawn a pair for which $|m_\mathrm{h}|<|m_\mathrm{e}|$. The absence of an instability is clear. The energy of the pair is negative with respect to E_F, because one of the electrons resides below E_F. For an instability to occur, one should be able to create a negative energy pair *above* the Fermi energy. This is not possible without *attractive* interactions between the quasiparticles. Note that this argument is general and does not rely on the condition $\mathbf{k}'=-\mathbf{k}$.

In conclusion, the Coulomb force alone cannot induce a Cooper instability in a two-band system, no matter the bands are electron-like, hole-like or a combination of the two. For superconductivity arising from the coexistence of electrons and holes, one would have to go beyond the simple picture described in this appendix.

References

[1] D. M. Eagles, Sol. State Comm. **69**, 229 (1989).

[2] T. Honma, K. Yamaya, F. Minami, and S. Takekawa, Physica C **176** (1991).

[3] W. Jiang, S. N. Mao, X. X. Xi, X. Jiang, J. L. Peng, T. Venkatesan, C. J. Lobb, and R. L. Greene, Phys. Rev. Lett. **73**, 1291 (1994).

[4] P. Seng, J. Diehl, S. Klimm, S. Horn, R. Tidecks, K. Samwer, H. Hänsel, and R. Gross, Phys. Rev. B **52**, 3071 (1995).

[5] P. Fournier, X. Jiang, W. Jiang, S. N. Mao, T. Venkatesan, C. J. Lobb, and R. L. Greene, Phys. Rev. B **56**, 14149 (1997).

[6] C. H. Wang, G. Y. Wang, T. Wu, Z. Feng, X. G. Luo, and X. H. Chen, Phys. Rev. B **72**, 132506 (2005).

[7] H. Takagi, T. Ido, S. Ishibashi, M. Uota, S. Uchida, and Y. Tokura, Phys. Rev. B **40**, 2254 (1989).

[8] N. Luo, Physica C **350**, 132 (2001).

[9] A. Ino, C. Kim, M. Nakamura, T. Yoshida, T. Mizokawa, A. Fujimori, Z.-X. Shen, T. Kakeshita, H. Eisaki, and S. Uchida, Phys. Rev. B **65**, 094504 (2002).

[10] T. Yoshida, X. J. Zhou, T. Sasagawa, W. L. Yang, P. V. Bogdanov, A. Lanzara, Z. Hussain, T. Mizokawa, A. Fujimori, H. Eisaki, et al., Phys. Rev. Lett. **91**, 027001 (2003).

[11] M. R. Norman, H. Ding, M. Randeria, J. C. Campuzano, T. Yokoya, T. Takeuchik, T. Takahashi, T. Mochiku, K. Kadowaki, P. Guptasarma, et al., Nature **392**, 157 (1998).

[12] N. P. Armitage, F. Ronning, D. H. Lu, C. Kim, A. Damascelli, K. M. Shen, D. L. Feng, H. Eisaki, Z.-X. Shen, P. K. Mang, et al., Phys. Rev. Lett. **88**, 257001 (2002).

[13] T. R. Chien, Z. Z. Wang, and N. P. Ong, Phys. Rev. Lett. **67**, 2088 (1991).

[14] G. Xiao, P. Xiong, and M. Z. Cieplak, Phys. Rev. B **46**, 8687 (1992).

[15] N. W. Ashcroft and N. D. Mermin, *Solid state physics* (Thomson Learning, 1976).

[16] P. W. Anderson, Phys. Rev. Lett. **67**, 2092 (1991).

[17] A. Brinkman and H. Hilgenkamp, Physica C **422**, 71 (2005).

[18] H. Ibach and H. Lüth, *Solid-state physics: an introduction to principles of materials science* (Springer-Verlag, Berlin, 1995), 2nd ed.

[19] L. N. Cooper, Phys. Rev. **104**, 1189 (1956).

[20] P. G. de Gennes, *Superconductivity of Metals and Alloys* (Addison-Wesley, 1989).

Summary

Complex oxides are emerging as a versatile class of materials, exhibiting a wide variety of properties, from high-temperature (high-T_c) superconductivity to (fully spin-polarized) ferromagnetism, colossal magnetoresistance, and ferroelectricity. In recent years, it has become increasingly clear that the properties of complex-oxide interfaces can differ considerably from those of the bulk. This opens up the possibility of tuning and improving interface properties. In addition, it might enable the stabilization of novel phases at the interface. When applications or devices involve combinations of different complex oxides, understanding and control of interface properties are imperative. This thesis therefore focuses on complex oxide interfaces. Their properties are studied for four different cases.

In the first case, the influence of $SrTiO_3$ (STO) substrates on the high-T_c superconductor and strongly correlated electron system $La_{2-x}Sr_xCuO_4$ (LSCO) is examined. It is found that the substrate influences the LSCO film through epitaxial strain. Surprisingly, a small tetragonal modification below the cubic-tetragonal phase transition of the STO at 105 K, clearly affects the electronic properties of the LSCO film. It is found that the conductance anisotropy for $x = 0.10$–0.13 changes abruptly under the influence of this phase transition. The anisotropic contribution to the conductance is directed along Cu-O bonds. It has been argued that this contribution is due to so-called stripes. Stripes are extended self-assembling patterns of charges and spins. For doping levels x for which such indications for stripe order are found, it is also observed that the magnetoresistance shows peculiar behavior. A component which depends linearly on magnetic field adds to the magnetoresistance, which has also been reported for LSCO single crystals in a narrow doping range around $x = 0.125$. The marked difference between single-crystal and the present thin-film data is the abrupt vanishing of the linear contribution below 90 K for the latter. This difference has to arise from the presence of the STO substrate, for instance through the epitaxial strain exerted by the substrate. The magnetoresistance as well as the conductance anisotropy behavior strongly suggest that linear magnetoresistance is a fingerprint of fluctuating stripes, which become pinned by the structural modification enforced from the substrate phase transition. The LSCO case further learns that doping-graded films can be grown by pulsed laser deposition by positioning the sample out of the center of the plasma plume. In addition, it is found that an anisotropic component to the thin-film

conductivity is present, which is induced by the stepped character of the STO substrate. This implies that such substrate steps are dominant sources for planar defects (antiphase boundaries) during LSCO film growth.

The second case is a tunnel study for which a variety of tunnel junctions is prepared, for the purpose of tunnel junction spectroscopy on LSCO. All different structures show rather featureless tunnel spectra, with pronounced linear conductance backgrounds, which are in some cases asymmetric and sometimes exhibit a gap-like feature. The results indicate a suppressed carrier density at the interface between the superconductor and the insulating tunnel barrier. Tunneling then takes place into a locally underdoped, non-superconducting surface layer. The data have been analyzed using a variety of models. The linear conductance background and asymmetry can be accounted for by assuming the occurrence of inelastic tunneling, although a linear conductance background due to tunneling via localized states cannot fully be excluded. Strong electron correlations cannot explain the observed asymmetry, since the conductance is largest for electrons entering the LSCO, which is at odds with theoretical predictions.

The third case, the $YBa_2Cu_3O_7/La_{0.67}Sr_{0.33}MnO_3$ (YBCO/LSMO) interface, is studied using two different approaches. Ramp-type YBCO/LSMO contacts and YBCO/LSMO/YBCO junctions have been fabricated to investigate transport through this interface. The junctions and contacts are characterized by a large normal-state resistance of about 3 $\mu\Omega cm^2$. A comparison has been made with ramp-type contacts for which the LSMO was replaced by several other materials, including the high-temperature grown, ferromagnetic oxide $SrRuO_3$ (SRO). The YBCO/SRO interface resistance is found to be about 0.1 $\mu\Omega cm^2$ and YBCO/Au and YBCO/Pt interfaces both are about 0.03 $\mu\Omega cm^2$. The interface resistance appears to scale with the work function difference between YBCO and the top electrode material. At the same time, deoxidation of YBCO might occur most strongly for YBCO in contact with LSMO, compared to SRO, Au, and Pt, as the Gibbs free energy decrease is largest for oxidation of the constituent elements of LSMO. The high interface resistance of the YBCO/LSMO interface could therefore be caused by oxygen deficiency in the YBCO. However, the temperature dependence of the interface resistance does not support this scenario. In addition, an elemental oxygen mapping of the junction cross section by electron energy loss spectroscopy has been prepared, which has not resolved oxygen deficiency near the interface. Instead of to oxygen deficiency, the high interface resistance of the LSMO/YBCO interface is attributed to the transfer of charge across the interface, driven by the work function difference between YBCO and LSMO. The interplay between an antiferromagnetic tendency in YBCO and spin-polarized ferromagnetism in LSMO is expected to give rise to an additional contribution to the interface resistance. This antiferromagnetic tendency of YBCO will be enhanced by the carrier depletion near the interface. As a result, a fraction of the charge carriers arriving at the interface might be blocked. Experimentally, it is found that the interface resistance shows a large magnetic field dependence, which indicates that part of the interface resistance is of magnetic origin, and supports the block-

ing scenario. Ideal Josephson junction behavior has not been observed in YBCO junctions with LSMO barriers.

In a second approach, epitaxial YBCO/LSMO and LSMO/YBCO bilayers have been grown as well as trilayers in a superconducting spin-switch geometry (sandwiching the superconductor between two ferromagnetic layers, i.e., LSMO/YBCO/LSMO). For such a geometry, theory predicts the possibility of switching superconductivity on and off by manipulating the magnetization state (parallel or antiparallel) of the two magnetic layers. Such behavior has been observed experimentally in superconductor/ferromagnet structures with low-T_c superconductors. Literature data of oxide heterostructures show resistance switching effects at temperatures close to T_c as function of magnetic field. So far, these have been interpreted either in terms of the superconducting spin-switch effect, or as a result of the injection of spin-polarized charge carriers into the superconductor. In order to enhance such effects, trilayers have been fabricated by tilted epitaxial growth on STO (305) substrates, with the c axis rotated 31° with respect to the sample surface. It has been found that the LSMO layers grown this way exhibit uniaxial magnetic anisotropy, and nearly ideal, single domain magnetization switching. This greatly suppresses stray fields due to ferromagnetic domains. The resistance switching then observed is clearly not uniquely defined by the magnetization state (parallel or antiparallel) of the ferromagnetic layers, but rather depends on the direction of the external field and the magnetization directions of the two ferromagnetic layers individually. This indicates that the resistance switching effects are caused by the penetration of magnetic field through the superconductor, with the total magnetic field given by the external field and stray-field contributions from the ferromagnetic layers. Roughness of the YBCO/LSMO interface plays an important role. It has been shown that rough interfaces induce larger resistance switching effects than smooth interfaces, which can be understood from increased stray fields penetrating the superconductor. The stray-field model is supported by measurements on bilayers. Pronounced resistance switching has been observed for YBCO/LSMO bilayers on STO (305), which have a considerably rough YBCO/LSMO interface.

Whereas the interface between the conductors YBCO and LSMO is highly resistive, the interface between the two perovskite insulators $LaAlO_3$ (LAO) and STO is conducting, which is the subject of the last case in this thesis. Several experiments described in the literature indicate that the conducting sheet is confined to a narrow (up to a few nm) region near the interface. The low-temperature and high-magnetic-field properties of this conducting interface have been investigated in this thesis. The focus has been on interfaces prepared by deposition of LAO on TiO_2-terminated STO substrates at relatively high ($\geq 1.0 \times 10^{-3}$ mbar) oxygen deposition pressure. Such interfaces have a larger resistance than interfaces grown at lower oxygen pressure, which exhibit superconductivity below 200 mK. Furthermore the resistance of the high-pressure interfaces increases for decreasing temperatures below about 70 K, while low-pressure grown interfaces show a monotonically decreasing resistance. At low temperature (50 mK) the high-pressure-grown interfaces show a large (> 50 %) magnetoresistance, which is independent of

the direction of applied magnetic field. This suggests that the magnetoresistance is a spin, rather than an orbital effect. It has been argued that spin scattering arises from the coexistence of localized and mobile electrons, with the localized electrons acting as magnetic moments off which mobile electrons scatter. Within this picture, the resistance increase below 70 K might be a signature of the Kondo effect. At 50 mK, oscillations are resolved in the magnetoresistance. Their amplitude can be greatly enhanced by increasing the magnetic field sweep rate. The oscillations exhibit a peculiar $\sqrt{H}$ periodicity, with H being the magnetic field. In a 10×30 μm^2 cloverleaf structure similar oscillations are observed for which magnetic field sweep rate independence was confirmed. The periodicity of the oscillations is independent of the orientation of the magnetic field. The unusual periodicity and absence of field-orientation dependence rule out explanations in terms of Landau quantization, and the origin of the oscillations requires further investigation.

The four cases described above all indicate the sensitivity of oxides to deviations in properties near interfaces. Strain, charge transfer, interplay between different kinds of magnetic ordering, stray fields, and structural as well as electronic reconstructions are all factors influencing oxide behavior at the interface. These enable the manipulation of a wide range of phenomena, from stripe ordering in LSCO to resistance switching in nearly superconducting YBCO and spin-dependent transport in between non-magnetic insulators.

The appendix to this thesis discusses the hypothesis of Cooper pairing due to Coulomb interactions between coexisting electrons and holes in the cuprates. Although the two-band picture has been popular in the literature for explaining certain transport properties in the cuprates, it is difficult to reconcile with the temperature dependence of the Hall angle as shown in the appendix. Nevertheless, a simple two-band model for superconductivity has been elaborated, which shows that the repulsive force between quasiparticles in electron-like and hole-like bands cannot give rise to a Cooper instability.

Samenvatting

Complexe oxiden vormen een veelzijdige materiaalklasse, met eigenschappen die variëren van supergeleiding bij hoge temperatuur (hoge T_c) tot (volledig spingepolariseerd) ferromagnetisme, kolossale magnetoweerstand en ferro-elektriciteit. De laatste jaren is het steeds meer duidelijk geworden dat de eigenschappen van grensvlakken tussen complexe oxiden sterk kunnen verschillen van die van de materialen zelf. Dit schept niet alleen de mogelijkheid van het beïnvloeden en verbeteren van de grensvlakeigenschappen, maar ook mogelijkerwijs van de realisatie van nieuwe toestanden op het grensvlak. Voor toepassingen die bestaan uit combinaties van verschillende complexe oxiden is een goed begrip van, en controle over grensvlakeigenschappen noodzakelijk. Dit proefschrift concentreert zich daarom op de grensvlakken van complexe oxiden. Aan de hand van vier gevallen worden hun eigenschappen bestudeerd.

Het eerste geval omvat de invloed die $SrTiO_3$-substraten (STO-substraten) uitoefenen op de hoge-T_c-supergeleider $La_{2-x}Sr_xCuO_4$ (LSCO), dat een sterk gecorreleerd elektronsysteem is. Het blijkt dat het substraat de LSCO-laag beïnvloed doordat het een epitaxiale vervorming van het kristalrooster veroorzaakt. Beneden de faseovergang van kubisch naar tetragonaal in het STO bij 105 K treedt een kleine tetragonale vervorming op die verrassend genoeg van invloed is op de elektronische eigenschappen van het LSCO. Het blijkt dat de geleidingsanisotropie voor $x = 0.10$–0.13 plotseling verandert wanneer deze faseovergang optreedt. De anisotrope bijdrage aan de geleiding is gericht langs de Cu-O-bindingen. De conclusie dringt zich op dat deze bijdrage wordt veroorzaakt door zogenaamde 'stripes'. Stripes zijn spontaan gevormde, langgerekte patronen van ladingen en spins. Bij Sr-fracties x, waarvoor aanwijzingen voor de aanwezigheid van stripes zijn gevonden, laat de magnetoweerstand een bijzonder gedrag zien. De magnetoweerstand bevat een component die lineair afhangt van het magnetisch veld, wat in de literatuur ook beschreven is voor LSCO-eenkristallen in een smal Sr-bereik rond $x = 0.125$. Het belangrijk verschil tussen de eenkristal- en de dunnelaagdata is het abrupt verdwijnen van de lineaire bijdrage beneden de 90 K voor de dunne lagen. Dit verschil moet worden veroorzaakt door de aanwezigheid van het STO-substraat, bijvoorbeeld door de epitaxiale vervorming die wordt opgelegd door het substraat. Het magnetoweerstands- als ook het anisotrope geleidingsgedrag suggereren sterk dat de lineaire magnetoweerstand een vingerafdruk is van fluctuerende

stripes, welke overgaan in statische stripes wanneer het substraat een faseovergang ondergaat en een structurele vervorming oplegt aan het LSCO. De studie van de LSCO-lagen leert verder dat lagen met een Sr-gradiënt kunnen worden gegroeid met gepulstelaserdepositie, door het substraat buiten het centrum van de plasmapluim te plaatsen. Bovendien is aangetoond dat een anisotrope component aanwezig is in de geleiding van de dunne laag, die wordt veroorzaakt door het trapvormig oppervlak van het STO-substraat. Dit betekent dat substraatstappen een dominante bron zijn voor vlakdefecten tijdens de groei van LSCO-lagen.

Het tweede geval betreft een tunnelstudie, waarbij elektronen door een potentiaalbarrière heengaan ('tunnelen'). Een verscheidenheid aan tunnelstructuren is gemaakt met het doel tunnelspectroscopie te bedrijven aan LSCO. De verschillende structuren laten geleidingsspectra zien zonder opvallende pieken, maar met een duidelijk lineaire afhankelijkheid van de aangelegde spanning. In sommige gevallen is het spectrum asymmetrisch en soms bevat het een 'gap'. De resultaten duiden op een onderdrukte ladingsdragerdichtheid bij het grensvlak tussen de supergeleider en de isolerende tunnelbarrière. Elektronen tunnelen dan in een lokaal niet supergeleidende, ondergedoteerde oppervlaktelaag. De data zijn geanalyseerd met een aantal verschillende modellen. De lineaire geleidingsachtergrond en de asymmetrie zijn te verklaren met het optreden van inelastische tunnelprocessen, hoewel de mogelijkheid dat de lineaire achtergrond wordt veroorzaakt door tunnelen via gelokaliseerde toestanden niet volledig kan worden uitgesloten. Sterke elektroncorrelaties kunnen de waargenomen asymmetrie niet verklaren, want de geleiding is het grootst wanneer elektronen het LSCO ingaan, wat in strijd is met theoretische voorspellingen.

De derde casus onderzoekt in twee verschillende benaderingen het grensvlak tussen $YBa_2Cu_3O_7$ (YBCO) en $La_{0.67}Sr_{0.33}MnO_3$ (LSMO). YBCO/LSMO-contacten en YBCO/LSMO/YBCO-juncties van het hellingstype zijn gefabriceerd om het elektronisch transport door dit grensvlak te onderzoeken. De contacten en juncties worden gekenmerkt door een hoge weerstand in de normale toestand van ongeveer 3 $\mu\Omega cm^2$. Ter vergelijking zijn er hellingstype contacten gemaakt waarvoor het LSMO vervangen is voor verscheidene andere materialen, waaronder het op hoge temperatuur gegroeide, ferromagnetische oxide $SrRuO_3$ (SRO). De weerstand van het YBCO/SRO grensvlak is ongeveer 0.1 $\mu\Omega cm^2$, en die van de YBCO/Au en YBCO/Pt grensvlakken zijn beide ongeveer 0.03 $\mu\Omega cm^2$. De grensvlakweerstand lijkt te schalen met de werkfunctieverschillen tussen YBCO en het materiaal van de bovenste elektrode. Tegelijkertijd mag ook verwacht worden dat reductie van het YBCO het sterkst optreedt voor YBCO in contact met LSMO, in vergelijking met SRO, Au en Pt, omdat de verandering van de Gibbs vrije energie het grootst is wanneer de elementen in LSMO reageren met zuurstof. De hoge weerstand van het YBCO/LSMO grensvlak zou daarom veroorzaakt kunnen worden door een zuurstoftekort in het YBCO. Dit scenario wordt echter niet ondersteund door de temperatuurafhankelijkheid van de grensvlakweerstand. Bovendien is het zuurstofgehalte in een junctiedoorsnede in kaart gebracht en kan geen zuurstoftekort worden waargenomen nabij het YBCO/LSMO grensvlak. In

plaats van aan zuurstoftekort is de hoge grensvlakweerstand toegeschreven aan ladingsoverdracht over het grensvlak, gedreven door het werkfunctieverschil tussen YBCO en LSMO. Van de wisselwerking tussen een antiferromagnetische neiging in YBCO en spingepolariseerd ferromagnetisme in LSMO wordt verwacht dat het een extra bijdrage levert aan de grensvlakweerstand. De antiferromagnetische neiging in YBCO zal versterkt worden door ladingsdepletie in het YBCO bij het grensvlak. Als gevolg daarvan zou een deel van de ladingsdragers die arriveren bij het grensvlak geblokkeerd kunnen worden. Experimenteel is een sterke magneetveldafhankelijkheid van de grensvlakweerstand gevonden, wat erop duidt dat een deel van de grensvlakweerstand van magnetische oorsprong is. Dit ondersteunt het blokkeerscenario. Geen van de YBCO juncties met LSMO barrières gedraagt zich als een ideale Josephsonjunctie.

In een tweede benadering zijn epitaxiale YBCO/LSMO en LSMO/YBCO-bilagen gegroeid in de geometrie van een supergeleidende spinschakelaar (met de supergeleider tussen twee ferromagnetisch lagen, i.e., LSMO/YBCO/LSMO). De literatuur voorspelt voor een dergelijke geometrie de mogelijkheid van aan- en uitschakelen van supergeleiding door middel van het manipuleren van de magnetisatietoestand (parallel of antiparallel) van de twee ferromagnetische lagen. Dergelijk gedrag is waargenomen in experimenten met structuren van ferromagneten en lage-T_c-supergeleiders. Data in de literatuur laten als functie van magnetisch veld schakeleffecten zien in de weerstand van oxidische heterostructuren bij temperaturen dichtbij T_c. Deze zijn tot nu toe geïnterpreteerd als gevolg van de supergeleidende spinschakelaar, of als het resultaat van de injectie van spingepolariseerde ladingsdragers in de supergeleider. De trilagen die voor dit proefschrift zijn gemaakt, zijn om deze effecten te versterken epitaxiaal gegroeid met de c-as geroteerd over 31° ten opzichte van de normaal van het oppervlak op STO-substraten met een (305)-oriëntatie. De LSMO-lagen die op deze manier gegroeid zijn blijken een eenassige magnetische anisotropie te bezitten. De magnetisatie kan op bijna ideale wijze als één domein worden geschakeld. Dit reduceert in sterke mate de strooivelden die worden veroorzaakt door magnetische domeinen. Het schakelen van de weerstand dat in dat geval wordt waargenomen is niet uniek gedefinieerd door de magnetisatietoestand (parallel of antiparallel) van de ferromagnetische lagen, maar hangt in plaats daarvan af van het extern aangelegde magnetisch veld en de magnetisatierichtingen van de individuele ferromagnetische lagen. Dit duidt erop dat de schakeleffecten in de weerstand worden veroorzaakt door het indringen van het magnetisch veld in de supergeleider, met het totale magnetisch veld bestaande uit het aangelegde veld en de magnetische strooiveldbijdragen van de ferromagnetische lagen. Ruwheid van het YBCO/LSMO-grensvlak speelt een belangrijke rol. Het is aangetoond dat ruwe grensvlakken grotere weerstandsschakeleffecten veroorzaken dan gladde grensvlakken, wat kan worden verklaard met de toegenomen strooivelden die de supergeleider indringen. Het strooiveldmodel wordt ondersteund door metingen aan bilagen. Aanzienlijke schakeleffecten in de weerstand zijn waargenomen voor YBCO/LSMO-bilagen gegroeid op STO-(305), die een tamelijk ruw YBCO/LSMO-grensvlak hebben.

Waar het grensvlak tussen de geleiders YBCO en LSMO een hoge weerstand heeft, is het grensvlak tussen de twee isolerende perovskieten $LaAlO_3$ (LAO) en STO geleidend. Dit is het onderwerp van de laatste casus in dit proefschrift. Verschillende experimenten beschreven in de literatuur laten zien dat de dikte van de geleidende laag slechts enkele nm bedraagt. De eigenschappen van deze geleidende grensvlakken zijn in dit proefschrift onderzocht bij lage temperatuur en hoge magneetvelden. De nadruk heeft gelegen op grensvlakken die zijn gemaakt door LAO te groeien op TiO_2-getermineerde STO-substraten bij relatief hoge ($\geq 1.0 \times 10^{-3}$ mbar) zuurstofdruk. Dergelijke grensvlakken hebben een grotere weerstand dan grensvlakken die zijn gegroeid bij lagere depositiedruk, en die supergeleiden beneden 200 mK. Verder neemt de weerstand van de hogedrukgrensvlakken toe voor afnemende temperatuur onder ongeveer 70 K, terwijl de weerstand van de grensvlakken die gegroeid zijn op lage druk monotoon afneemt met temperatuur. Op lage temperatuur (50 mK) laten de hogedrukgrensvlakken een grote (> 50 %) magnetoweerstand zien, die onafhankelijk is van de richting van het aangelegde magnetisch veld. Dit wijst op een spingerelateerde magnetoweerstand en niet op een baangerelateerde magnetoweerstand. In het proefschrift wordt beargumenteerd dat spinverstrooiing voortkomt uit de co-existentie van gelokaliseerde en beweeglijke elektronen, waarbij de gelokaliseerde elektronen optreden als magnetische momenten waaraan de beweeglijke elektronen verstrooid worden. Binnen dit scenario zou de weerstandstoename onder de 70 K een aanwijzing kunnen zijn van het Kondo-effect. Bij 50 mK zijn oscillaties waargenomen in de magnetoweerstand. De amplitude van deze oscillaties kan sterk worden vergroot door het verhogen van de snelheid waarmee het magnetisch veld toeneemt. De oscillaties hebben een ongewone $\sqrt{H}$-afhankelijkheid, waarbij H het magnetisch veld is. In een 10×30 μm^2 klaverbladstructuur zijn vergelijkbare oscillaties waargenomen. De oscillaties in deze structuur zijn onafhankelijk van de snelheid van magneetveldverandering. De periodiciteit van de oscillaties is onafhankelijk van de oriëntatie van het aangelegde magnetisch veld. De bijzondere periodiciteit en de onafhankelijkheid van veldoriëntatie sluiten verklaringen voor de oscillaties uit die gebaseerd zijn op Landau-kwantisatie. Verder onderzoek zal nodig zijn om de oorsprong van de oscillaties te bepalen.

Deze vier besproken gevallen laten alle zien dat de oxiden gevoelig zijn voor veranderende eigenschappen nabij grensvlakken. Epitaxiale vervorming, ladingsoverdracht, wisselwerking tussen verschillende typen magnetische ordening, magnetische strooivelden en structurele en elektronische eigenschappen zijn stuk voor stuk factoren die het gedrag van de oxidische materialen beïnvloeden op het grensvlak. Deze factoren stellen in staat tot de manipulatie van een grote verscheidenheid aan verschijnselen, van stripe-ordening in LSCO tot weerstandsschakeling in bijna supergeleidend YBCO en spinafhankelijk transport tussen niet-magnetische isolatoren.

De appendix bij dit proefschrift gaat in op de hypothese van het vormen van Cooperparen door de Coulombinteractie tussen gelijktijdig voorkomende elektronen en gaten in de cupraten. Hoewel het tweebandmodel veelvuldig is toegepast in

de literatuur om bepaalde transporteigenschappen van de cupraten te verklaren, is het moeilijk te verenigen met de temperatuurafhankelijkheid van de Hallhoek, zoals in de appendix wordt aangetoond. Niettemin wordt er een eenvoudig tweebandmodel voor supergeleiding uitgewerkt, dat laat zien dat de afstotende kracht tussen de ladingsdragers in een elektron- en een gatenband niet tot een Cooperinstabiliteit leidt.

Dankwoord

Dit proefschrift had ik niet kunnen schrijven zonder de hulp en ondersteuning van vele mensen. Het zijn ook deze mensen die ervoor gezorgd hebben dat de vier jaren die ik aan het promotieonderzoek gewerkt heb, zo plezierig zijn verlopen. Een woord van dank is dus op zijn plaats.

Ten eerste wil ik graag Hans bedanken als mijn promotor. Hans, je bent een ideeëngenerator pur sang met een groot netwerk van nationale en internationale contacten en een scherpe blik op zowel de inhoudelijke als de uiterlijke kant van het werk. Kortom, een prettige promotor! Tijdens een van de zeiluitjes van de groep heb ik je bij een wegvaarmanoeuvre achtergelaten op een drassige waterkant ergens in Friesland. Waar zouden we zijn geweest zonder jou als 'roerganger' van de groep? Bedankt voor de begeleiding en ondersteuning tijdens het hele project!

Alexander, ik had me geen betere begeleider kunnen wensen. Het enthousiasme dat je uitstraalt is erg motiverend geweest. Bedankt voor alle aanmoediging, inspiratie en inzichten tijdens vele discussies. De manier waarop je me begeleid hebt bij het schrijven van mijn proefschrift heb ik erg gewaardeerd. Zonder je ideeën en aansporingen hadden enkele hoofdstukken er heel anders uitgezien. Gezelligheid was er ook. Ik denk hierbij aan een kanotocht tussen alligators over de zwarte wateren bij New Orleans en een schaatstocht over het Zwarte Water bij Zwartsluis.

Mijn dank gaat ook uit naar Jan Aarts die een belangrijke rol heeft gespeeld in dit onderzoek door het introduceren van de magneten. De samenwerking die is ontstaan tijdens zijn sabbatical in Twente, heeft tot leuke resultaten geleid en tot twee hoofdstukken in dit proefschrift. Jan, ik heb me altijd verbaasd over je oog voor detail, het lijkt wel of niets je ontgaat.

Vruchtbaar was ook de samenwerking met het 'High Field Magnet Laboratory' in Nijmegen. In deze ben ik dank verschuldigd aan Jan Kees, Uli en Jos, die de experimenten mogelijk hebben gemaakt in dit bijzondere laboratorium. Nergens anders heb ik zo sterk het 'ontdekkingsreizigersgevoel' gehad om als eerste het gedrag te bestuderen van materialen onder de bijzondere omstandigheden die in het hoogveldlab gecreëerd kunnen worden. Met name Jos wil ik noemen vanwege de vele uren die hij met ons heeft doorgebracht tijdens lange meetsessies in het holst van de nacht en in de weekenden. Naast nuttig waren ze ook altijd erg gezellig!

Wilfred van der Wiel, Guus Rijnders en Dave Blank, bedankt voor jullie inbreng in het LAO/STO-onderzoek. Ook Gerwin, Jeroen Blok, Hans Boschker, Josée en Zhicheng Zhong hebben middels de 'interface meetings' in positieve zin aan hoofdstuk 6 bijgedragen.

Een bijzonder woord van dank aan iedereen die op welke wijze dan ook ondersteunend werk heeft verricht en zo een aandeel heeft aan de totstandkoming van dit proefschrift. Sybolt en Gerrit, op jullie kon ik altijd rekenen voor de röntgenkarakterisatie van dunne lagen. Van heel andere aard was de Vuelta-start 2009 die we vanaf de VIP-bank in de huiskamer van Sybolt hebben bekeken, een bijzondere belevenis! Alles draait om techniek. Frank en Dick, jullie dragen zorg voor het functioneren van een heel arsenaal aan apparatuur. Zonder jullie was dit promotieonderzoek onmogelijk geweest. Datzelfde geldt voor Harry en Jan, die in ruil voor een 'ofi-nummer' steeds weer een vaatje vloeibaar helium klaar hadden staan. Voor theoretische vragen was er altijd Sasha. Hij heeft de handvatten gegeven voor het uitwerken van het tweebandmodel, zoals het in de appendix beschreven staat. Dit hoofdstuk is dan ook voor een groot deel aan hem te danken. Rico Keim wil ik bedanken voor het uitvoeren van de electron energy loss experimenten die staan beschreven in hoofdstuk 4 en Aico voor de 'scanning SQUID'-metingen in ditzelfde hoofdstuk. Ans en Inke, dank voor de administratieve ondersteuning.

Jos Boschker, Menno, Peter Bosch, met veel plezier heb ik jullie begeleid met jullie afstudeeronderzoeken. Jullie werk heeft voor een belangrijk deel bijgedragen aan dit proefschrift, waarvoor dank. Menno, jouw resultaten hebben een mooie publicatie opgeleverd. Jullie hebben alle drie gekozen voor een promotieonderzoek na het afstuderen. Ik wens jullie hier alle succes bij!

Ik heb het naar mijn zin gehad in de vakgroep. Uit mijn jaren bij LT zijn waardevolle vriendschappen voortgekomen die wat mij betreft nog vele jaren zullen duren. Joska, ik hoop dat we nog vele gezellige avonden zullen doorbrengen en ik wens dat SolMates zal groeien tot een groot en succesvol bedrijf. Aan jouw passie zal het niet liggen! Kristiaan, schaatsen, fietsen, luidsprekers bouwen, wat hebben we allemaal niet gedaan? Laten we dat vooral blijven doen! Het is een eer dat je m'n paranimf bent. Kamergenoten Jeroen (100 pk) en Joost (125 pk), ik ben blij dat ik jullie ervan heb kunnen overtuigen dat motorrijden een schitterende hobby is. Ik hoop op nog vele gezamenlijke kilometers en die reis naar Scandinavië gaan we zeker een keer maken. Mark, Aico, Alexander, Kees, Aleksandar, Johannes, Menno, Martin, Reinder, Ariando, Karthi, Pieter, Hendrie, Robert-Jan, Sander, Bernard, kamergenote Michelle (1 pk) en alle andere promovendi, postdocs en afstudeerstudenten die LT rijk is en is geweest, bedankt voor jullie bijdrage aan een leuke tijd!

Het zaalvoetbal heeft zeker bijgedragen aan mijn mentale en fysieke gezondheid tijdens de promotie. Matthijn, Peter, Hans Boschker, Ruud, Menno, Joska, Mark Huijben, Mark Smithers, ik heb genoten van deze leuke potten. Ik hoop dat mijn gebrek aan talent het team geen onherstelbare schade heeft toegebracht.

Bedankt ook de WOE2008 groep: Gertjan, Hajo, Wolter, Mark, Jeroen, Josée en Guus. Deze conferentie aan de voet van de Rocky Mountains en het aanslui-

tend verblijf op een door burlende wapiti omgeven camping vormde een van de hoogtepunten van de afgelopen vier jaar.

Kristiaan, Joost, Jeroen, Menno, Kees en Sybolt, bedankt voor het nalezen van hoofdstukken van dit proefschrift. Jeroen, je hulp en inbreng (ondanks je volle agenda) bij het ontwerpen van de omslag heb ik bijzonder gewaardeerd.

Naast mijn collega's wil ik alle vrienden bedanken. Een bijzondere plaats daarin nemen mijn oud-huisgenoten De Kadullen. Kadul ben je voor het leven!

Dat het bedanken van familie geen cliché is, heb ik de afgelopen jaren mogen uitvinden. Pa, ma, Annemiek, Maaike, jullie steun en liefde waren onvoorwaardelijk! Ook mijn schoonfamilie wil ik hierbij niet onvermeld laten. Jullie warmte heeft mij altijd goed gedaan!

Vier jaar heb ik mogen werken aan onderzoek. Er zijn resultaten geboekt en nieuwe dingen geleerd. Toch deed ik de belangrijkste ontdekking drie jaar voor ik aan mijn promotie begon. Marjon, mijn lieve vrouw, jij bent de kern van mijn bestaan. Bedankt voor alle ondersteuning die je hebt gegeven en het begrip en geduld waarmee je naar mijn verhalen hebt geluisterd. Ik ben gelukkig dat we het afgelopen jaar onze liefde hebben mogen bestendigen. Op onze trouwkaart stonden woorden van de schrijfster George Sand: 'There is only one happiness in life, to love and be loved.' Ik zou daar nu een citaat aan willen toevoegen, afkomstig van haar geliefde, de componist Frédéric Chopin:

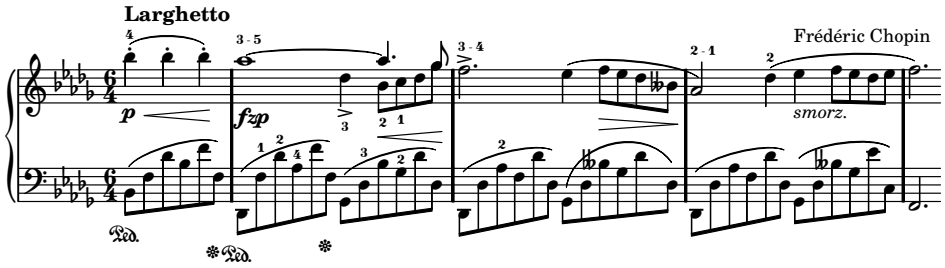

Ik hoop dit een leven lang voor je te mogen spelen.

Enschede, oktober 2009

Stellingen

behorende bij het proefschrift

In Between Matters, Interfaces in Complex Oxides

Maarten van Zalk

1. Een uiterst kleine roostervervorming in een dunne laag $La_{2-x}Sr_xCuO_4$ ($0.10 < x < 0.13$), opgelegd door een structurele faseovergang in het substraat, leidt tot het vastpinnen van fluctuerende 'stripes'. *(hoofdstuk 2)*

2. Het is niet realistisch te verwachten dat een perfect $YBa_2Cu_3O_{7-\delta}$/ $La_{0.67}Sr_{0.33}MnO_3$-grensvlak een transparantie heeft die te vergelijken valt met die van een metaal/metaal-grensvlak. *(hoofdstuk 4)*

3. Weerstandsveranderingen geïnduceerd door het schakelen van de magnetisatietoestand in oxidische F/S/F-trilagen van ferromagneten (F) en supergeleiders (S) worden gedomineerd door magnetische strooivelden. *(hoofdstuk 5)*

4. De grote magnetoweerstand bij lage temperatuur van $LaAlO_3/SrTiO_3$-grensvlakken die bij relatief hoge zuurstofdruk gegroeid zijn, wordt veroorzaakt door lokale magnetische momenten aan het grensvlak. *(hoofdstuk 6)*

5. Een groot potentieel voor de landbouw ligt op zee.

6. De gewoonte om proefschrifthoofdstukken in Nederland standaard op een rechterpagina te beginnen kost jaarlijks circa 100 bomen.

7. Het gebruik van 'doping' om bijzondere resultaten te behalen komt ook in de wetenschap veel voor.

8. Een goed begin van de oplossing van het fileprobleem is de halvering van het aantal wielen per voertuig.

PROPOSITIONS

accompanying the thesis

In Between Matters, Interfaces in Complex Oxides

Maarten van Zalk

1. An extremely small lattice modification in $La_{2-x}Sr_xCuO_4$ thin films ($0.10 < x < 0.13$), enforced by a structural phase transition of the substrate, causes the pinning of fluctuating stripes. *(chapter 2)*

2. It is unrealistic to expect the $YBa_2Cu_3O_{7-\delta}/La_{0.67}Sr_{0.33}MnO_3$ interface to have a transparency that is comparable to that of a metal/ metal interface. *(chapter 4)*

3. Resistance changes induced by magnetization switching in oxide F/S/F trilayers of ferromagnets (F) and superconductors (S) are dominated by magnetic stray fields. *(chapter 5)*

4. The large magnetoresistance at low temperature of $LaAlO_3/SrTiO_3$ interfaces grown at relatively high oxygen pressure, are caused by local magnetic moments at the interface. *(chapter 6)*

5. A big potential for agricultrure is at sea.

6. The custom to begin thesis chapters in the Netherlands standardly on the right page yearly costs 100 trees.

7. The use of doping to obtain extraordinary results also frequently occurs in science.

8. A good start to solve the problem of traffic jams is to halve the number of wheels per vehicle.